

## Notes on the calibration of the JHU-APL Solar Vector Magnetograph at NSO-Sac Peak

Gianna Cauzzi<sup>1,2</sup>

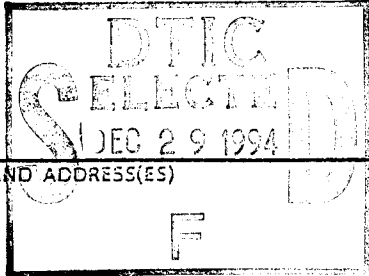
NSO Technical Report 1991-02

# National Solar Observatory

19941227 066

[illegible]

The National Solar Observatory is a Division of the National Optical Astronomy Observatories, which is operated by the Association of Universities for Research in Astronomy, Inc., under contract to the National Science Foundation.

REPORT DOCUMENTATION PAGE			Form Approved OMB No. 0704-0188	
Public reporting burden for this collection of information is estimated to average 1 hour per response, including the time for reviewing instructions, searching existing data sources, gathering and maintaining the data needed, and completing and reviewing the collection of information. Send comments regarding this burden estimate or any other aspect of this collection of information, including suggestions for reducing this burden, to Washington Headquarters Services, Directorate for Information Operations and Reports, 1215 Jefferson Davis Highway, Suite 1204, Arlington, VA 22202-4302, and to the Office of Management and Budget, Paperwork Reduction Project (0704-0188), Washington, DC 20503.				
1. AGENCY USE ONLY (Leave blank)	2. REPORT DATE 21 December 1994	3. REPORT TYPE AND DATES COVERED Reprint		
4. TITLE AND SUBTITLE Notes on the Calibration of the JHU-APL Solar Vector Magnetograph at NSO-Sac Peak		5. FUNDING NUMBERS PE 61102F PR 2311 TA G3 WU 22		
6. AUTHOR(S) Gianna Cauzzi				
7. PERFORMING ORGANIZATION NAME(S) AND ADDRESS(ES) Phillips Laboratory/GPSS 29 Randolph Road Hanscom AFB, MA 01731-3010		8. PERFORMING ORGANIZATION REPORT NUMBER  PL-TR-94-2308		
9. SPONSORING/MONITORING AGENCY NAME(S) AND ADDRESS(ES)  		10. SPONSORING/MONITORING AGENCY REPORT NUMBER		
11. SUPPLEMENTARY NOTES Reprinted from National Solar Observatory Technical Report 1991-02				
12a. DISTRIBUTION/AVAILABILITY STATEMENT  Approved for public release; distribution unlimited		12b. DISTRIBUTION CODE		
13. ABSTRACT (Maximum 200 words) We discuss two different techniques for the conversion of polarization signal in magnetic fields, the calibration curves and derivative methods, for the case of an imaging magnetograph. The advantages and typical errors of both techniques are analyzed in respect to the instrumental characteristics, particularly the spectral response. Both methods present high degree of errors, but the calibration curves method is probably more suitable for the present instrumental configuration of the SVMG.				
14. SUBJECT TERMS Solar magnetic field                      Solar instrumentation Solar magnetographs Vector magnetograph			15. NUMBER OF PAGES 52	
			16. PRICE CODE	
17. SECURITY CLASSIFICATION OF REPORT Unclassified	18. SECURITY CLASSIFICATION OF THIS PAGE Unclassified	19. SECURITY CLASSIFICATION OF ABSTRACT Unclassified	20. LIMITATION OF ABSTRACT SAR	

**Notes on the calibration of the JHU-APL Solar  
Vector Magnetograph at NSO-Sac Peak**

**Gianna Cauzzi<sup>1,2</sup>**

*NSO Technical Report 1991-02*

<sup>1</sup> USAF-Phillips Lab., Geophysics Directorate, National Solar  
Observatory/Sac. Peak, NOAO\*\*, Sunspot NM, U.S.A.

<sup>2</sup> NAS/NRC Research Associate, on leave from Dip. di As-  
tronomia, Università di Firenze.

\*\* Operated by the Association of Universities for Research in  
Astronomy Inc.

# Notes on the calibration of the JHU-APL Solar Vector Magnetograph (SVMG) at NSO-Sac Peak

Gianna Cauzzi<sup>1,\*</sup>

<sup>1</sup> USAF-Phillips Lab., Geophysics Directorate, National Solar Observatory/Sac. Peak, NOAO<sup>\*\*</sup>, Sunspot NM, U.S.A.

\* NAS/NRC Research Associate, on leave from Dip. di Astronomia, Università di Firenze.

<sup>\*\*</sup> Operated by the Association of Universities for Research in Astronomy Inc.

**Abstract.** We discuss two different techniques for the conversion of polarization signal in magnetic fields, the *calibration curves* and *derivative* methods, for the case of an imaging magnetograph. The advantages and typical errors of both technique are analysed in respect to the instrumental characteristics, particularly the spectral response. Both methods present high degree of errors, but the *calibration curves* method is probably more suitable for the present instrumental configuration of the SVMG.

## INTRODUCTION

Vector magnetic fields are a *leitmotiv* in modern solar physics, especially for their role in explosive phenomena like flares. Recently, many solar observatories, and NSO-Sac Peak within them, tried to establish good sensitivity vector magnetograph systems, at high spatial and temporal resolution (Zirin, 1985; Ai, 1987; Hagyard, 1988; Rust and O'Byrne, 1991). However, two issues are still the nightmare of every physicist that wants to deal with vector magnetic fields, especially if he (she) is working with an imaging instrument:

- 1- the need to get observations of extremely high quality and,
- 2- the need of a *reliable* (and possibly fast) way to convert the observed polarization into magnetic fields.

In these notes we will concentrate only on the conversion of polarization signal to magnetic field, what we will call "calibration procedures", for the Solar Vector Magnetograph (SVMG) at NSO-Sac Peak, i.e., considering its particular instrumental set-up and the spectral line the instrument works at. Nevertheless, we hope that some of the considerations and analyses here made will result useful for other similar devices.

We will assume that other factors (instrumental polarization, different transmission due to the state of polarization of the light, non-uniformity of transmission and spectral tuning on the FOV, etc.) have already been taken into account, and will concentrate on two different calibration techniques, first for "theoretical" conditions, then considering the effect of spectral smearing and other error sources.

## 1. THE INSTRUMENT AND THE CALIBRATION METHODS

The JHU-APL Solar Vector Magnetograph (SVMG) is an imaging magnetograph, i.e. it acquires narrow band images in different light polarisation states (selected through different settings of a quarter waveplate and a Glan-Taylor prism). The images correspond to measurements of  $I+Q$ ,  $I-Q$ ,  $I+U$ ,  $I-U$ ,  $I+V$ ,  $I-V$ , where  $I$ ,  $Q$ ,  $U$ ,  $V$  are the usual Stokes parameters, and are acquired at a rate of  $\sim 30$  images/min. In a normal observing procedure, up to 20 images are accumulated for each polarisation state, in order to increase the signal-to-noise ratio; this brings the acquisition time for a sequence to  $\sim 5$  minutes. The field of view (FOV) is  $\sim 4 \times 3$  arcmin<sup>2</sup>, the pixel size is 0.4 arcsec.

The SVMG operates in the magnetic CaI 6122.22 Å line, that has a Doppler width of  $\sim 120$  mÅ and a Landé factor  $g_L$  of 1.75.

The spectral selection in the SVMG is performed by a tunable, lithium-niobate, Fabry-Perot Interferometer (FPI) and by an interference blocker, that acts as a prefilter for the FPI.

The FPI has a transmission profile described by the usual Airy function (Hernandez, 1986), with a FWHM of  $\sim 150$  mÅ and a FSR of 3.25 Å (Fig. 1a). The transmission is nominally around 50%, but no precise measurements have been recently made.

Duncan and Thomas, 1987, provide some information about the spectral position of the FPI orders in the range 6000-7000 Å.

The blocker has a FWHM of  $\sim 1$  Å and a FSR of 16 Å (Fig. 1b). The only ways to tune the blocker are:

- 1- tilt it, with the effects of shifting the passband towards the blue ( $\sim 20$  mÅ/deg), or
- 2- changing the temperature, moving the passbands of approximately 80 mÅ/°C (cooling - blue shift; heating - red shift).

The second option is not feasible during an observing sequence, and the first hasn't been investigated carefully up to now, so that actually during the observations the blocker sits at one fixed wavelength. The central position of the blocker passband is, as we will see later, important for the validity of the calibration procedure, and it must be carefully chosen.

The nature of the SVMG, an imaging filter magnetograph, doesn't allow the use of calibration methods based on a full profile analysis of the Stokes profiles  $I$ ,  $Q$ ,  $U$ ,  $V$  (see Skumanich and Lites, 1987), at least on a regular basis, for two main reasons:

- 1- the acquisition of images along the line profile with a good spectral sampling rate ( $\sim 1/2$  FWHM, 50-70 mÅ) will take too much time (more than 1 hr.), with all the problems related to changes of the structures<sup>1</sup>.
- 2- the computing time necessary to perform this analysis for all the  $2 \times 10^5$  (or more) points in the FOV would be a prohibitive restriction.

The daily calibration must be, therefore, based on the signal at 1 or few wavelengths in particular positions in the line.

Two possible methods are:

- 1- conversion of polarization signal to magnetic field through calibration curves, built solving the equations of transfer for polarised radiation for the spectral line in a particular atmospheric model, and finally considering the spectral transmission profile of the instrument (in our case FPI + blocker). This is the method adopted, for example, by the Marshall group (Hagyard *et al.*, 1988), and, for the limited case of longitudinal field, by many others (Title *et al.*, 1987; Lundstedt *et al.*, 1991).
- 2- in weak field approximation (WFA), use of the derivative method, that states the proportionality of the polarization signals, both linear and circular, to magnetic field, through the slope of the line

<sup>1</sup> An alternative "solution" could be the acquisition of images along the whole line profile with a smaller number of accumulations (even single images), that will reduce the total time to  $\sim 10$  min. According to Lites and Skumanich (1984), this will still give a precision of 5% (for fields bigger than 1000 G) and it's something worth further investigations.

profile (Jefferies *et al.*, 1989; Jefferies and Mickey, 1991, hereafter JM).

Unfortunately, at this time the SVMG is still in the "test" phase so that few observations are now available. In particular, no observations along the whole line profile have been performed, and a check of the validity of the 2 mentioned calibration methods vs. fitting line profiles methods is not possible yet.

## 2. SYNTHETIC LINE PROFILES

The profiles have been computed using Graham Murphy's code, Stokes Profiles Synthesis Routine (SPSR, Rees *et al.*, 1989), for the CaI 6122 line and three different atmospheric models: quiet sun VAL3C (Vernassa *et al.*, 1981), Moe-Maltby penumbral (1969) and Maltby umbral (Avrett *et al.*, 1986). The magnetic parameters have been assumed constant with height in all the calculations; we used a grid of values of  $B$  (total magnetic field) and  $\gamma$  (inclination of magnetic field with respect to the line of sight) ranging from 0 to 2500 G (step 50 G), and from 0 to 90° (step 30°) respectively. The azimuth of the field,  $\chi$ , is normally computed through the ratio of the parameters  $Q$  and  $U$  independently from the adopted calibration technique, and therefore we limited ourselves to the case of  $\chi = 0^\circ$ . Nevertheless, we'll make a brief comment about the determination of this parameter and errors involved, in Sect. 5.

The wavelengths step for the simulated profiles is 10 mÅ.

Fig. 2a shows the I profile for the VAL3C model, and no magnetic fields; Figs. 2b-d show Stokes I and V (on the same scale) for 3 different sets of  $B$ ,  $\gamma$  and  $\chi$ . Figs. 3b-d show the same, for the U and Q parameters. All the profiles are normalized to the continuum intensity.

It might be useful to remind that for  $\gamma = 0^\circ$  the transverse field is absent, while when  $\gamma = 90^\circ$  the longitudinal field is zero.

Figs. 4-5 and 6-7 are the same as 2 and 3, but for the Moe-Maltby penumbral and Maltby umbral models, respectively. The line is enormously strengthened in the penumbral and umbral models, respect to the quiet sun, and this can be a font of errors in the calibration, especially using the calibration curve method. The validity of umbral models is somehow in discussion, but now we don't have any observation of the line profile in a spot, that can confirm or discharge these simulations.

## 3. CALIBRATION CURVES. POLARIZATION VS. MAGNETIC FIELD.

### 3.a The "theory"

The *calibration curves* method essentially consists in determining functional relationships between the magnetic field and the correspondent fractional polarisation (both circular and linear). These relationships are derived solving the equations of transfer for polarised radiation, for the particular case of constance of magnetic parameters with height in the atmosphere, as mentioned in Sect. 2. We can write:

$$B_L = f_1(\gamma, \lambda, B, \dots) P_V \quad (1)$$

$$B_T = f_2(\gamma, \lambda, B, \dots) P_Q^{1/2} \quad (2)$$

where  $P_V = V/I$ , is the fractional circular polarization,  $P_Q = \sqrt{Q^2 + U^2}/I$  is the fractional linear polarisation, and  $B_L$  and  $B_T$  the longitudinal and transverse magnetic fields.

$f_1$  and  $f_2$  are, in general, functions of the atmospheric model, the magnetic parameters (for example, there is a strong dependence on the inclination  $\gamma$ ), the transmission profile of the filter and the wavelength position in the spectral line. Examples of such curves are shown in Figs. 8 and 9, for the Moe-Maltby penumbral model, and  $B_L$  and  $B_T$  respectively. The fractional polarisation is shown for several spectral positions in the blue wing of the line (from -260 mÅ to -120 mÅ from line center); the spectral smearing due to the FPI and blocker hasn't been taken into account.

Fig. 10 is the same as Fig. 9, but on a logarithmic scale, to better show the (quite small) values of linear polarisation.

In weak field approximation (WFA) Eqs. (1) and (2) become simpler (Hagyard *et al.*, 1988):

$$B_L = c_1 P_V \quad (3)$$

$$B_T = c_2 P_Q^{1/2} \quad (4)$$

where  $c_1$  and  $c_2$  are now constant with the magnetic parameters, even though still dependent on the wavelength and the filter characteristics (and the model, as before). The WFA nominally holds for values of  $\nu_B = \Delta\lambda_B/\Delta\lambda_D \ll 1$ , where  $\Delta\lambda_B$  is the splitting Zeeman, or

$$\Delta\lambda_B = \mu\lambda^2 g_L B = 4.67 \times 10^{-13} \lambda^2 g_L B \quad (5)$$

with  $\lambda$  measured in Å and B in Gauss<sup>2</sup>. For the Ca 6122 line, this translates in  $B \leq 2000$  G, assuming a value of 120 mÅ for  $\Delta\lambda_D$ . However, a quick look at Figs. 8 and 10 will tell us that this is not strictly true, i.e. the linearity between  $B_L$  and the circular polarisation holds up to  $\sim 1000$ -1500 G, but, even in this range, the differences due to the inclination are relevant. The same considerations apply to the  $B_T$ , where the deviations from the linearity are more severe.

Usually the curves of polarization vs. magnetic field are shown for just one value of inclination ( $\gamma = 0^\circ$  for the longitudinal field, and  $\gamma = 90^\circ$  for the transverse), and no mention is made about the eventual differences, but this is a source of significant error, as we will see in Sect. 3.d.

Some preliminary tests showed that the same problems are present in the magnetic line FeI 5250 also, so we can probably generalize the question of the validity of relations (3) and (4).

The choice of the working wavelength is dictated by the need of a good signal-to-noise ratio, and by the need of avoiding, as much as possible, saturation effects, magneto-optical effects, dependence on inclination values etc; its value must be carefully considered in order to satisfy these conditions. In Figs. 8 and 9 is clear that the signal is increasing noticeably going towards line center, but at the same time some of the problems just mentioned appear: the difference in the curves due to the  $\gamma$  values, for example, is increasing with wavelength, especially for the longitudinal field; the magneto-optical effects are present at  $\lambda=6122.08$  and  $6122.1$  Å, etc.

Due to the particular combination of a big  $\Delta\lambda_D$  and a quite low  $g_L$  factor, the CaI 6122 line doesn't suffer of saturation problems, unless we go too close to the line center or at very high magnetic fields ( $\geq 3000$  G). The same two factors, however, contribute to rather small values of polarization: in Fig. 8 we can see that, at  $\lambda=6122.02$  Å, for example, we have a V/I ratio of  $\sim 3\%$  for 500 Gauss; for the magnetic FeI 5250 line ( $g_L=3$  and  $\Delta\lambda_D \sim 40$  mÅ), at a similar distance from the line center, the fractional circular polarization would be close to 15% for the same 500 G. The values of linear polarisation are better visualised in Fig. 10, and are not very encouraging: at  $\lambda=6122.02$  Å, a sensitivity of  $10^3$  will be sufficient to detect transverse fields of no less than 3-400 G.

The FPI and the blocker, though, change the Stokes parameters profiles: we must hence analyse their effects, and choose our working wavelength(s) on the base of the results.

We will analyse the effects of the FPI alone, first, and then add the blocker. This could be useful in a near future, when a tunable blocker will be allowable, and the net spectral transmission profile will be the one of the FPI only.

### 3.b Effects of spectral smearing. FPI

To simulate the effects of the spectral smearing introduced by the Fabry-Perot, we convolved the Stokes parameters correspondent to the different models and values of magnetic fields, described in Sect. 2, with the transmission profile shown in Fig. 1a. It might be useful to remind that we must convolve the parameters *first*, and then do the ratio to obtain the fractional polarizations of

<sup>2</sup>Following Jefferies *et al.*, 1989, 0.5 is a reasonable upper limit for  $\nu_B$ .

Figs. 8-10: this is because the ratio and the convolution do not commute.

Fig. 11 shows the Stokes profiles for the case of  $B=1500$  G,  $\gamma = 30^\circ$  and  $\chi = 60^\circ$ , in photospheric model, "original" and convolved with an Airy function of  $150$  mÅ of FWHM (and normalising the continuum intensity to 1, as before). The profiles are shallower as expected, but, happily, the convolved V, U, Q signals are greater than the original ones for wavelengths  $\leq 6122.06$  Å (this "cutting" wavelength depends on the model and the filter characteristics); in the case of U and Q, the smearing profile is big enough to dilute all the details in the line center<sup>3</sup>.

Figs. 12-14 are the analogous of Figs. 8-10, this time considering the convolution with the FPI profile. The polarization signal is in this case bigger for wavelengths  $\leq 6122.04$  Å. We can notice from Fig. 12 that the range of linearity for  $B_L$  is greatly extended (up to the limit of our simulations, i.e. 2500 G), and the differences due to the  $\gamma$  values are reduced, even if not completely. For the transverse field, the same extension of the linear regime applies, but the differences introduced by various  $\gamma$  values are enhanced: the reason for this apparently strange behavior sits in the rapidly varying shape of the U and Q profiles, and in their dependence on the inclination.

We can probably clarify the issue with an example: Fig. 15a shows two Q profiles for  $B_T=1000$  G,  $\gamma = 30^\circ$  and  $90^\circ$ , and  $\chi = 0^\circ$ . The two profiles are extremely different but in the line center and the far wings, where we ought work. However, when we convolve with the FPI profile, whose FWHM is bigger or comparable to the wavelength scale of variation of the Q parameters, the two signal do not coincide anymore, even in the far wings, as shown in Fig. 15b<sup>4</sup>. Since we don't have any other independent way to determine  $\gamma$ , we must choose one or another of these curves (or a combination of them) as our calibration curve: this will lead us in any case to errors in the determination of magnetic fields.

The spectral smearing hence, as we will see in Sect. 4 also, has double-faced effects: on the good side, it enhances the signal level in the wings and increases the linearity of the curves, therefore reducing errors due to the velocity, e.g.; on the bad side, it brings signal from the line center, with all the related problems, to the line wings, therefore introducing dishomogeneities like the  $\gamma$  dependence.

### 3.c Effects of spectral smearing. Blocker

In the actual version of the SVMG the blocker is not easily tunable, so we have to determine which is the most convenient wavelength to sit the blocker on. Fig. 16 shows the same case of Fig. 11, for two different positions of the blocker, in line center and in the blue wing (note the different scale on the y axis respect to Fig. 11). For the intensity profile the differences are 15-30% when the blocker is position at line center (in the range of wavelengths 6121.96-6122.10), and 5-10% when in the wing; the differences in V, Q, U are not as big (5-10% of the original polarisation signal when the blocker is positioned at line center, and 2-5% when in the wing). However, the quantities  $P_V$  or  $P_Q$  will be different from the case of FPI only, so the calibration curves must be built taking into account the blocker.

If we work at one single wavelength, or few of them very close together, the best position for the blocker is that same working wavelength; if we want to perform a scan of the whole line profile, it will be easier to keep the blocker at line center, in order to maintain things symmetric.

Figs. 17-19 are the same as Figs. 12-14, but taking into account the influence of the blocker, set at the same nominal wavelengths; apart for slight differences in the fractional polarization signals, the curves have the same shapes.

<sup>3</sup>In all the simulations, the contrast of the intensity profile (defined as  $(I_{cont.} - I_{l.c.})/I_{cont.}$ ) is around 35%, while the observed one doesn't go over a mere 15%. This suggests the presence of a strong percentage of scattered light, that will affect all the calibration procedures. It's therefore crucial try to reduce this scattered light at the minimum possible level by means, e.g., of several field stops in the optical path.)

<sup>4</sup>This problem is common to all the imaging magnetographs, where the spectral selection is performed by means of filters with passbands around 100 mÅ.

### 3.d Calibration curves and errors

From Figs. 17 and 19, we can see that the more useful wavelengths are in the range 6122.00-6122.06 Å; in fact, at lower wavelengths the signal is extremely small, especially for the linear polarisation (a  $P_Q$  value of  $5 \times 10^{-4}$  corresponds to  $B_T \sim 350$  G.), while closer to the line center the inclination, magneto-optical and saturation effects are stronger.

Estimating the sensitivity of the instrument at  $\sim 2 - 3 \times 10^3$ , at these wavelengths we should be able to detect transverse fields of 1-200 G, and longitudinal fields of  $\sim 10$  G.

Tables 1 and 2 show the values of the calibration constants  $c_1$  and  $c_2$  of Eqs. (3) and (4) obtained from our simulations. Some more or less obvious consideration can be made: at each fixed wavelength, the polarisation signal is smaller in photosphere, and stronger in the umbra, and the models are very different each other; the signal increases with the inclination, both for longitudinal and transverse field; there is quite a big difference between wavelengths distant as low as 20 mÅ.

The weak field approximation is very good for the case of  $B_L$ , where the deviations from linearity are of 2-3% max; the same is not completely true for  $B_T$ , where these deviations can reach 10-12%. If we assume a power law relationship between  $B_T$  and  $P_Q$ :

$$B_T = c_3 P_Q^{c_4} \quad (6)$$

the best exponent for  $P_Q$  would be 0.55-0.58, instead of 0.5.

Besides the validity of the WFA, errors typical of this calibration method are related to velocity effects, line-of-sight inclination dependence, model dependence. Trying to quantify these errors, we will assume as *mean* calibration curves for our magnetograms the ones corresponding to the penumbral model, at  $\lambda=6122.04$  Å and  $\gamma = 30^\circ$  (for  $B_L$ ;  $\gamma = 60^\circ$  for  $B_T$ ).

**3.d.1 Line-of-sight inclination dependence.** Our calibration curve corresponds to a particular value of  $\gamma$ , but nobody can tell us *a priori* what the real inclination of the field is. An estimate of the error related to this assumption is given in Figs. 20a and 21a, for  $B_L$  and  $B_T$  respectively. The curves are computed using the polarisation signals corresponding to different  $\gamma$  values, for the same wavelength and model and converted into magnetic fields using the *mean* curve described above. The errors for  $B_L$  are  $\leq 10\%$ , mainly for the case of  $\gamma = 60^\circ$ . The situation is not so good for the  $B_T$  case, where the errors for the case of complete transverse field ( $\gamma = 90^\circ$ ) are constantly over 20% and can go up to 40%<sup>5</sup>. Probably a calibration curve computed for  $\gamma = 45 - 50^\circ$  would reduce some of these errors.

**3.d.2 Velocity effects.** A velocity field will shift the spectral line of a quantity  $\Delta\lambda = v\lambda/c$  and therefore reduce the validity of the mean calibration curve, since we will be at a different wavelength from the working one. Figs. 20b and 21b show the effects of a velocity field of  $\pm 1$  Km/sec. (a typical value for solar features) that translates into a shift of  $\pm 20$  mÅ. As in the previous example, the curves are computed using the polarisation corresponding to the adjacent wavelengths, and converted into magnetic fields through the *mean* curve.

The errors are similar in both the  $B_L$  and  $B_T$  cases, and of the order of 15%.

**3.d.3 Model dependence.** Usually, many different features are present in the FOV, therefore the assumption of a single model (in this case penumbral) introduces errors. To estimate it, we took the polarisation signal corresponding to  $\lambda=6122.04$  Å and  $\gamma = 30^\circ$  ( $60^\circ$ ) for the three models, and converted it through the mean curves. The results are shown in Fig. 22a and b: for the longitudinal field a penumbral model used in a photospheric situation introduces an underestimate of the field up to 30%; for the umbral case we have an overestimate of  $\sim 15-20\%$ . In the transverse field we have a similar overestimate, of  $\sim 15-20\%$  in both the situations.

Sometimes, some of the errors just described will compensate each other, like the case of umbral field with a downward motion, but of course we cannot count on this kind of "tricks", especially

<sup>5</sup>Note that below  $\sim 200$  G the determination of the field is very uncertain.

because we don't know anything about the velocity or other thermodynamical parameters of the solar features. Trying to be pessimistic, we built the so-called "everything wrong" curve, where we take the linear polarisation for the umbral model, at  $\lambda=6122.02 \text{ \AA}$  and  $\gamma = 90^\circ$ , and calibrate it with the mean curve: the result is in Fig. 23, and the errors can be as big as 50%.

#### 4. DERIVATIVE METHOD IN WEAK FIELD APPROXIMATION.

##### 4.a The "theory".

In a recent paper, Jefferies and Mickey (1991) extended the range of applicability of the weak field approximation, as defined in Sect. 3.a, provided that the derivatives of the Voigt function describing the line profile fall off fast enough. At the very end, this translates into the possibility of using the WFA for values of  $\nu_B$  as big as 1.5, maintaining a precision of 15-20%, if we work at about  $\sim 3 \Delta\lambda_D$  from the line center; this result is rather independent from the adopted atmospheric model.

The equations that describe this "new" WFA are (JM):

$$B \cos \gamma = \frac{k_1}{g_L} \frac{V}{dI/d\lambda} \quad (7)$$

$$B \sin \gamma = \frac{k_2}{g_L} \sqrt{\frac{\Delta\lambda(Q^2 + U^2)^{1/2}}{dI/d\lambda}} \quad (8)$$

where  $dI/d\lambda$  is the slope of the intensity profile,  $\Delta\lambda$  is the offset from line center,  $k_1 = 5.4 \times 10^4 \times (6300/\lambda)^2$ ,  $k_2 = 6.2 \times 10^4 \times (6300/\lambda)^2$ , with wavelengths measured in  $\text{\AA}$  and  $B$  in Gauss. Eqs. (7) and (8) are valid for all the lines, and, at least in principle, the method shouldn't be affected by model dependence or velocity effects (as far as the shift is small enough to keep us in the range of validity of the WFA). This seems therefore a very attractive method for the calibration of imaging magnetographs: the only requirement is the acquisition of 2 or more images close in wavelength, so to estimate the value of  $dI/d\lambda$ .

An obvious first obstacle is that at 3 (or more)  $\Delta\lambda_D$  from the line center, the polarisation signal is extremely small, and hence very difficult to detect: in Fig. 19, e.g., we see that at  $-2\Delta\lambda_D$  ( $\lambda=6121.96 \text{ \AA}$ ) the linear polarisation reaches detectable values only for  $B \geq 500 \text{ G}$ ; at  $3\Delta\lambda_D$  this lower limit increases to  $\sim 800 \text{ G}$ .

We can check if a sort of "compromise" between the distance from line center and value of fractional polarization will work, may be at the prices of a bigger uncertainty on the field values.

Fig. 24 shows the curves obtained with Eq. (7) for the same model, field values, inclinations and wavelengths of Fig. 8. The slope of the intensity profile has been evaluated with the "analytical" derivative of the Stokes I; the spectral smearing due to FPI+blocker hasn't been taken into account.

Fig. 25 shows the correspondent percentage errors, defined as  $(B_{\text{inp}} - B_{\text{out}}) \times 100/B_{\text{inp}}$ . The agreement between the input and the computed fields is much better further in the wing (as expected) and for smaller fields, and differences due to the inclination values still exist. In the range of wavelengths previously defined on the base of the polarisation signals, the errors that we get using eq. (7) are within 10% up to a 1000 G, but get much worse for bigger fields.

Figs. 26-27 are the same, for the transverse field case, i.e., using eq. (8). The general trend is the same as before, but the amplitude of the errors is bigger. For the case of pure transverse field ( $\gamma = 90^\circ$ ) the errors are quite small everywhere, but this is unfortunately not true in the other 2 cases, even though we remain in the range of  $\sim 20\%$  foreseen by JM.

In the photospheric case, the situation is better for the transverse field, and a little worse for the longitudinal; the contrary is true in the umbral model, but, again, we remain in the 20% of error regime.

Note that the errors are all positive, i.e., the derivative calibration gives a systematic underestimate of the real field.

#### 4.b Effects of spectral smearing. FPI

No mention of the effects of spectral smearing is given in JM but, as we saw before, the presence of a smearing function introduces significant changes respect to the original situation.

Figs. 28 and 29 are the correspondent of 25 and 27, for profiles convolved with the FPI transmission profile (FWHM=150 mÅ).

For  $B_L$  we see that there is a smaller error for the case of pure longitudinal field at all wavelengths, and that the convolution has somehow reduced the "wild" behaviors in the wavelengths close to line center, but the differences among inclinations are bigger than before; we saw in Sect. 3.b that the ratio  $V/I$  is more homogeneous for the convolved profiles respect to the original ones, so the cause of this discrepancy must belong to the factor  $dI/d\lambda$ .

Indeed, the derivative of the convolved intensity profiles is strongly dependent on the  $\gamma$  values; something similar to the effect described in Sect. 3.b about the fractional linear polarisation is happening here too: the convolution process "brings" part of the signal at line center, extremely dependent on the field and the inclination, to the wings, causing the behavior shown in Fig. 28. So, the best that we can say is that, in the range of wavelengths 6122.0-6122.06 Å, the errors for  $B_L$  remain within the 20%.

The transverse field (Fig. 29) shows tremendously enhanced errors and a very large spread within different inclinations.

The reason for the increase in the error curves is easily understood looking at formula (8): the proportionality between the linear polarisation and the slope of the intensity profile is ruled not by the  $B_T$  only, but also by the numerical factor  $\Delta\lambda$ , that, being the offset from line center, doesn't change either we convolve the profiles or not. In the un-smear profiles, the shapes of  $Q$  ( $U$ ) and  $dI/d\lambda$  are steep enough to compensate for the  $\Delta\lambda$  factor, while this is not true for the convolved profiles. Fig. 30 visualizes the point: using the original  $U$ ,  $Q$ ,  $I$ , the quantity defined by (8) asymptotically tends to the input field; using the convolved ones, the trend that we get is basically the shape of  $\Delta\lambda$ .

We need, therefore, an "effective"  $\Delta\lambda$ , somehow weighted with the spectral transmission profile of the FPI<sup>6</sup>, but of course not dependent on the field strength or the inclination value.

The best way we could think to determine this  $\Delta\lambda_{eff}$  was just a trial-and-error method, trying to minimise the error curves of Fig. 29.; for the penumbral and umbral models, and wavelengths in the interval 6122.0-6122.06 Å, the best value of  $\Delta\lambda_{eff}$  is  $\sim 0.65 \times \Delta\lambda$ , while for the photospheric model is  $\sim 0.5 \times \Delta\lambda$ .

Fig. 31 shows these "new" error curves, that now start and end within  $\pm 30\%$ ; however, the big dependence on the  $\gamma$  values is still present, a little enhanced respect to the un-convolved curves.

#### 4.c Effects of spectral smearing. Blocker

As described in Sect. 3.c, the net effect of the blocker is to reduce the intensity transmission of an appreciable quantity, even if positioned at the working wavelength, while the polarization signals are less affected.

This implies that the factor  $dI/d\lambda$  will be smaller and, using the derivative calibration, the output field will be an overestimate of the true one. The error curves of Fig. 28 will therefore shift towards more negative values, even though they will keep the same shape; the amount of the shift can be as large as 10%.

The shift for  $B_T$  is limited to  $\sim 3\%$ , since the factor  $dI/d\lambda$  is under square root (Eq. (8)). Fig. 32 shows the same error curves of Figs. 28 and 31, for  $B_L$  and  $B_T$  and a smaller range of wavelengths, considering the blocker factor.

Another possible source of errors is the misplacing of the blocker. The transmission of the blocker falls off quite rapidly, respect to the width of the line, and therefore a misplacing of even few tenths of mÅ respect to the working wavelength causes noticeable differences. The net result

<sup>6</sup>The straight convolution won't be useful, since the operator convolution doesn't commute with the operator multiplication.

depends on the amount and direction of the blocker shift: Fig. 33 shows (in the same format as Fig. 32) the error curves for a shift of the blocker of 40 mÅ, Fig. 34 for a shift of -40 mÅ. A precise tuning of the blocker is hence an absolute necessity for this calibration technique.

#### 4.d Effects of finite difference

All the previous curves have been computed using the "analytic" derivative of the profiles; with the real data we have to use a finite difference between intensities at 2 different wavelengths positions in the wing of the line. Here we will consider the effects of doing so, but for profiles convolved with the FPI alone.

The estimate of the derivative will be close to the real value if the separation in wavelength of the intensities images is small, but on the other hand if the images are too close, the corresponding signal will be too low to detect. Considering the convolved intensity profiles, an interval of 20 mÅ will give a  $dI/I \sim 2-3\%$ , that we can detect.

Given the working wavelength  $\lambda_i$ , we can estimate the derivative either as  $\Delta I = I_{\lambda_i} - I_{\lambda_{i-2}}$  or  $\Delta I = I_{\lambda_{i+2}} - I_{\lambda_i}$ ; In the first case we have a value bigger than the real one, in the second a value smaller. This translates into a shift of the error curves  $\leq 5\%$ , as shown in Fig. 35. As explained in Sect. 4.c, the presence of the blocker introduces an overestimate of the field that can be as big as 10% in the  $B_L$  case; to avoid that the error introduced by the finite difference sums with this, we need to use the  $\Delta I = I_{\lambda_{i+2}} - I_{\lambda_i}$  as estimate of the derivative.

### 5. DETERMINATION OF THE AZIMUTH

The azimuth of the field,  $\chi$ , is usually determined through the formula:

$$\chi = 0.5 \arctan(U/Q) \quad (9)$$

Its value should be wavelength-independent, as far as we remain in the line wings. Fig. 36 shows the values of the azimuth (input  $\chi = 0^\circ$ ) determined with eq. (9), for the same range of wavelengths of the previous figures. For the case of pure transverse field ( $\gamma = 0^\circ$ ) the output value is perfectly zero, but for the other inclinations, and for small fields, there is an error  $\leq 10^\circ$ . At bigger fields, the error tends asymptotically to zero; for wavelengths closer to the line center, though, the errors increase again.

When we convolve with the usual Fabry-Perot profile of 150 mÅ FWHM, the curves become more homogeneous, and we have an undetermination of  $10 - 12^\circ$ , for all the wavelengths, up to 800 G; over this value the errors reduce to  $\sim 5^\circ$  (Fig. 37).

### 6. SUMMARY AND CONCLUSIONS

As mentioned in the Introduction, the conversion of polarization into magnetic fields is a real difficult task and, indeed, what we saw in the previous sections is not very encouraging. We analysed two methods that could be suitable for the calibration of Vector Magnetographs, the *derivative* method and the *calibration curve* method, and commented the determination of the azimuth of the field. Here we will try to summarize the results, and give some suggestions for further improvements.

*Se Atene piange ...*

*Derivative method.* The derivative calibration method works reasonably well if we go in the far wings of the line; here, the average errors lie within 15-20%, both for longitudinal and transverse fields, up to 1500-2000 G (Figs. 25 and 27). However, this is not a general statement, since the range of validity greatly changes from line to line.

When we introduce a convolution factor, as in the case of a filter magnetograph, things change

drastically: the errors are somehow still acceptable in the  $B_L$  case, but for  $B_T$  we go up to 30% or more, and there is a strong dependence of these errors to the inclination of the field,  $\gamma$ . A filter with a narrower passband respect the one actually present in the SVMG would reduce this effects. The presence of the blocker is another source of error to consider using this method (Figs. 32-34). The two major problems are its very narrow transmission profile respect to the width of the line and its not completely reliable tunability; a tunable blocker with a bigger passband ( $\sim 1.5$  Å FWHM, but not more, since the adjacent orders of the FPI lie at  $\sim 3.3$  Å apart) would much improve the situation.

The method is not much affected by velocity effects or by "model dependence", in the sense that the errors are comparable in the range of wavelength 6122.0-6122.06 Å and for the three models. The necessity of using finite differences instead of "analytical" derivatives doesn't introduce errors too big ( $\leq 5\%$ ), if we limit the step to 20-30 mÅ, since the line is wide enough to change very smoothly in this interval. The same wouldn't be true with a narrower line, like the FeI 5250 (see Caussí *et al.*, 1991). Since we are subtracting images acquired at different wavelengths, though, we must pay special attention to some factors, like eventual dependence on wavelength of the transmission of the instrument, differences in the transparency of the sky, etc. The derivative factor seems to be extremely sensitive to misalignments of the images, and this can be a serious problem in the actual version of the SVMG, since the intensity images are constructed on a quite long time lap (between 20 sec, in the "old" mode, and 20 minutes, in the "new" one), with the unavoidable motion of the features in the FOV. A smooth of the intensity images before the subtraction will improve the situation.

In summary, in the actual version of the SVMG, the derivative method can give us results with an indetermination of 30% or worse.

#### ... *Sparta non ride*

*Calibration curve method.* As seen in Sect. 3.a, the relationships between fractional polarisation and magnetic fields are not completely linear, even after the convolution with a filter 150 mÅ wide, and therefore the use of Eqs. (3) and (4) as calibration curves gives us errors that can be up to 12% for the  $B_T$  case. However, we could solve the issue using different curves, like a power law for the linear polarisation.

The convolution with the FPI profile increases the linearity of the curves, but has two opposite effects on the differences due to the inclination values for  $B_L$  and  $B_T$  (Figs. 11 and 12). A filter with a narrower passband would be better for the transverse field, even though quite big differences are present in the original profiles, but would reduce the homogeneity of the curves for the longitudinal field, and vice versa.

The blocker doesn't affect much the precision of the method.

Errors intrinsic in the method, as described in sect. 3.d, are due to velocity and inclination effects, and lead to a total error that could be as big as 30%; an accurate choice of the calibration curve could however minimise the effects due to the  $\gamma$  values.

The problems introduced by the choice of a particular model could be overcome adopting the right model for each feature in the FOV, even if this will heavily affect the computational time; in any case the uncertainties of the models themselves, or in the determination of which model to use for a particular point, will remain.

In summary, once we trust and adopt a particular atmospheric model, the calibration curve method can give us results with an indetermination (internal consistence?) of  $\sim 20\%$ . This result is not strongly affected by the characteristics of the SVMG, but will equally apply to any filter magnetograph.

Both the methods will suffer by the presence of scattered light; as an example, the Marshall group corrects for scattered light comparing their results with the values of Mt. Wilson (obtained spectrographically), and the correction factor is around 8 (see Hagyard *et al.*, 1988, App. E).

All this considerations, plus the comments of Sect. 5, lead us to some conclusions:

1. The derivative method will work better with a very narrow filter (we think that the method would be very suitable for spectrographic observations) and needs a tunable blocker so that the global transmission profile is the one of the filter only. An additional improvement would come by speeding up the acquisition rate. The method is, however, not suitable for all the lines: small  $\Delta\lambda_D$  values will greatly reduce the range of validity of the WFA.
2. If we choose to use the calibration curve method, the filter shouldn't have a passband smaller than  $\sim 100$  mÅ, or there will be too much room for errors related to velocity fields (Hagyard *et al.*, 1988, Chap. 5); over this value, there are equivalent pros and cons, as reminded above. The method is most suitable for lines with a high  $g_L$  factor, since this will improve the polarization signal.
3. In any case, the vector magnetic fields that we can determine with filter magnetographs are, at the best, a very rough estimate of the real quantities; we can expect errors of 2-500 G in the transverse field, up to 200 G for the longitudinal, and  $\sim 10^\circ$  for the azimuth. This is based *only* on the analysis of the calibration methods, i.e. without considering other sources of noise, like instrumental polarisation, scattered light, inhomogeneities in the transmission, etc. Nevertheless, a filter magnetograph can give us information about the whole structure of an active region, with a good spatial resolution and, in general, we'll be able to follow the temporal evolution of the structures in considerable detail.

## 7. ACKNOWLEDGEMENTS

We wish to thank G. Murphy for kindly provide his SPSR code, and many hints on how to use it; K.S. Balasubramanian for many useful discussions. This work was completed while the author was holding a National Research Council Resident Associateship.

## 8. REFERENCES

- Ai, G.: 1987, *Pub. Beijing Astronomical Obs.* **9**, 27.
- Cauzzi, G., Smaldone, L.A., Balasubramanian, K.S. and Keil, S.L.: 1991, *On the calibration of line-of-sight magnetograms*, submitted to *Solar Physics*.
- Duncan, D.D. and Thomas, M.E.: 1987, *Fourier Transform Spectrometer Evaluation of Fabry-Perot Etalon ET75/1*, JHU/APL Memorandum F1F(4)87-U-209.
- Hagyard, M.J.: 1988, *Solar Physics* **115**, 107.
- Hagyard, M.J., Gary, G.A. and West, E.A.: 1988, *The SAMEX Vector Magnetograph*, NASA Technical Memorandum 4048, MSFC, Huntsville, Ala.
- Hernandez, G.: 1986, *Fabry-Perot Interferometers*, Cambridge Univ. Press, Cambridge.
- Jefferies, J.T., Lites, B.W. and Skumanich, A.: 1989, *Astrophys. J.* **343**, 920.
- Jefferies, J.T. and Mickey, D.L.: 1991, *Astrophys. J.* **372**, 694.
- Kjeldseth-Moe, O. and Maltby, P.: 1969, *Solar Physics* **8**, 275.
- Lites, B.W. and Skumanich, A.: 1984, in *Measurements of Solar Vector Magnetic Fields*, M.J. Hagyard ed., NASA Conference Publication 2374, Pag. 342.
- Lundstedt, H., Johannesson, A., Scharmer, G., Stenflo, J.O., Kusoffsky, U. and Larsson, B.: 1991, *Solar Physics* **132**, 233.
- Maltby, P., Avrett, E.H., Carlsson, M., Kjeldseth-Moe, O., Kurucs, R.L and Loeser, R.: 1986, *Astrophys. J.* **306**, 284.
- Rees, D.E., Murphy, G.A. and Durrant, C.J.: 1989, *Astrophys. J.* **339**, 1093.
- Rust, D.M. and O'Byrne, J.W.: 1991, in *Solar Polarimetry*, Proceedings of 11<sup>th</sup> NSO Summer workshop, L.J. November ed., Sunspot, NM, Pag. 74.

Skumanich, A. and Lites, B.W.: 1987, *Astrophys. J.* 322, 473.  
Title, A.M., Tarbell, T.D. and Topka, K.P.: 1987, *Astrophys. J.* 317, 892.  
Vernassa, J.E., Avrett, E.H. and Loeser, R.: 1981, *Astrophys. J., Suppl. Ser.* 45, 635.  
Zirin, H.: 1985, *Australian J. Phys.* 38, 961.

## FIGURE CAPTIONS

**Fig. 1a.** SVMG Etalon ET75 transmission profile. The transmission has been arbitrarily set to 50%.

**Fig. 1b.** Same plot, for the interference blocker, at  $T \sim 50^\circ\text{C}$  and tilt  $= 0^\circ$ . The transmission value is  $\sim 27\%$ .

**Fig. 2.** Plots of the Stokes I (solid) and V (dashed) for CaI 6122, photospheric model, and 3 different sets of magnetic parameters. The max. circular polarization is  $\sim 20\%$ .

**Fig. 3.** As Fig. 2, but for Stokes Q (solid) and U (dashed). The maximum signal is 10%, for the case of  $\gamma = 60^\circ$ .

**Figs. 4-5.** As Figs. 2-3, for Moe-Maltby penumbral model.

**Figs. 6-7.** As Figs. 2-3, for Maltby umbral model.

**Fig. 8.** Fractional circular polarization vs input longitudinal B, for the penumbral model. The signal increases towards line center, but the same do magneto-optical effects,  $\gamma$  dependence etc.

**Fig. 9.** Fractional linear polarization vs input transverse B, for the penumbral model. The same considerations of Fig. 8 apply. The signal is extremely small for fields  $\leq 500$  G.

**Fig. 10.** The same of Fig. 9, but on logarithmic scale. A value of linear polarization of  $10^{-4}$  corresponds to 1-200 G.

**Fig. 11.** Effect of the FPI (spectral selector) on the Stokes profiles. The curves are shallower than the original ones, but the values of fractional polarization are bigger, in the far wings of the line. The details of Q and U at line center have been washed out almost completely.

**Figs. 12-13-14.** Analogous of Figs. 8-9-10, but considering the spectral smearing introduced by the Fabry-Perot. There is a strong  $\gamma$  dependence in the linear polarization.

**Fig. 15.** a) Q profiles for the same input  $B_T$  (750 G) but for two different inclinations ( $\gamma = 90$  and  $30^\circ$ ). The signal is similar in the far wings. b) The same as before, but convolved with the FPI transmission profile (FWHM = 150 mÅ). The signal even in the far wings is very different.

**Fig. 16.** Effects of the blocker prefilter on the Stokes parameters.

**Figs. 17-18-19.** Analogous of 12-13-14, but introducing the blocker factor. These are the curves that will be used as calibration curves.

**Fig. 20.** a) B long. obtained from circular polarization correspondent to 3 different line-of-sight inclinations and calibrated with the mean curve, vs. the true B long. The errors lie within 10%. b) B long. obtained from circular polarization correspondent to 3 different wavelengths and calibrated with the mean curve, vs. the true B long. The errors are  $\sim 15\%$ .

**Fig. 21.** a)  $B$  tran. obtained from linear polarization correspondent to 3 different line-of-sight inclinations and calibrated with the *mean* curve, vs. the true  $B$  tran. The errors are pretty big, with a maximum of  $\sim 40\%$  for  $\gamma = 90^\circ$ . b)  $B$  tran. obtained from linear polarization correspondent to 3 different wavelengths and calibrated with the *mean* curve, vs. the true  $B$  tran. The errors are similar to those of **Fig. 20 b**).

**Fig. 22.** a) Effects of a wrong model. Umbral, penumbral and photospheric signal calibrated with a penumbral curve, for the case of  $B$  long. The errors can go up to a 30% for the photospheric signal. b) Same as a), for the transverse field. The errors remain within 15-20%.

**Fig. 23.** Mixing of different factors: wrong model, redshift of 1 Km/sec, different inclination, for the  $B_T$  case. The total error is around 50%.

**Fig. 24.**  $B$  longitudinal computed with the derivative method (for penumbral model, 3  $\gamma$  and 8 wavelengths as before) vs. input  $B$  long. No spectral smearing.

**Fig. 25.** Percentage error curves correspondent to the curves of **Fig. 24**. Far in the wings, the errors are within  $\sim 10\%$ .

**Figs. 26-27.** Analogous of **Figs. 24-25**, for the transverse field. The errors are worse in this case, especially for  $\gamma = 30$  and  $60^\circ$ .

**Fig. 28.** As **Fig. 25**, considering the spectral smearing introduced by the FPI. There is a bigger spread among inclinations than before.

**Fig. 29.** Like **Fig. 28**, but for  $B_T$ . The errors are tremendously increased, due to the factor  $\Delta\lambda$  in formula (8) in the text.

**Fig. 30.** Spectral behavior of the  $B_T$  computed with the derivative method, for un-smear (solid) and convolved (dashed) profiles. In the first case the output tends to the true value; in the second the shape of  $\Delta\lambda$  dominates.

**Fig. 31.** As **Fig. 29**, but introducing a factor  $\Delta\lambda_{eff} = 0.65\Delta\lambda$ . The errors remain within  $\pm 30\%$ , but the spread between inclinations is very big.

**Fig. 32.** Influence of the blocker in the derivative method. The global effect is to shift the curves towards more negative values (of about 10% for  $B_L$  and 3% for  $B_T$ ).

**Figs. 33-34.** Effects of blocker misplacing. In the first figure, the blocker is set at +40 mÅ respect to the working wavelength; in the second, to -40 mÅ.

**Fig. 35.** Effects of finite difference. The estimate of  $dI/d\lambda$  with a finite difference between intensity images brings a  $\pm 5\%$  error. Here the curves are shown for profiles convolved with the FPI only (no blocker).

**Fig. 36.** Azimuth determination for un-convolved profiles. The error remains  $\leq 10^\circ$  in all the situations.

**Fig. 37.** Same as 36, but for convolved profiles (FPI only). The errors are a little increased for smaller fields, but  $\sim 10^\circ$  again.

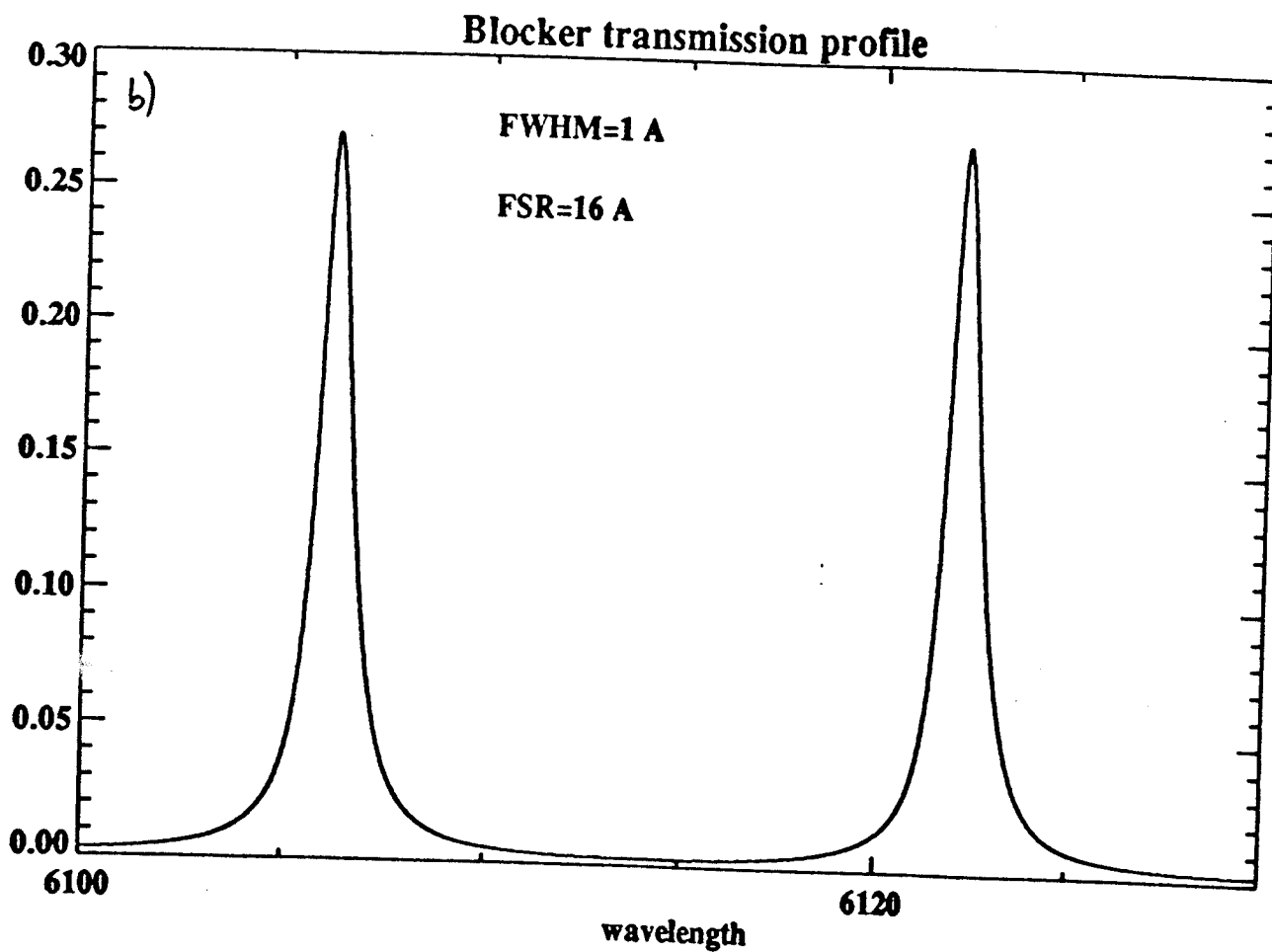
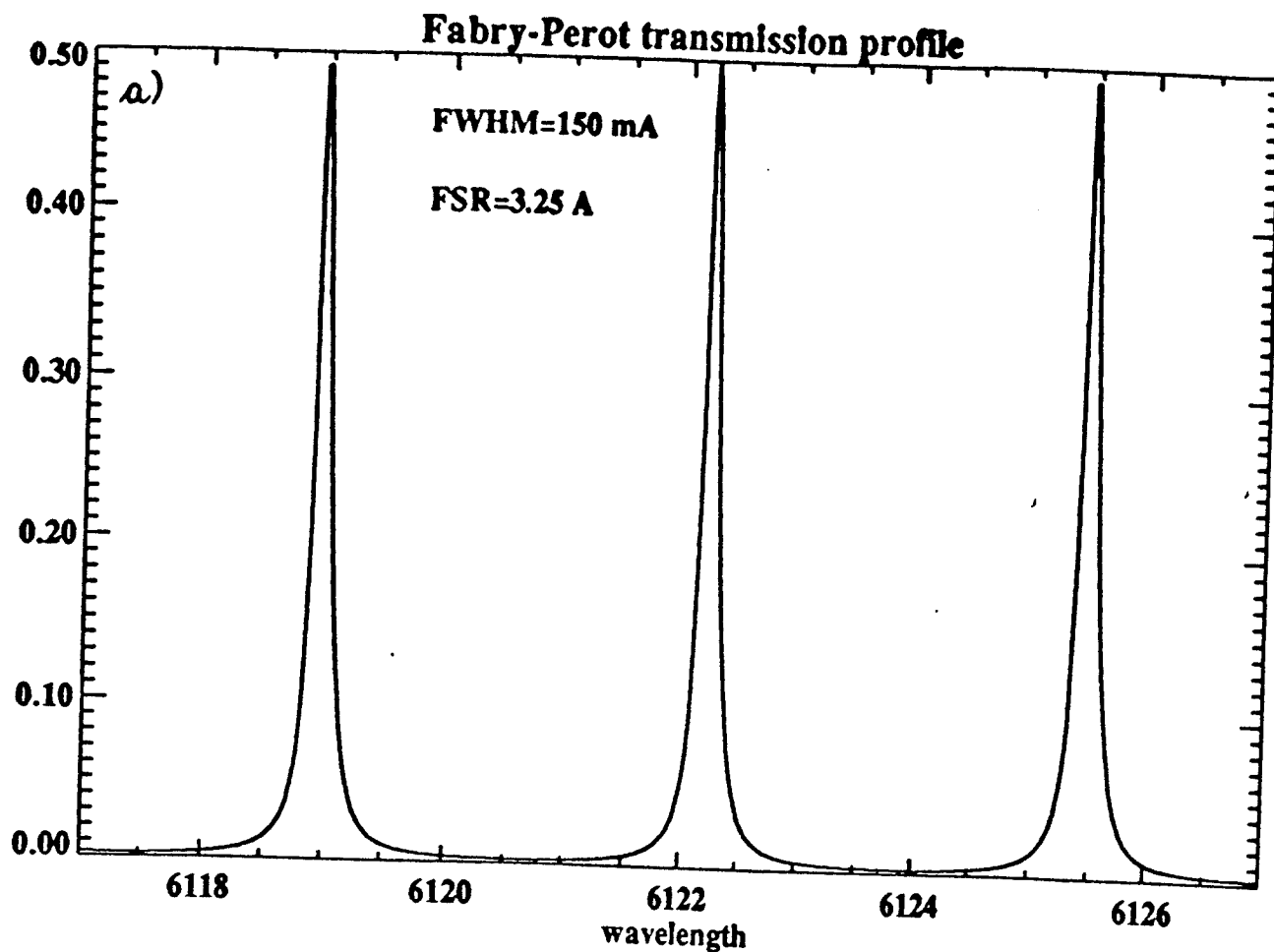


Fig 1.

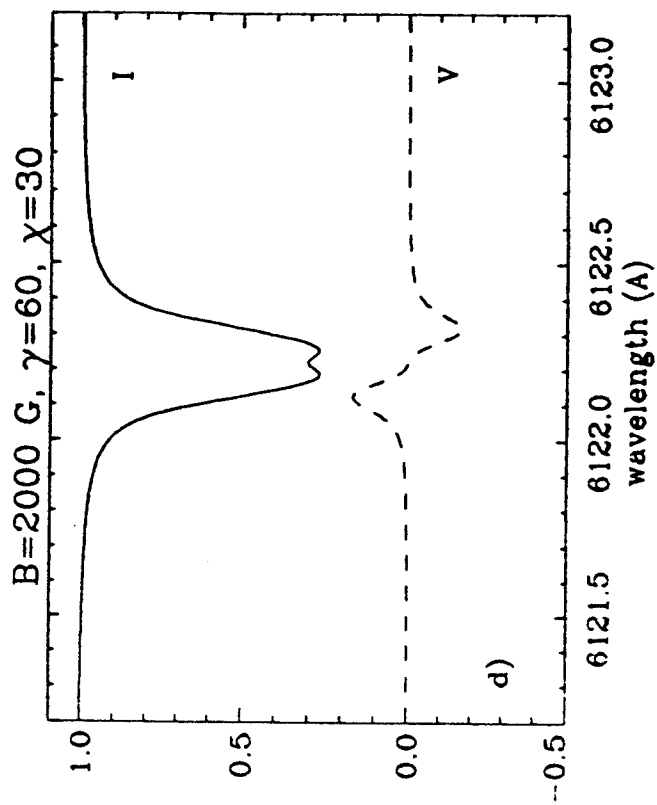
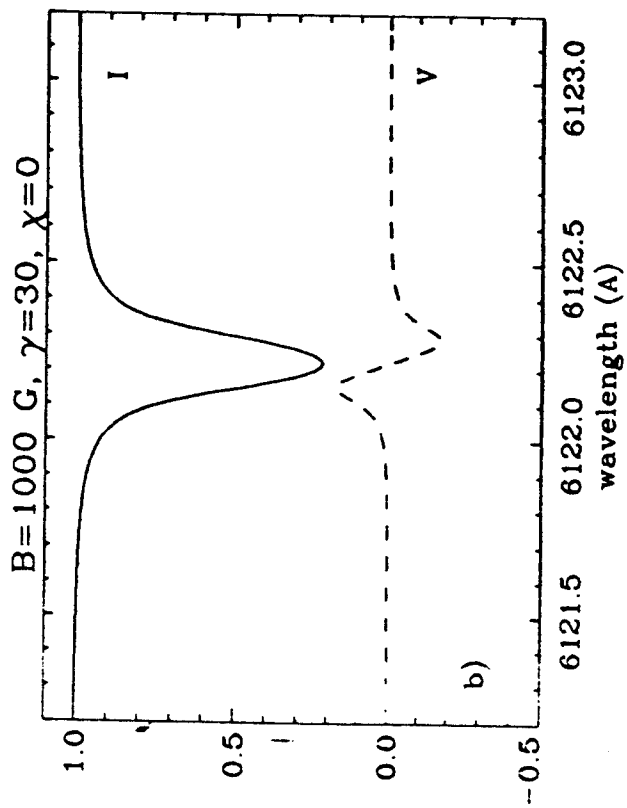
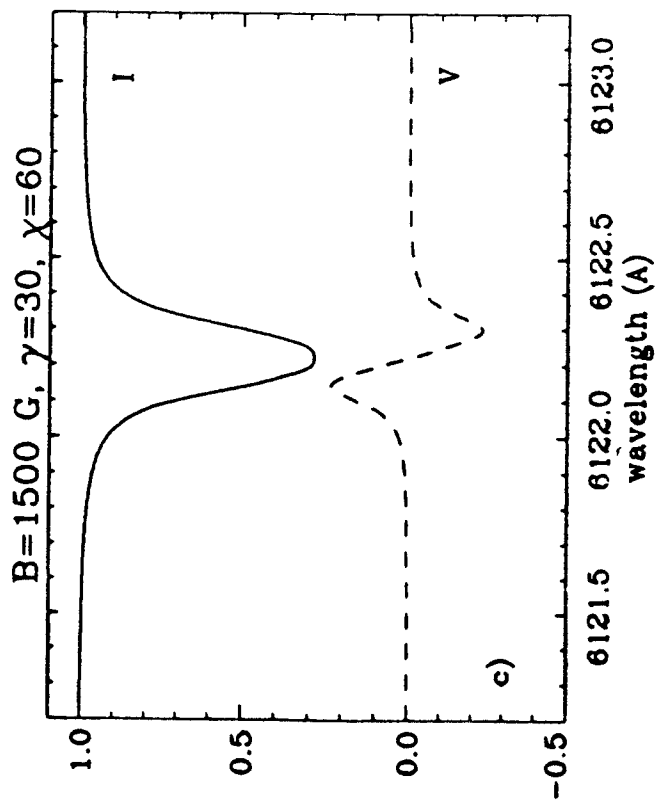
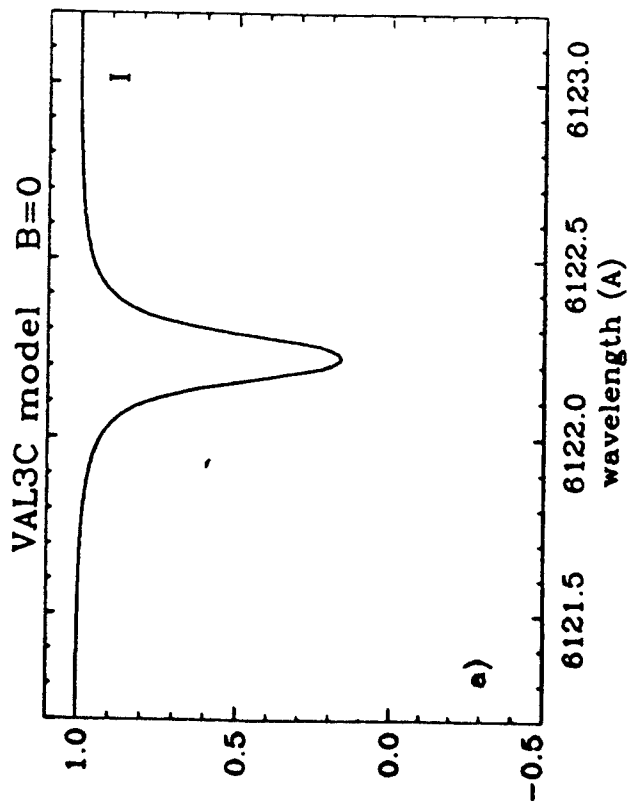


Fig 2.

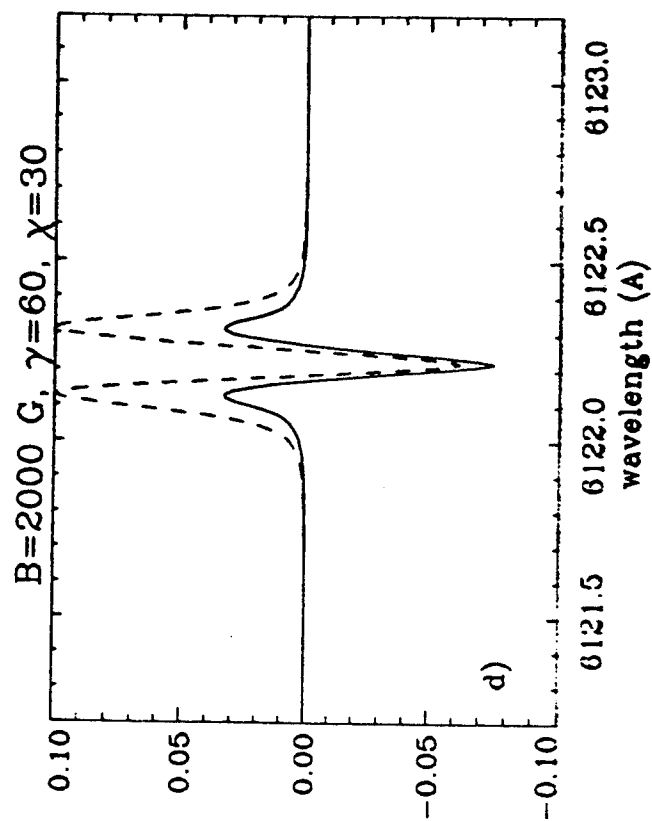
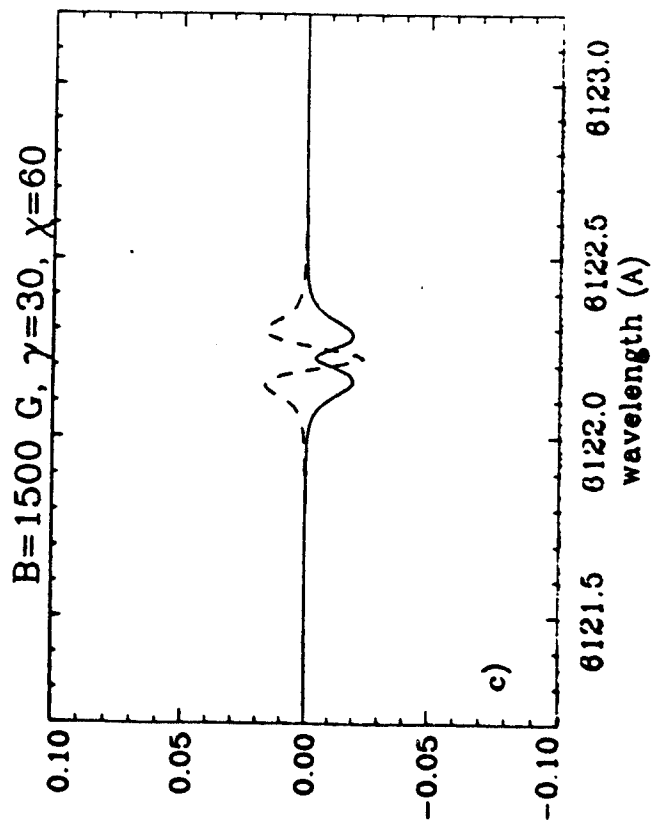
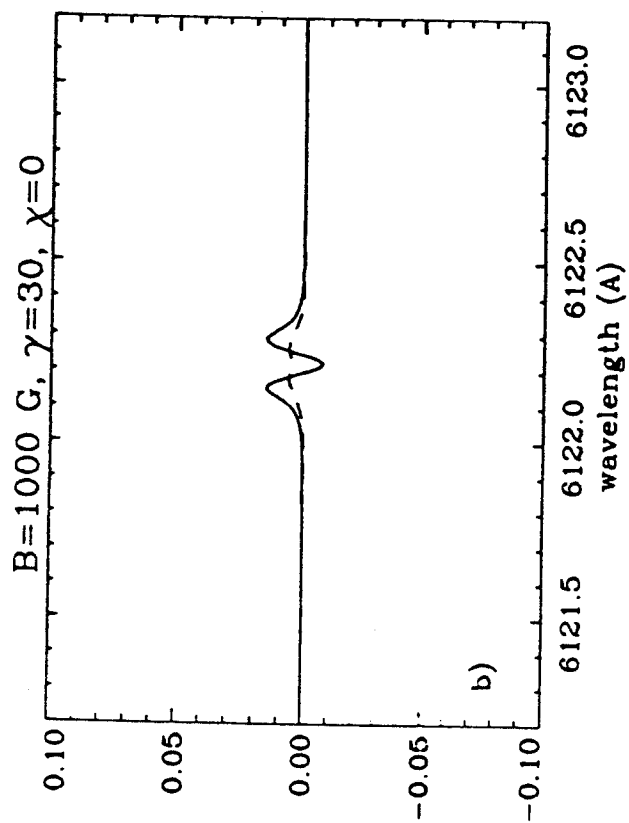
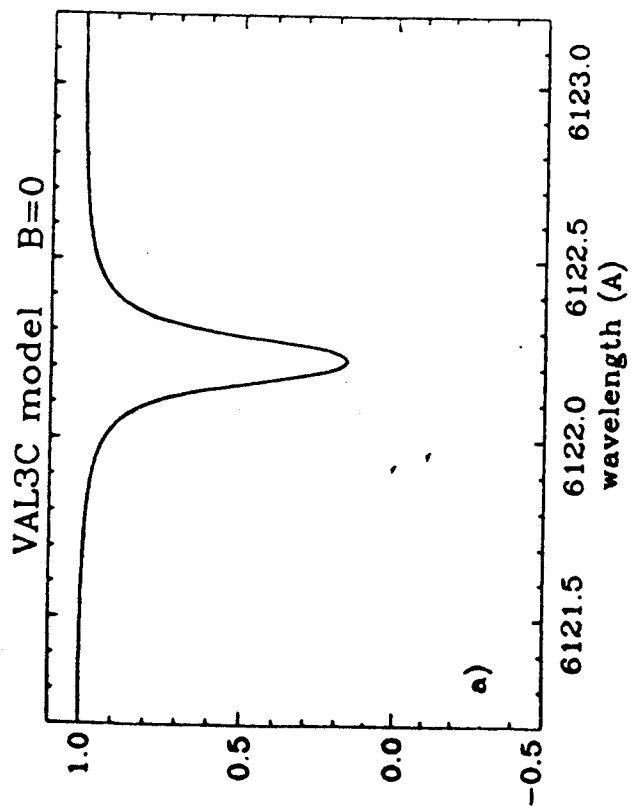


Fig. 3

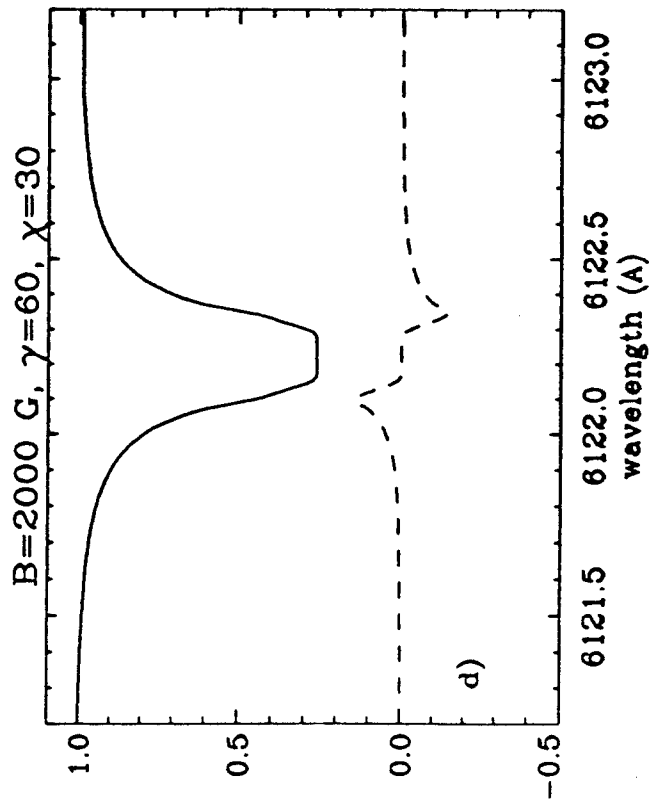
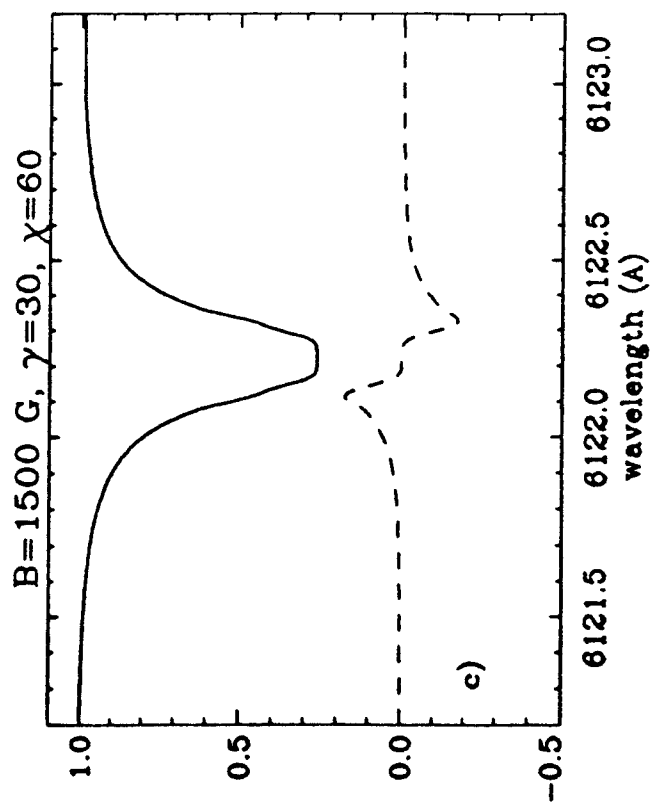
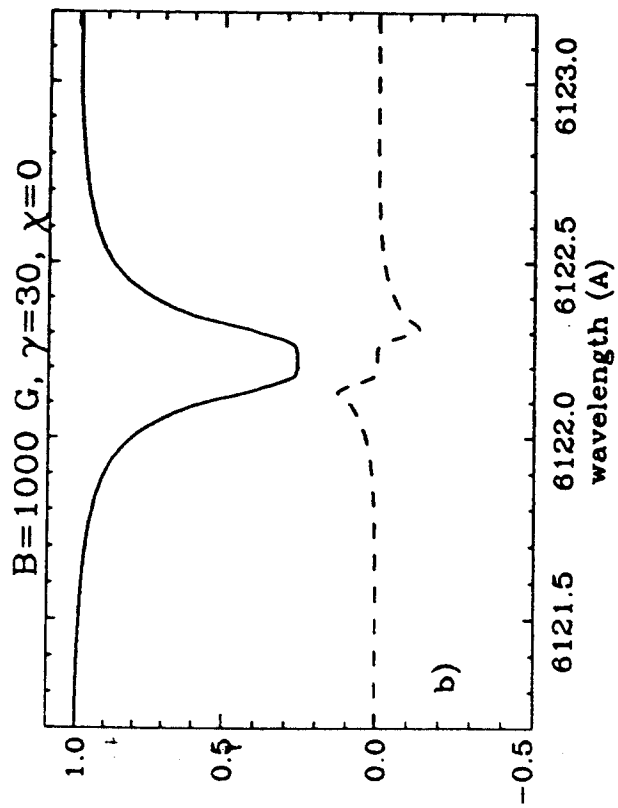
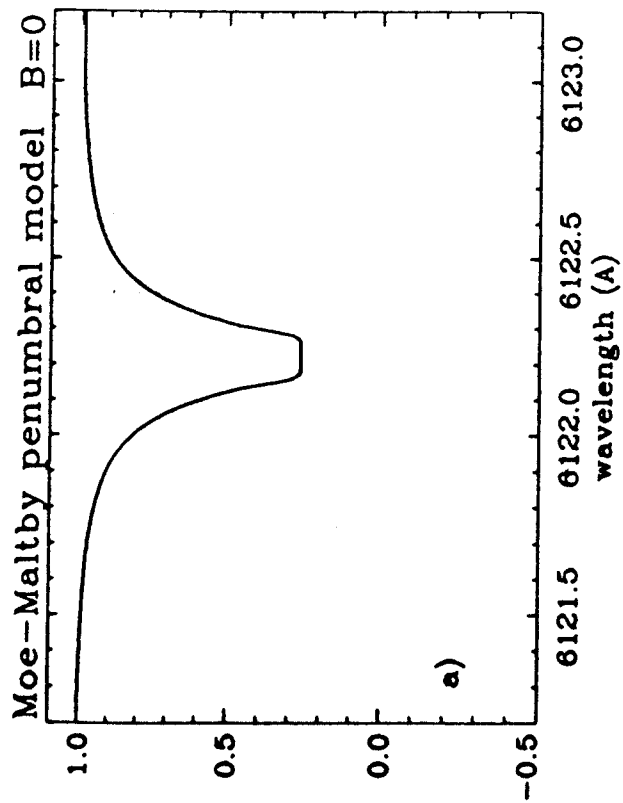


Fig 4

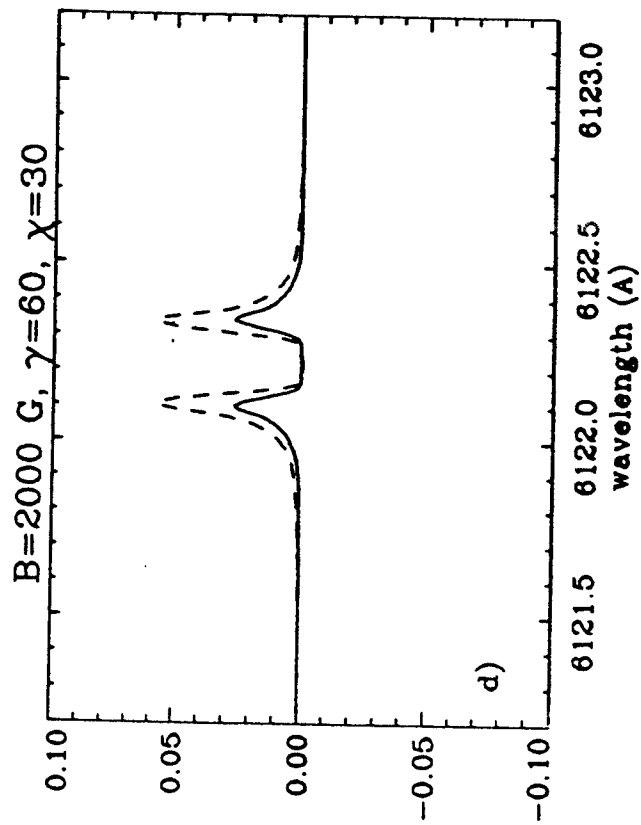
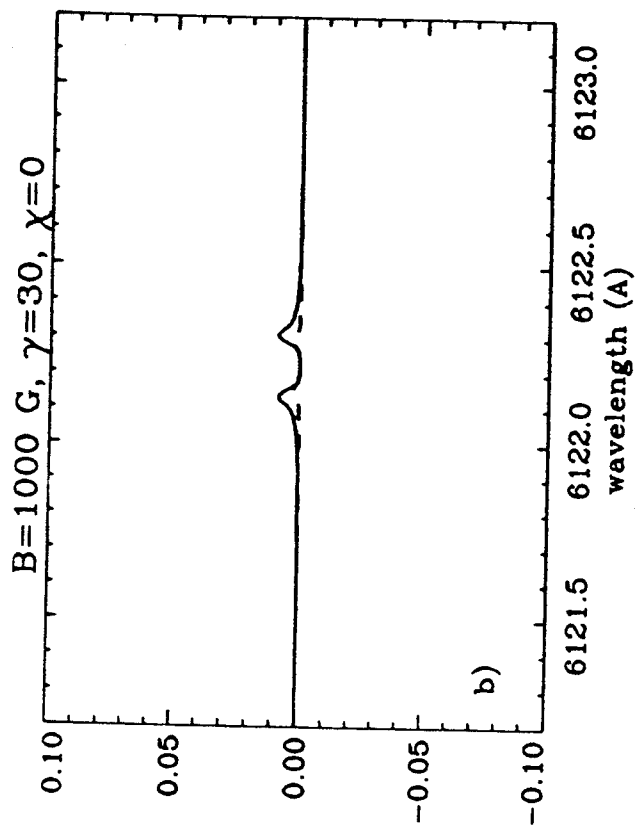
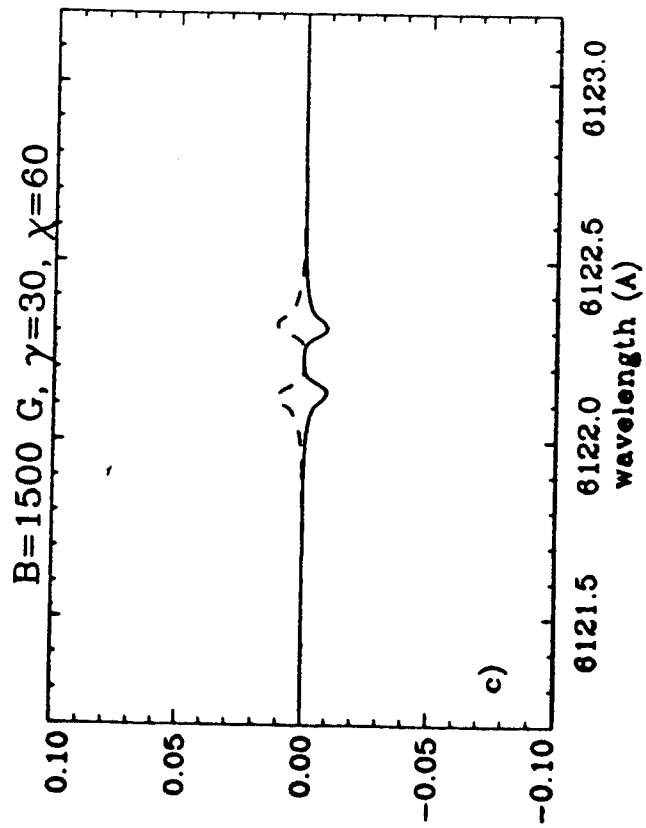
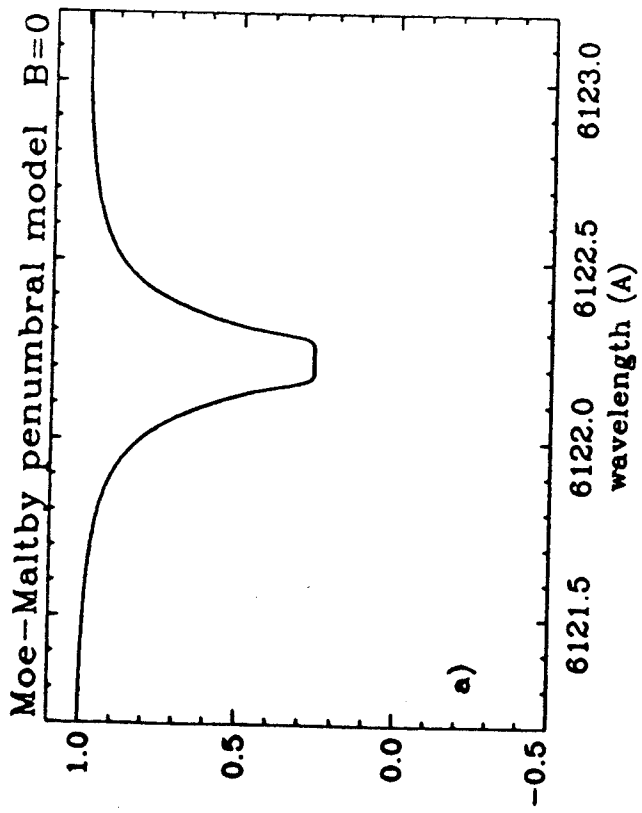


Fig 5.

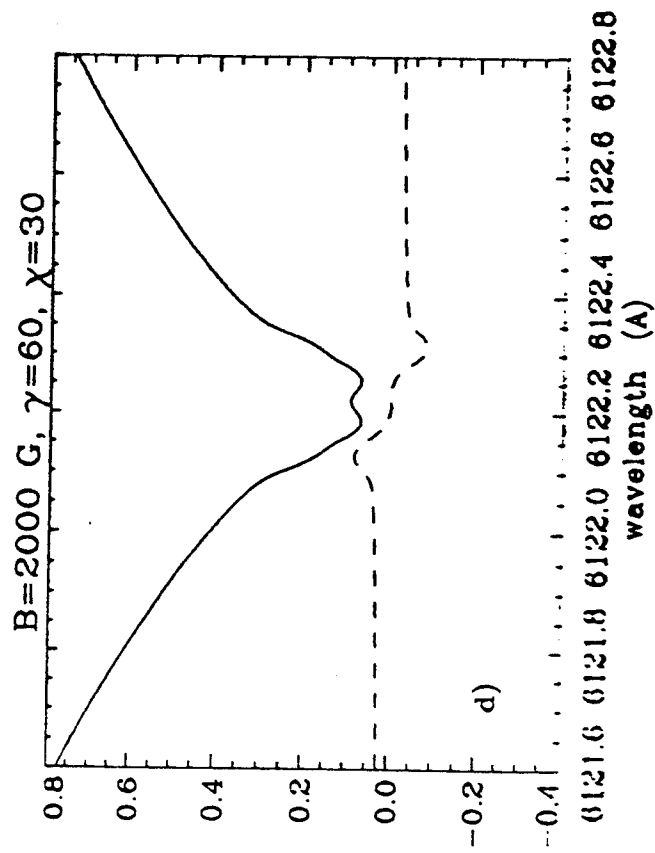
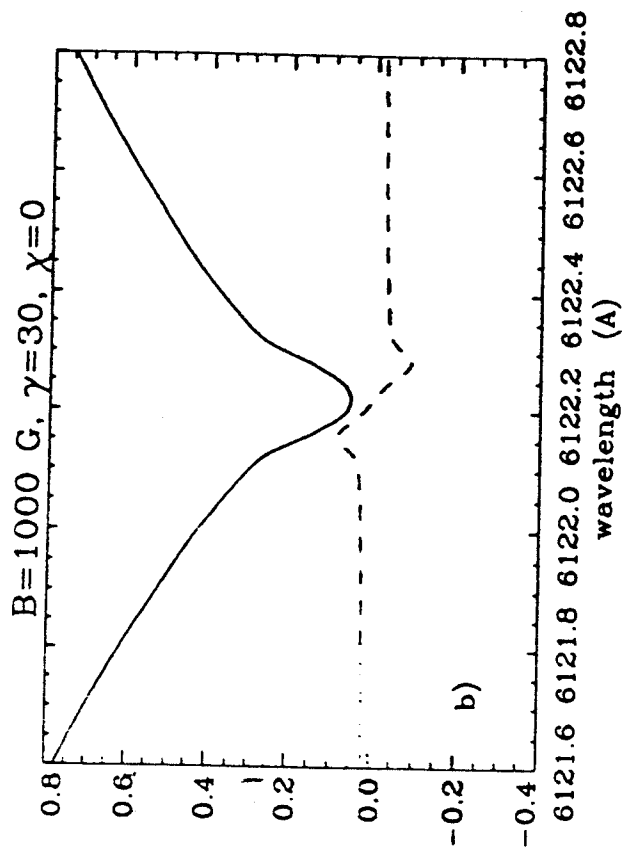
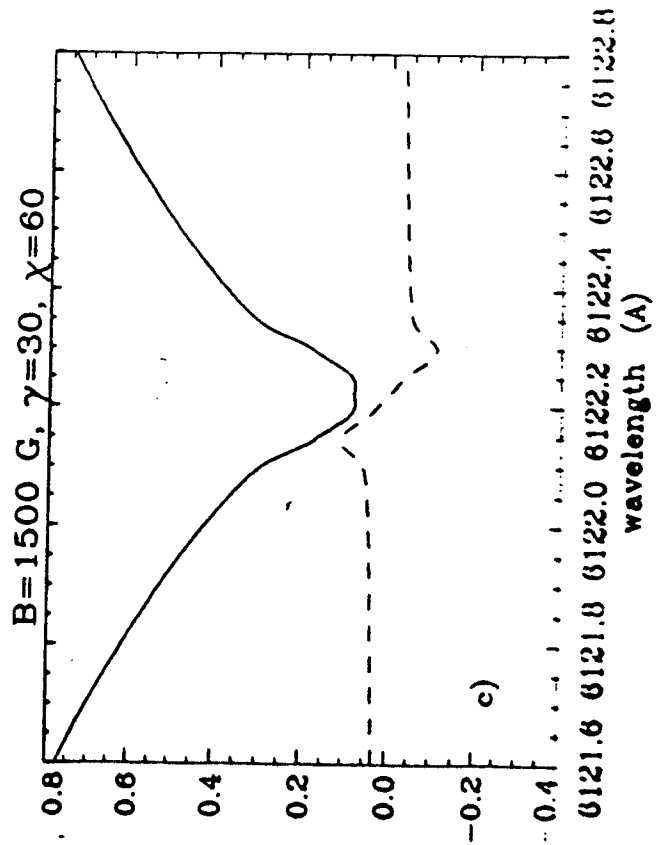
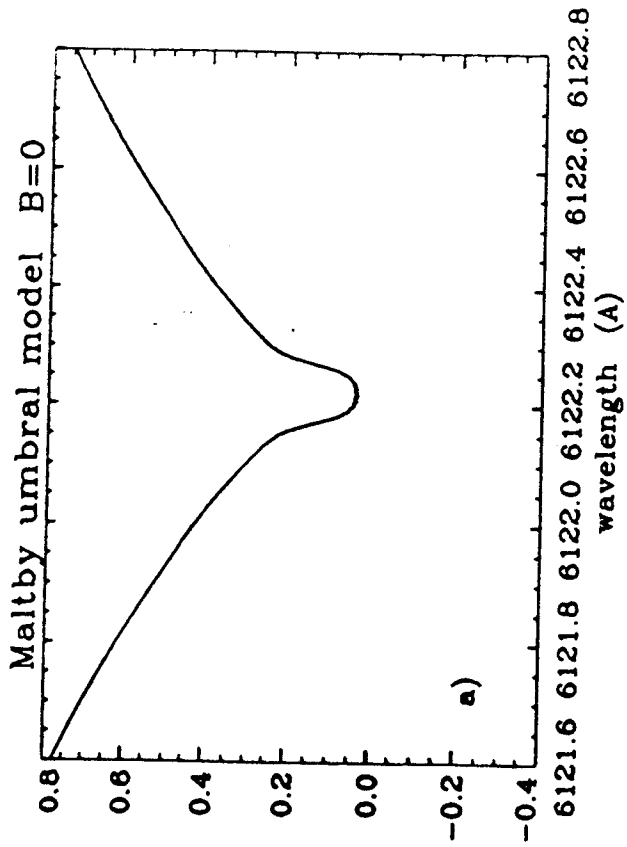


Fig 6

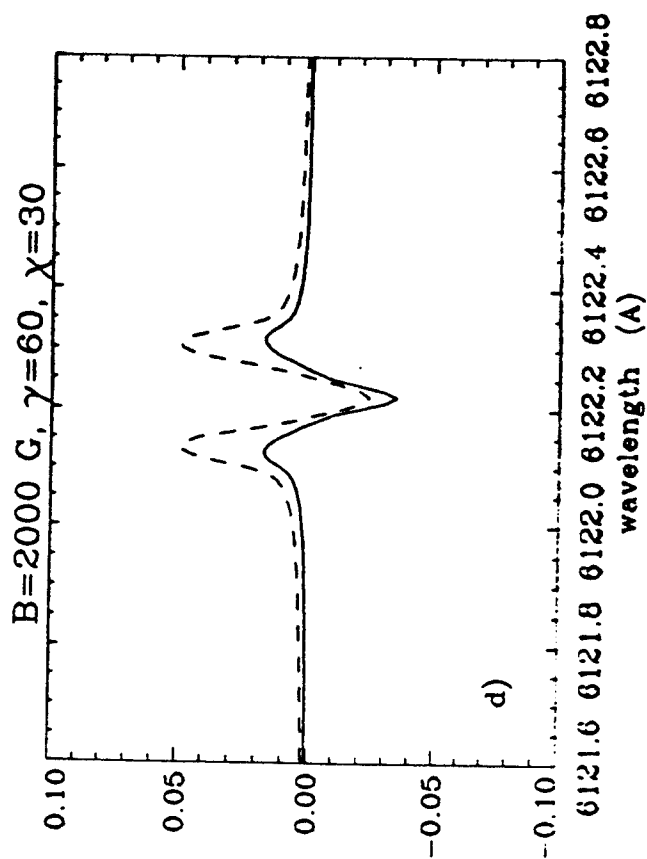
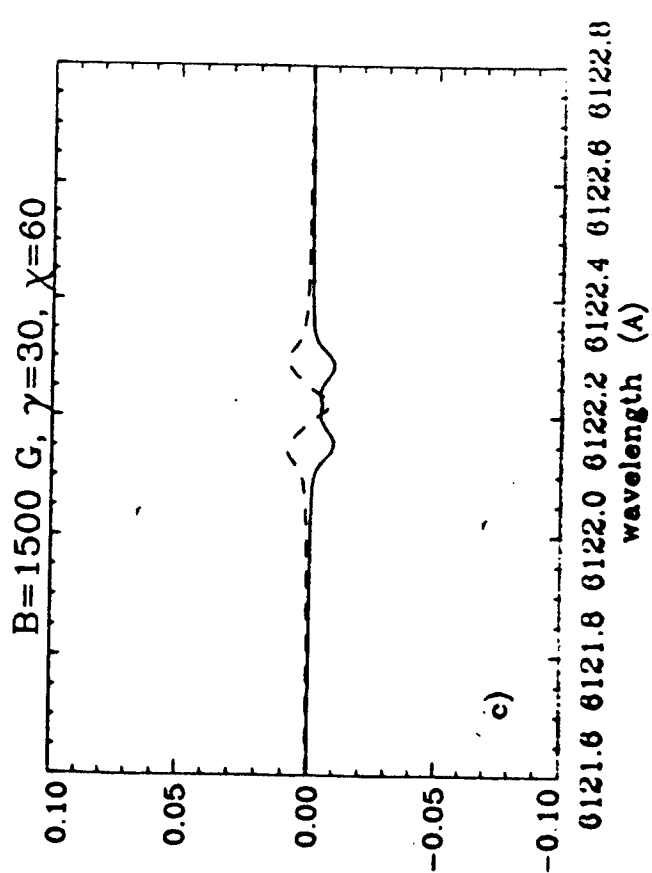
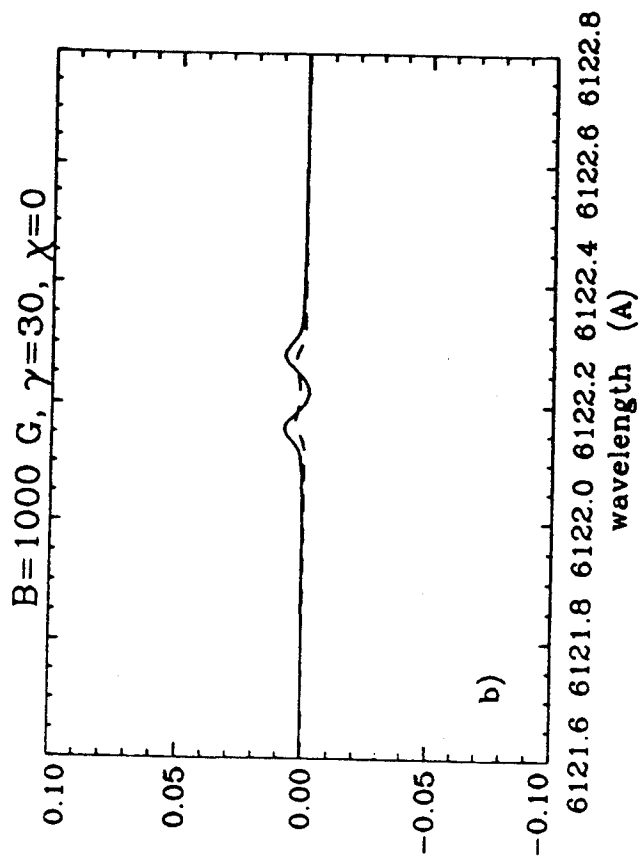
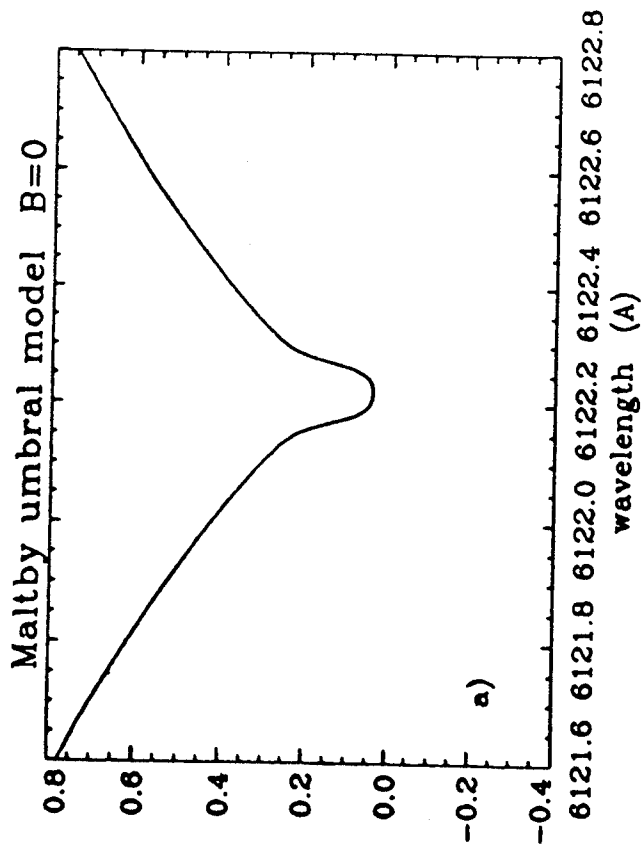


Fig 7.

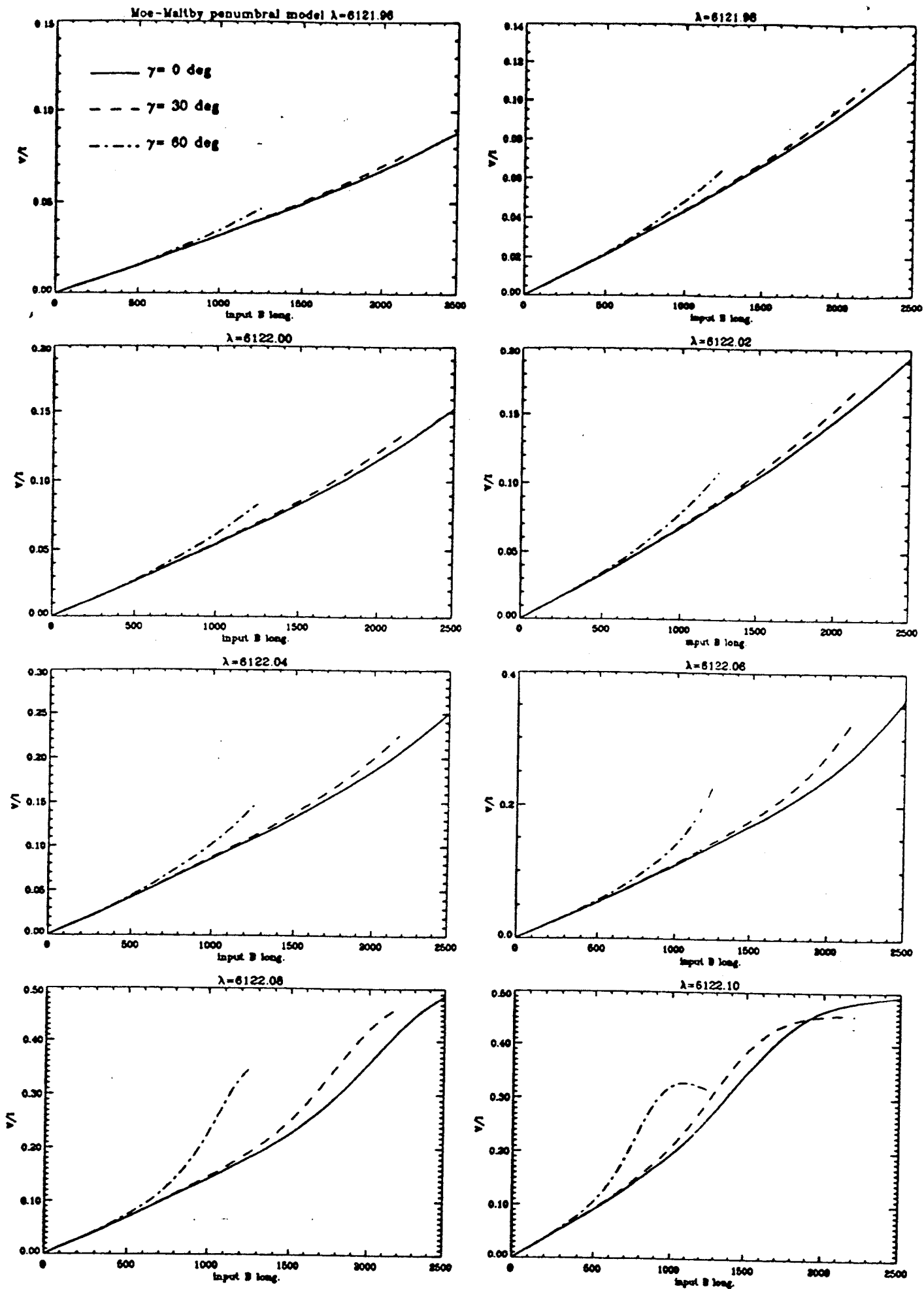
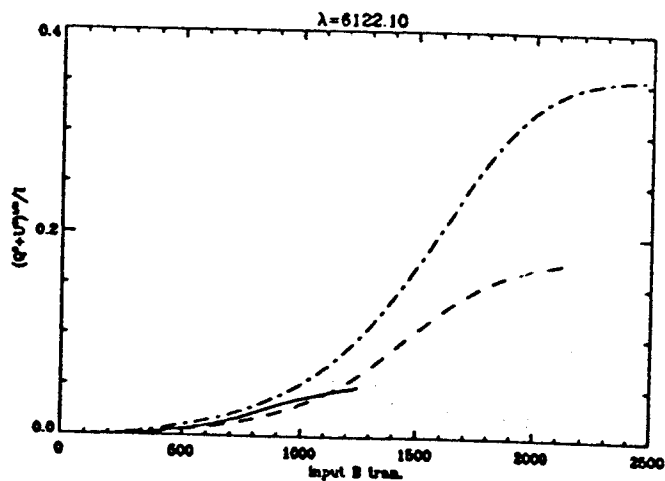
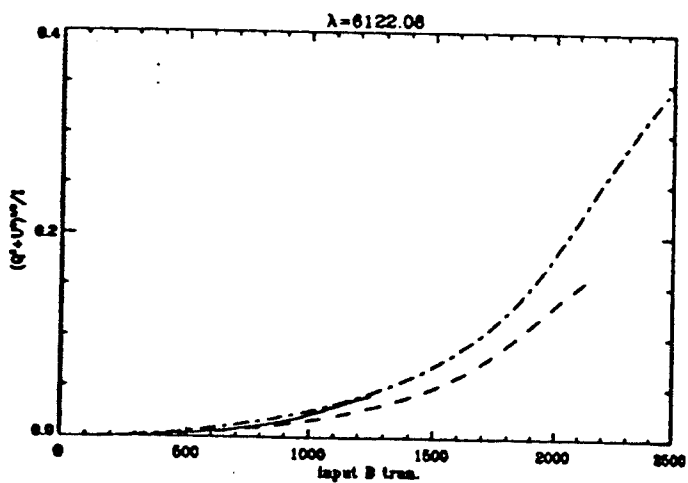
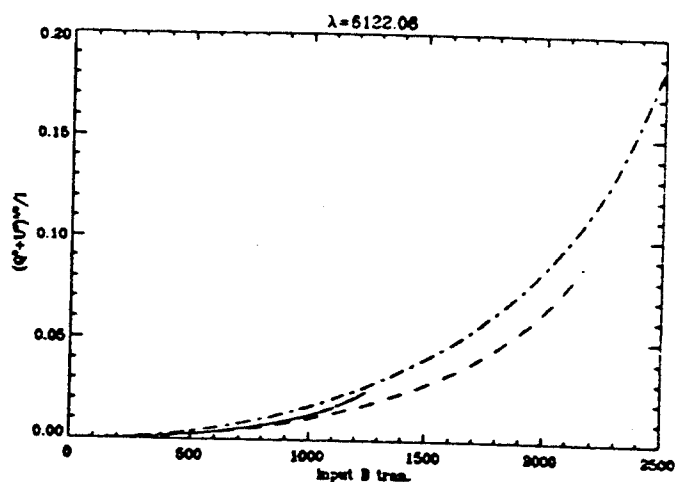
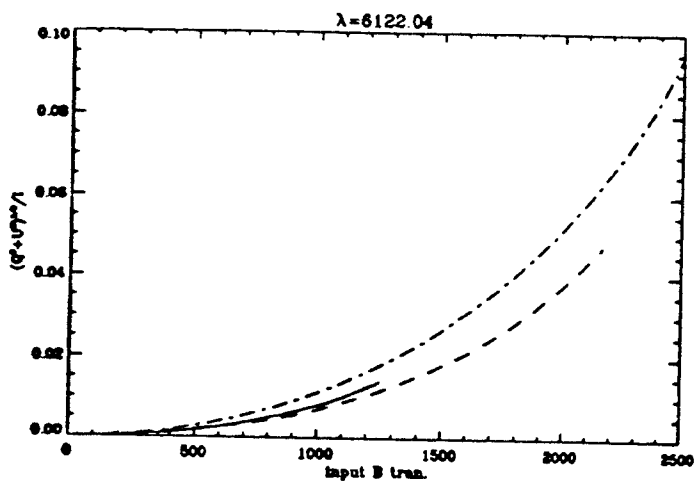
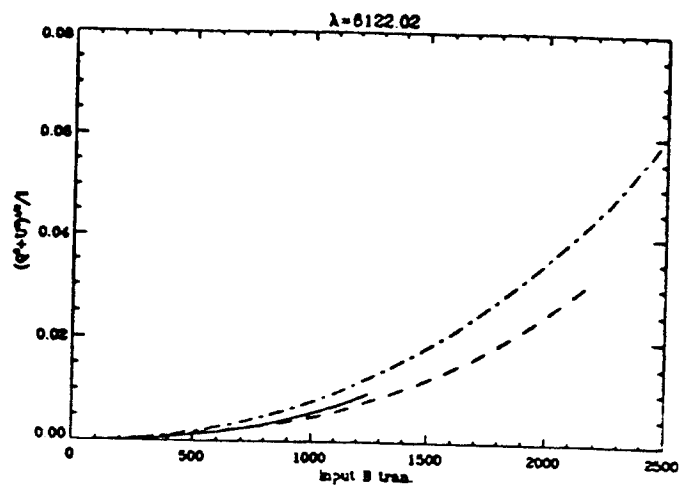
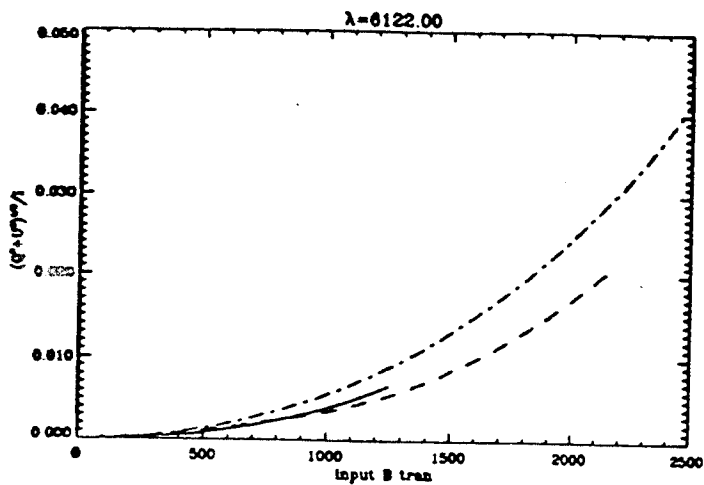
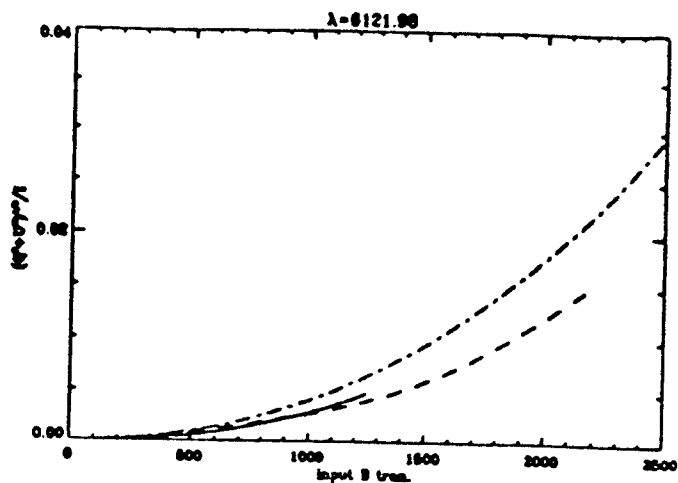
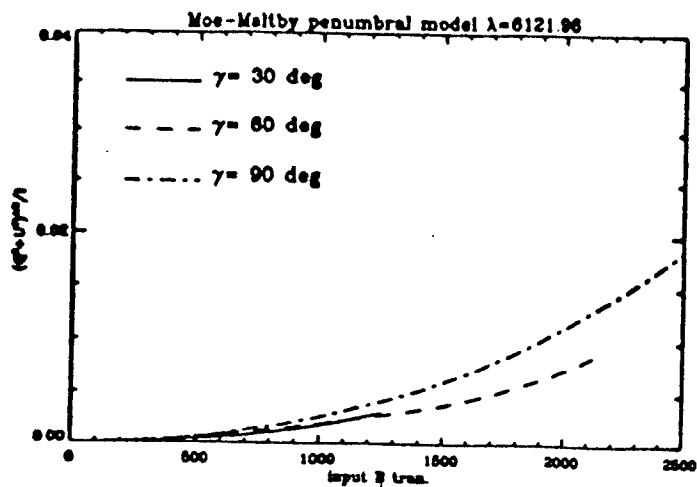


Fig 8





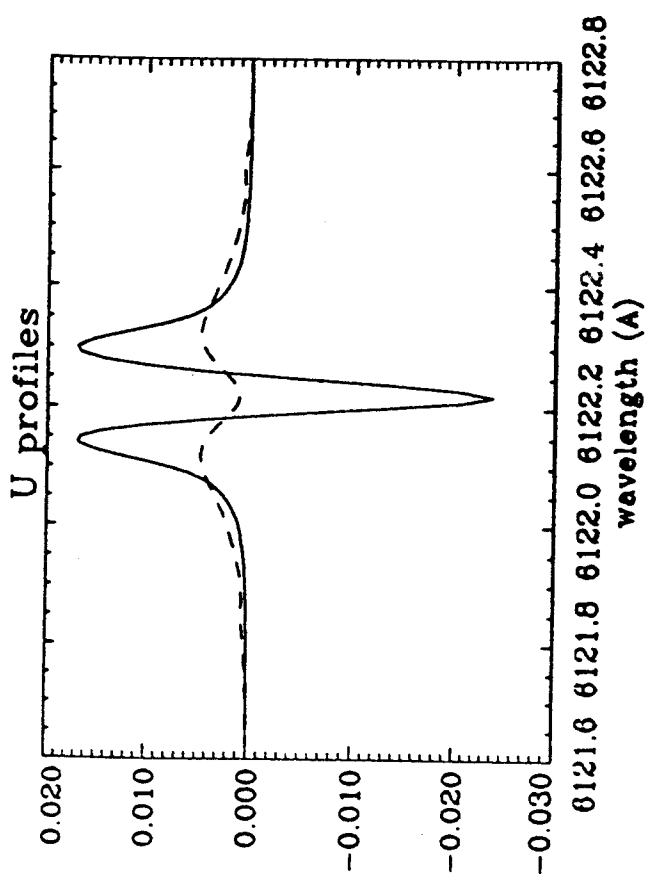
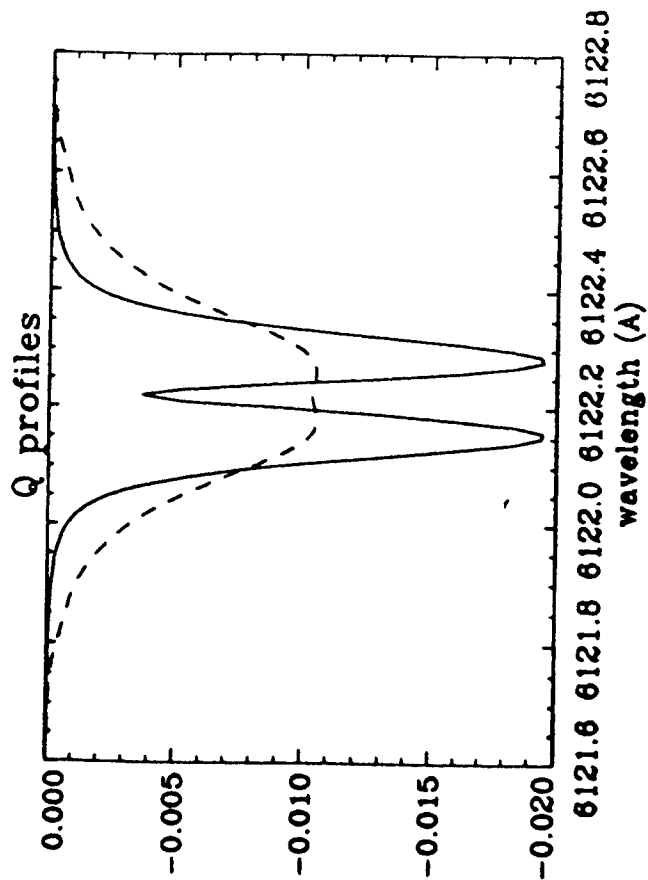
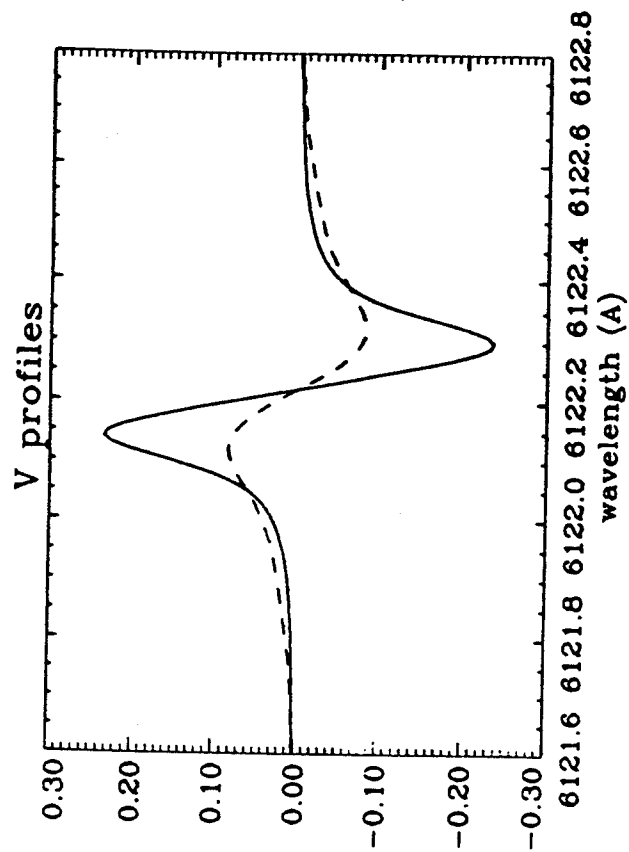
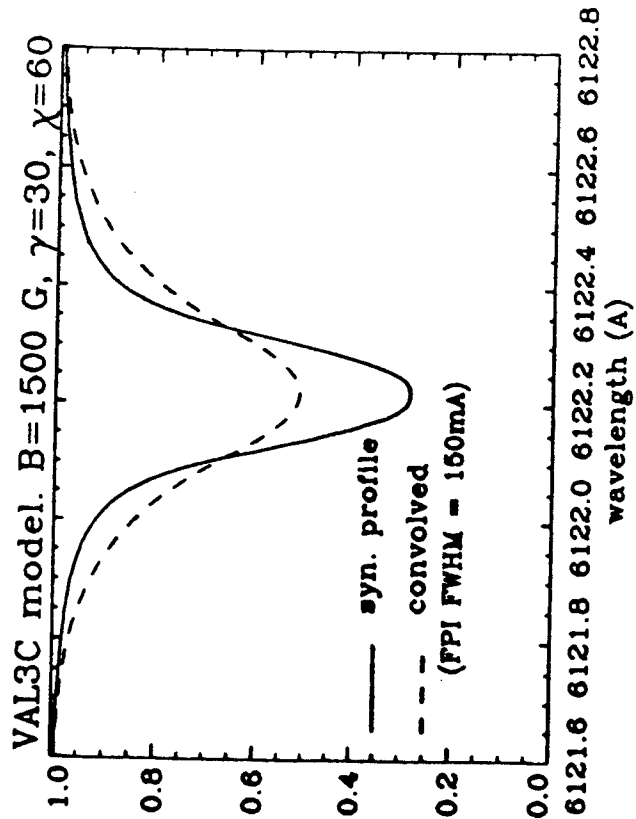


Fig. 11

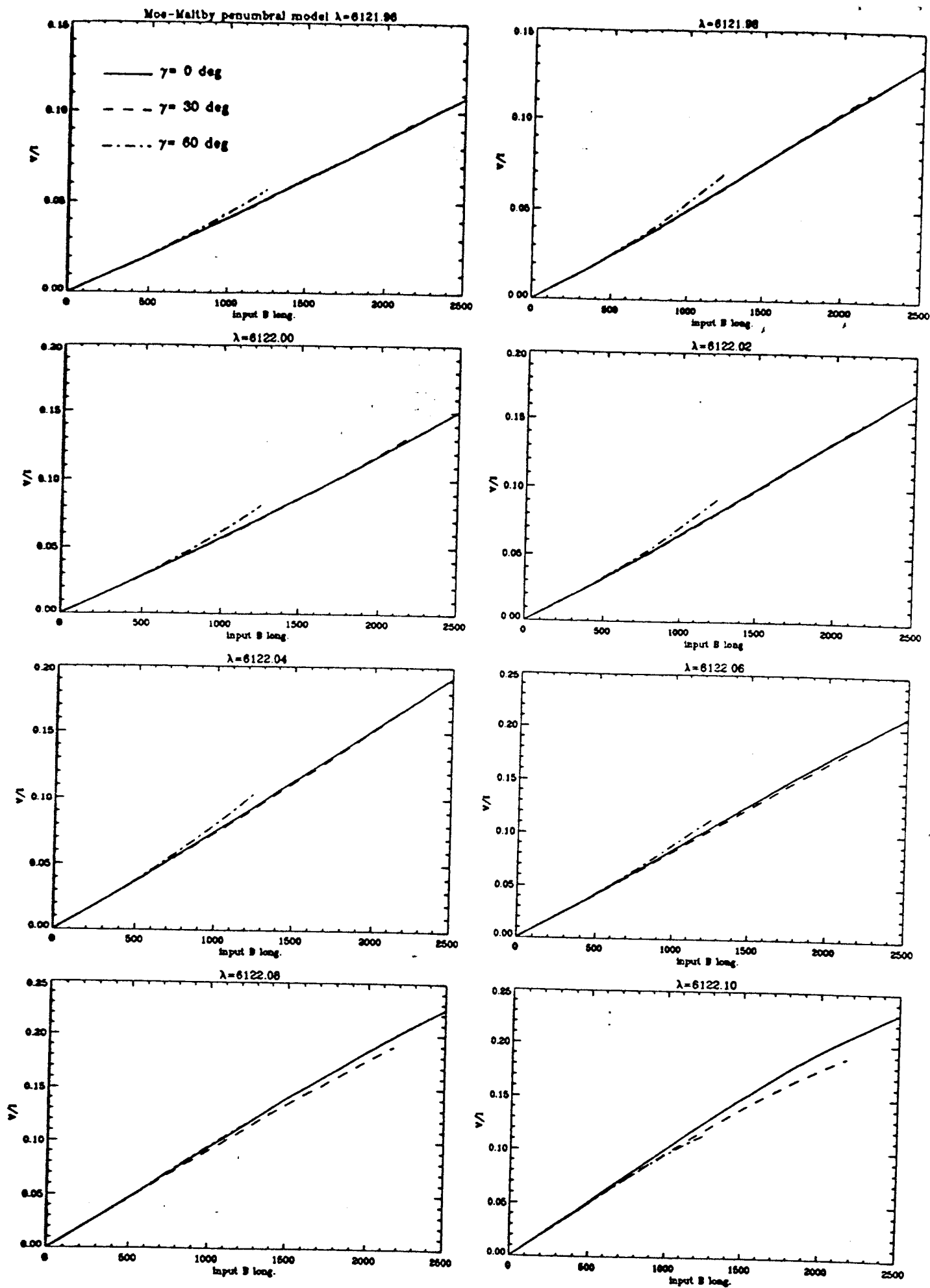


Fig 12.

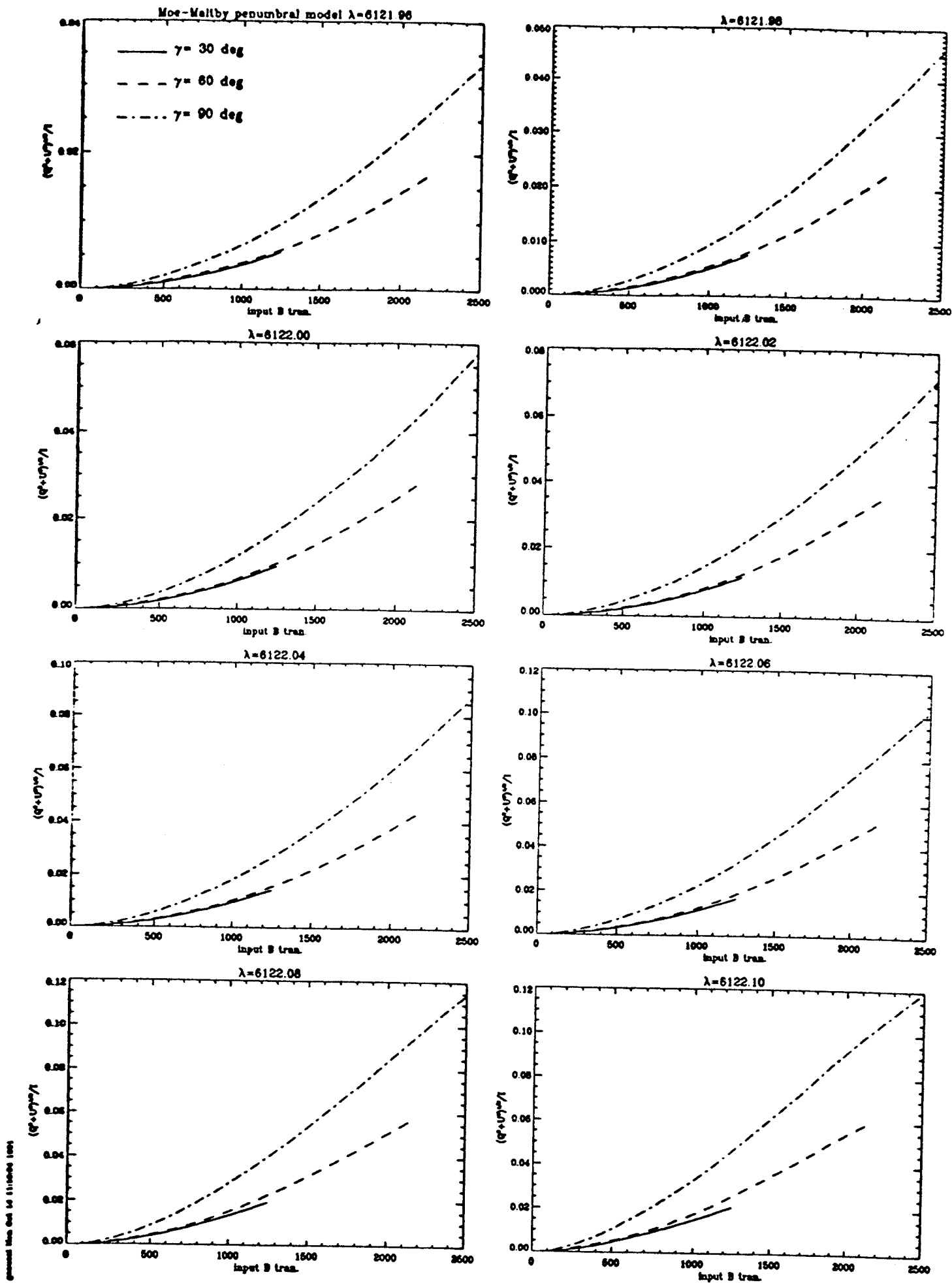


Fig 13

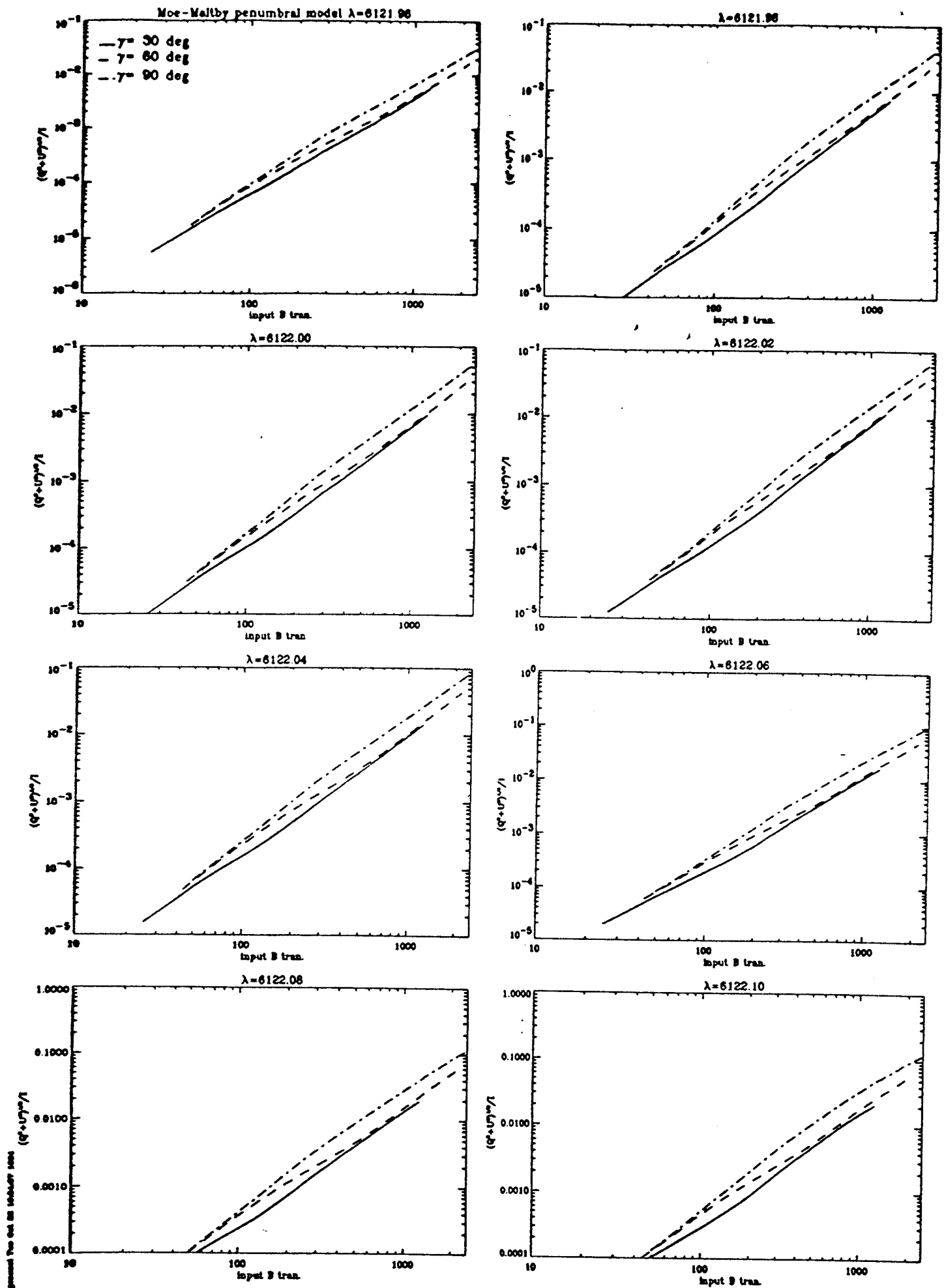


Fig 14.

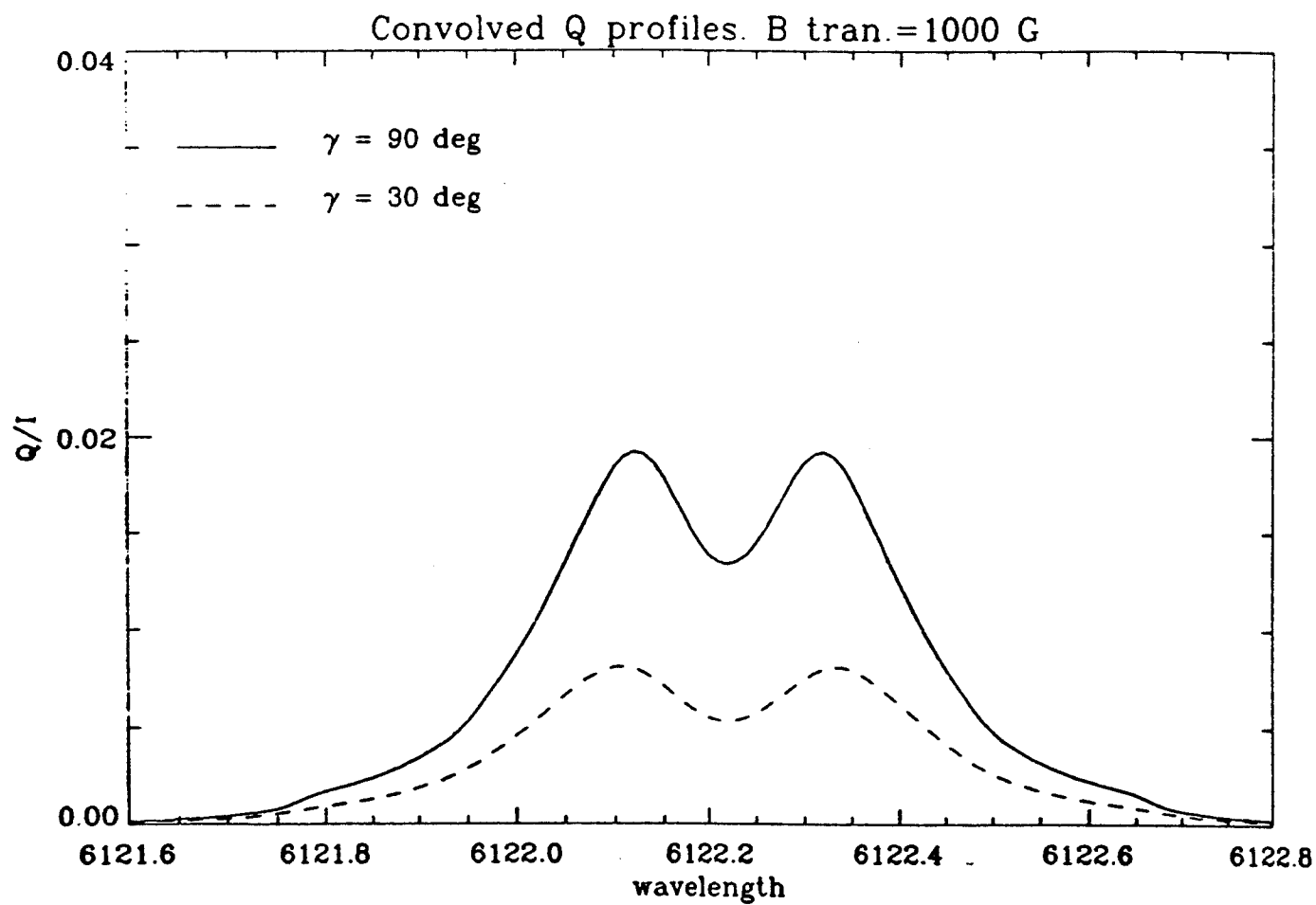
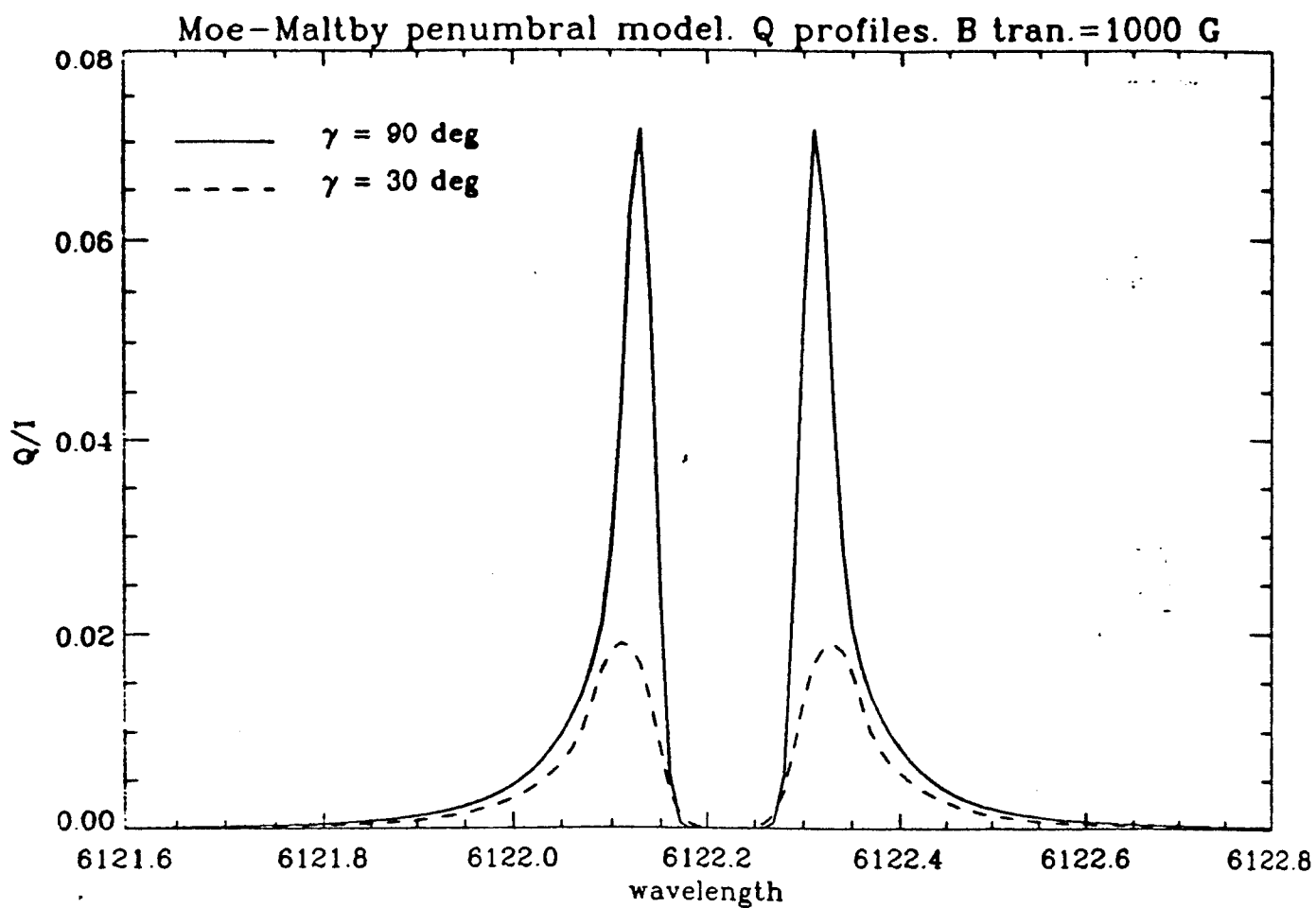


Fig 15

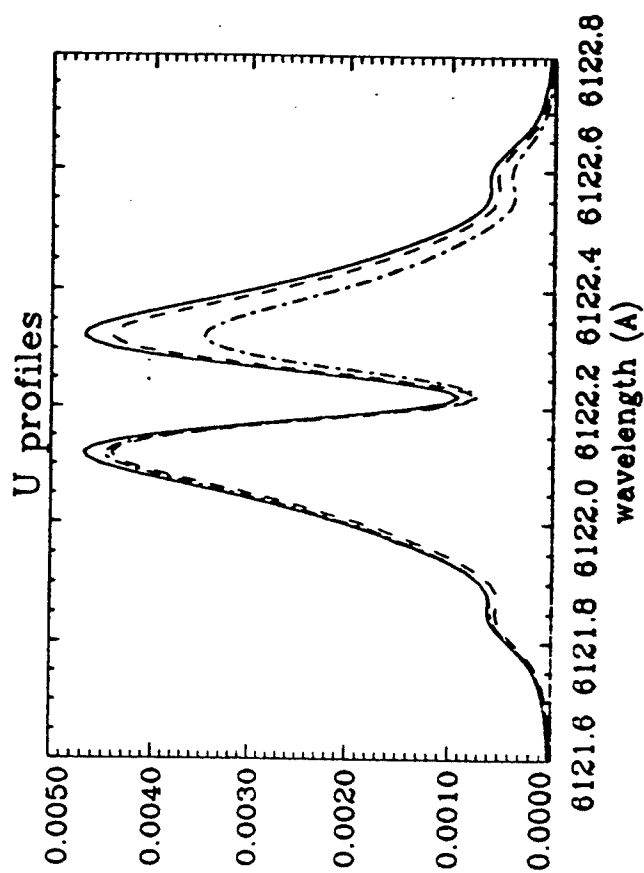
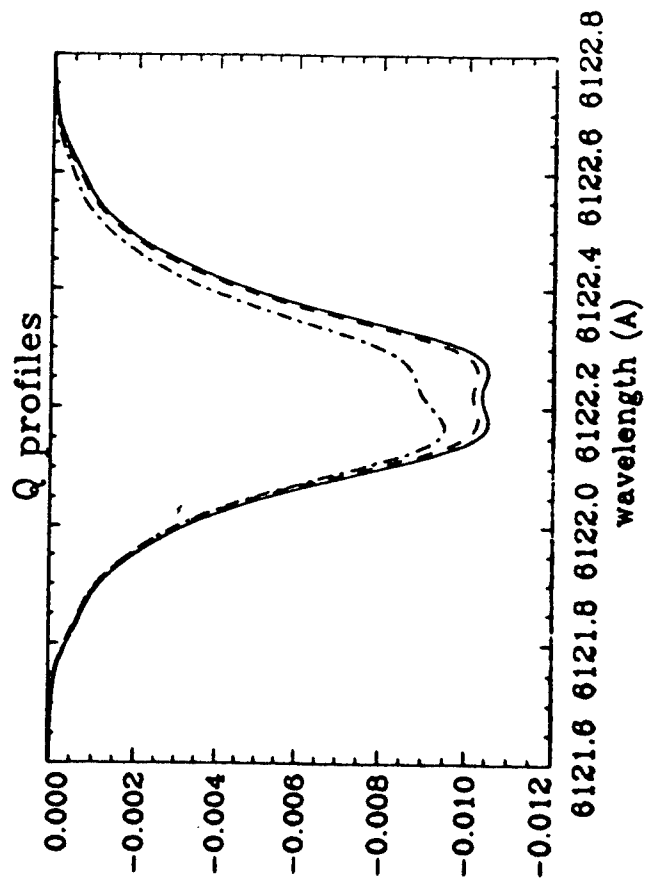
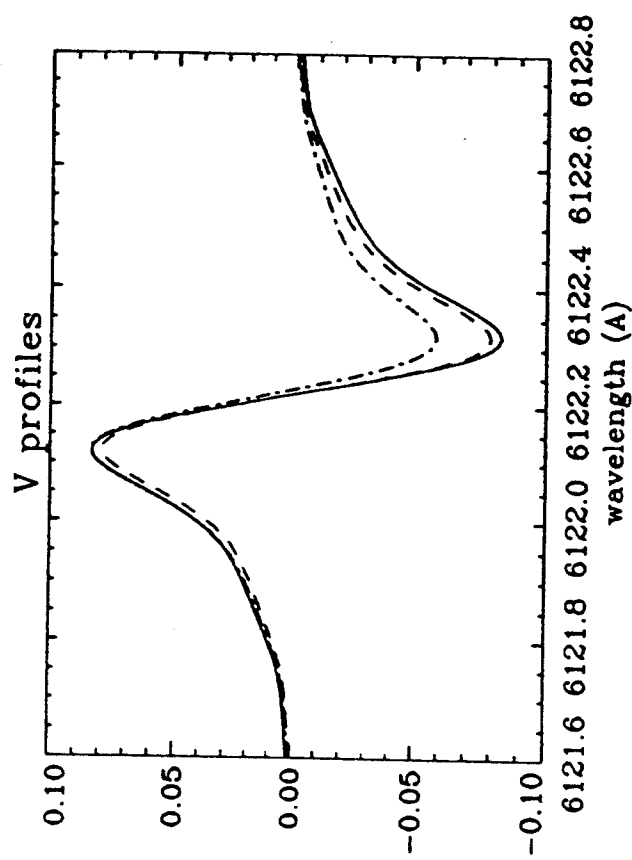
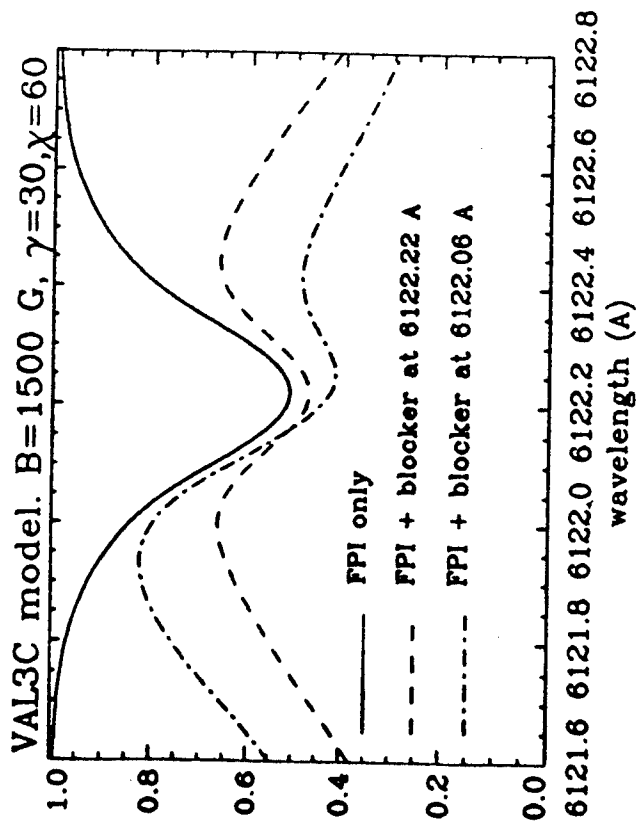
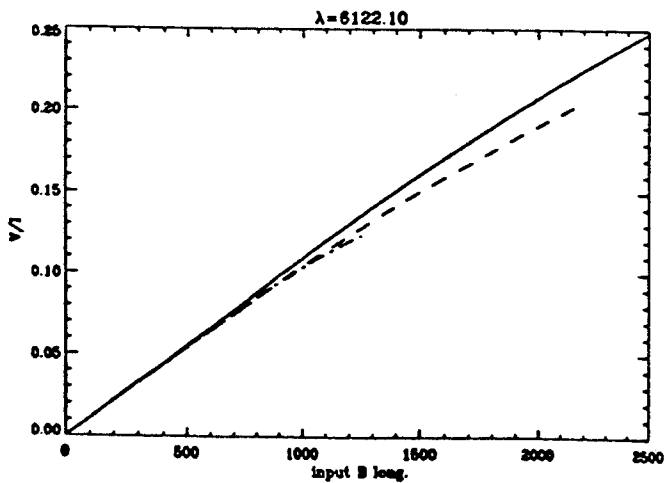
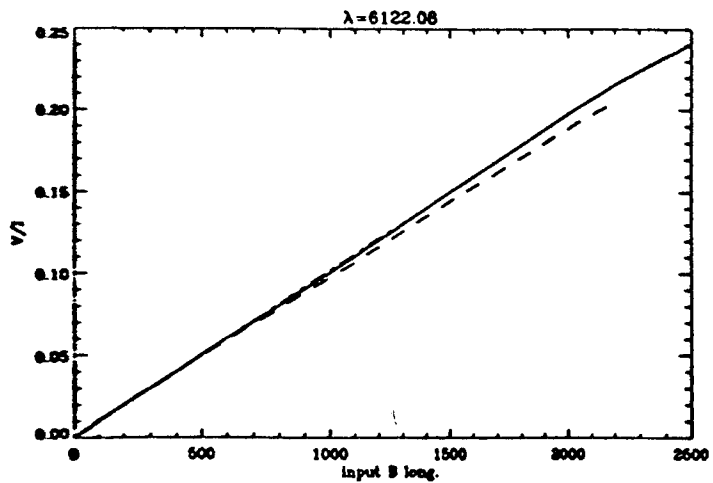
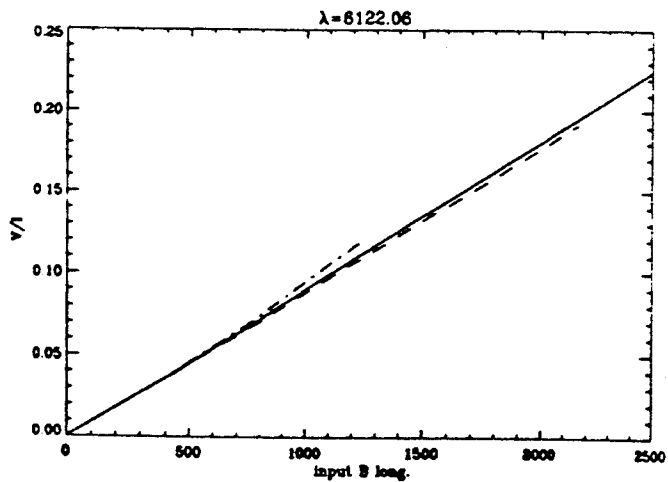
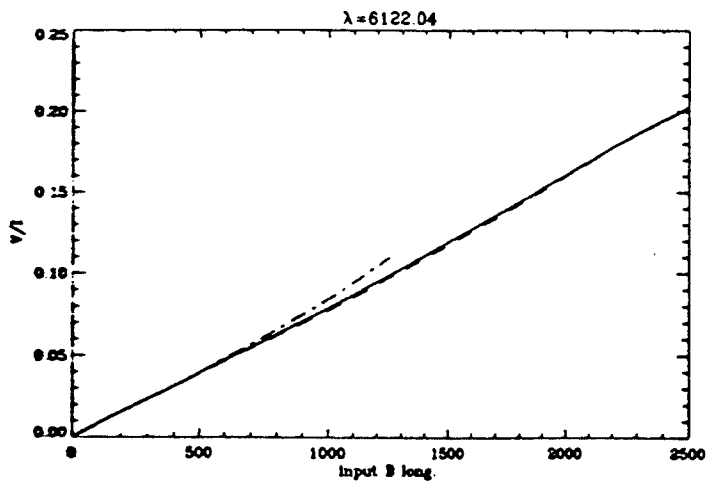
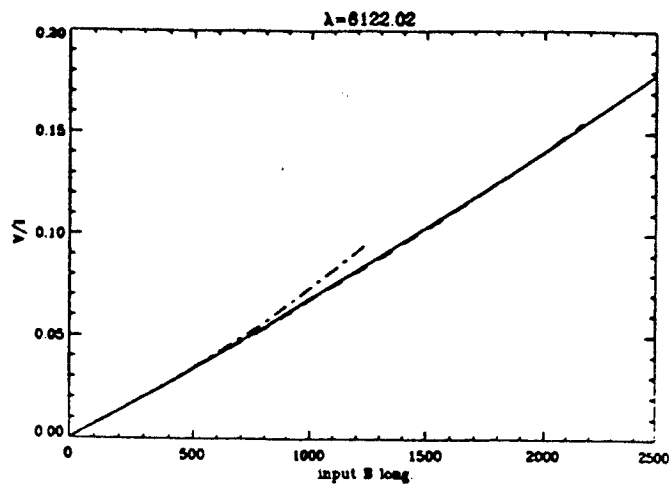
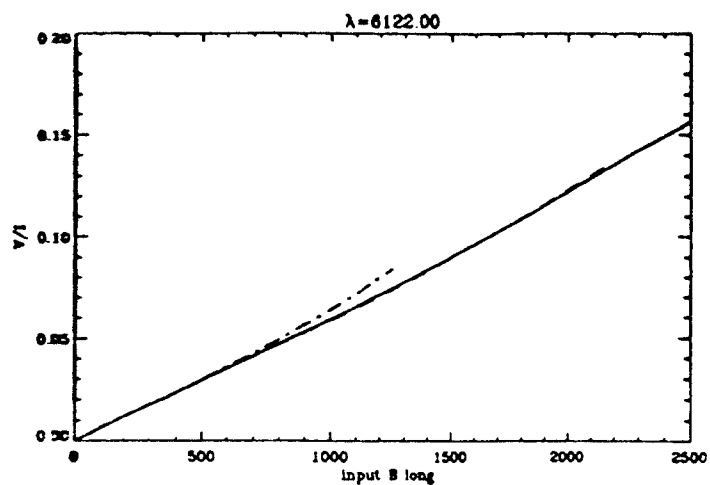
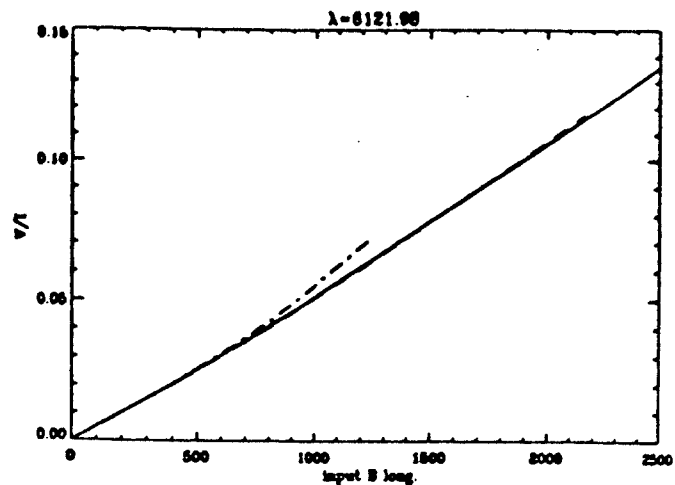
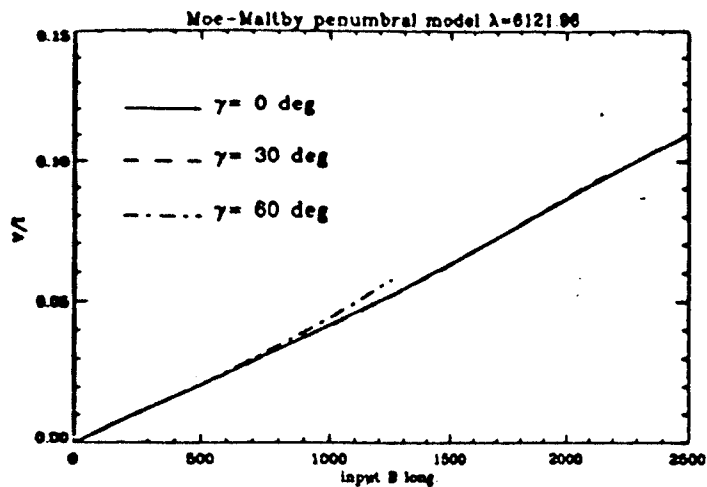


Fig 46



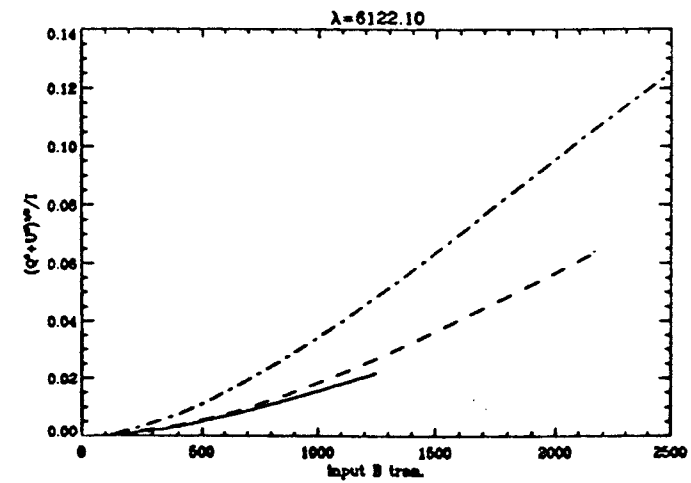
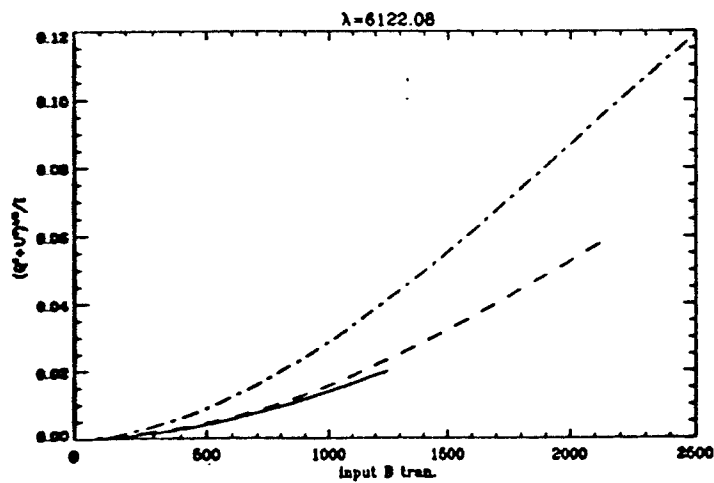
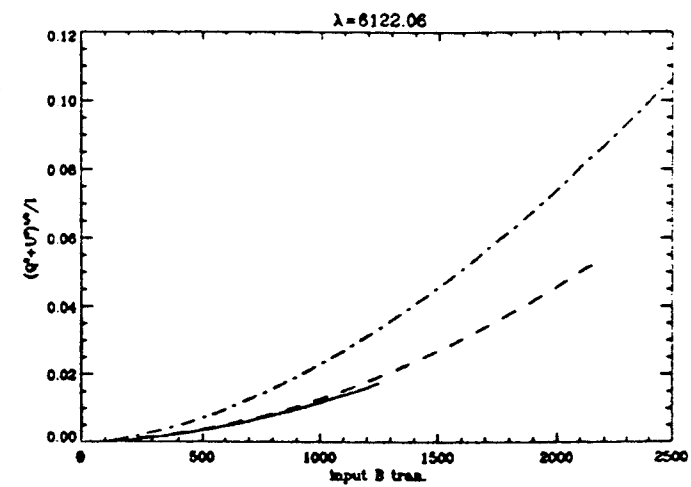
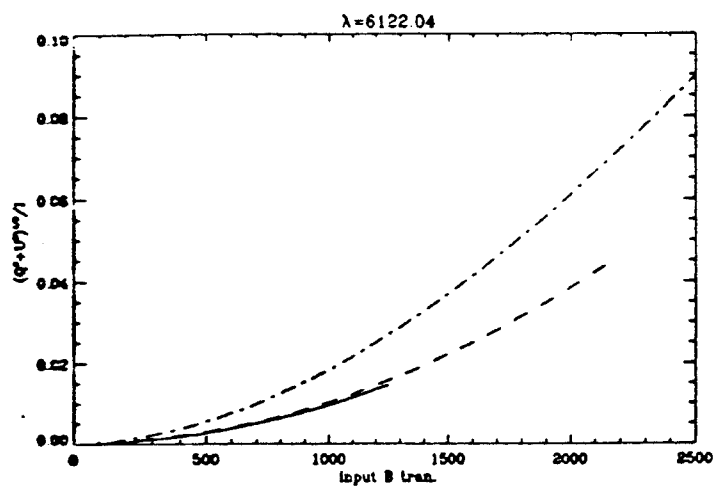
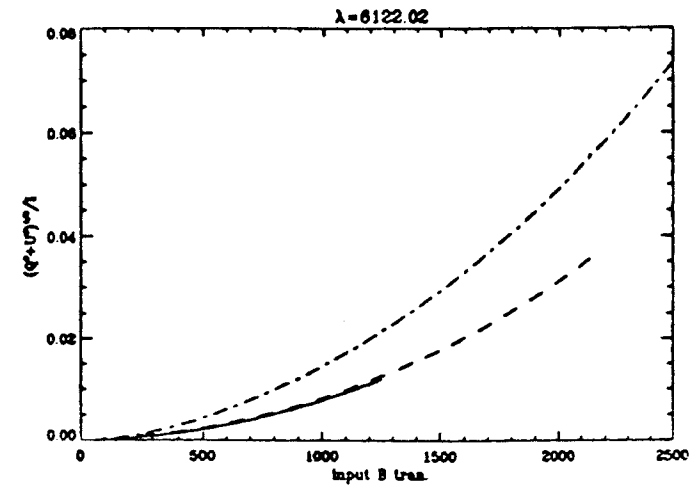
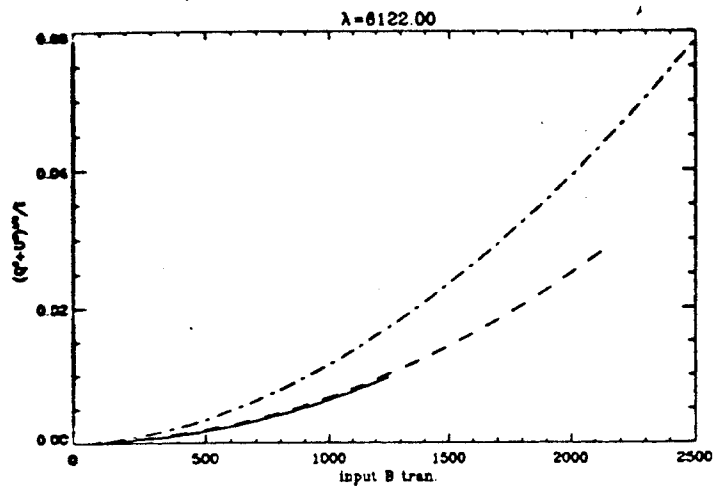
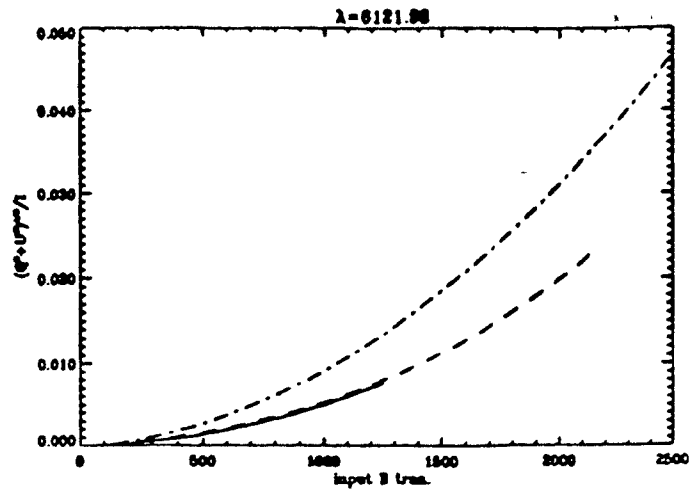
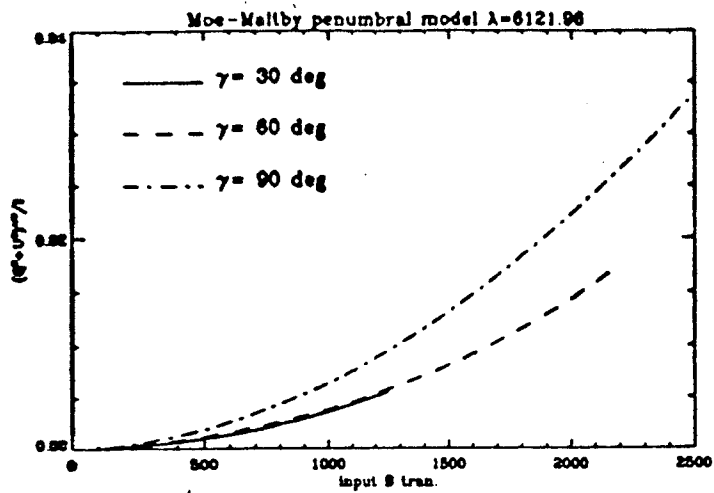


Fig 18

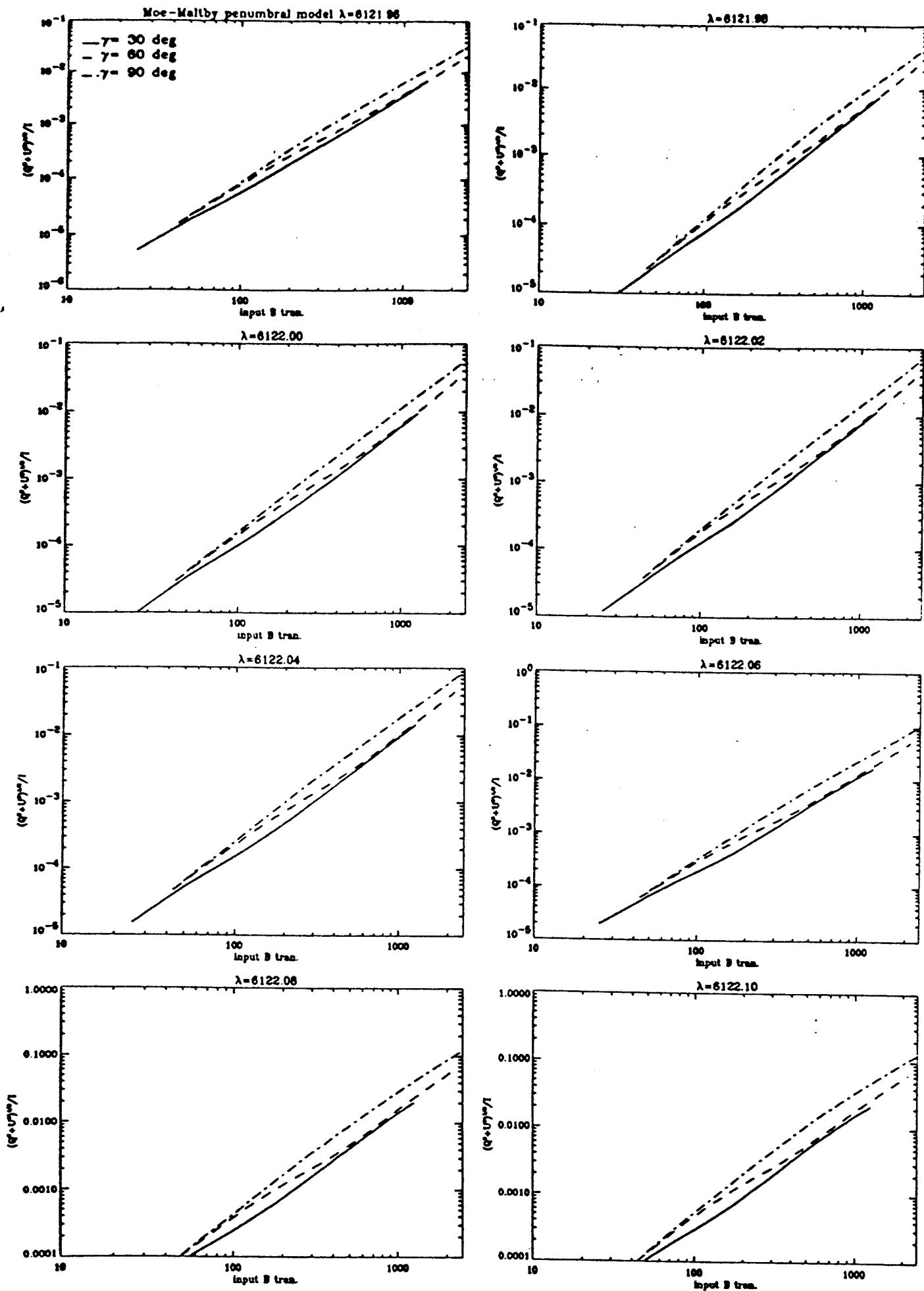


Fig 19

Table 1.  $c_1$  values for 3 models, 3 inclinations and 4 wavelengths

$\lambda\lambda(\text{Angstroms})$	<i>Photosphere</i> $\gamma = 0, 30, 60^\circ$	<i>Penumbra</i> $\gamma = 0, 30, 60^\circ$	<i>Umbra</i> $\gamma = 0, 30, 60^\circ$
6122.00	24520, 24315, 23294	16390, 16540, 15688	12720, 12670, 12240
6122.02	20197, 19996, 19068	14255, 14410, 13600	11840, 11780, 11320
6122.04	16650, 16450, 15615	12490, 12668, 11900	10950, 10880, 10380
6122.06	13840, 13660, 12920	11110, 11335, 10630	10080, 10000, 9470

Table 2.  $c_2$  values for 3 models, 3 inclinations and 4 wavelengths

$\lambda\lambda(\text{Angstroms})$	<i>Photosphere</i> $\gamma = 30, 60, 90^\circ$	<i>Penumbra</i> $\gamma = 30, 60, 90^\circ$	<i>Umbra</i> $\gamma = 30, 60, 90^\circ$
6122.00	12880, 12780, 12150	12300, 13080, 10530	11860, 12115, 10230
6122.02	11430, 11300, 10700	11660, 11690, 9420	10800, 11040, 9385
6122.04	10160, 10035, 9490	10530, 10540, 8500	9800, 10020, 8580
6122.06	9080, 9000, 8510	9610, 9650, 7790	8870, 9081, 7846

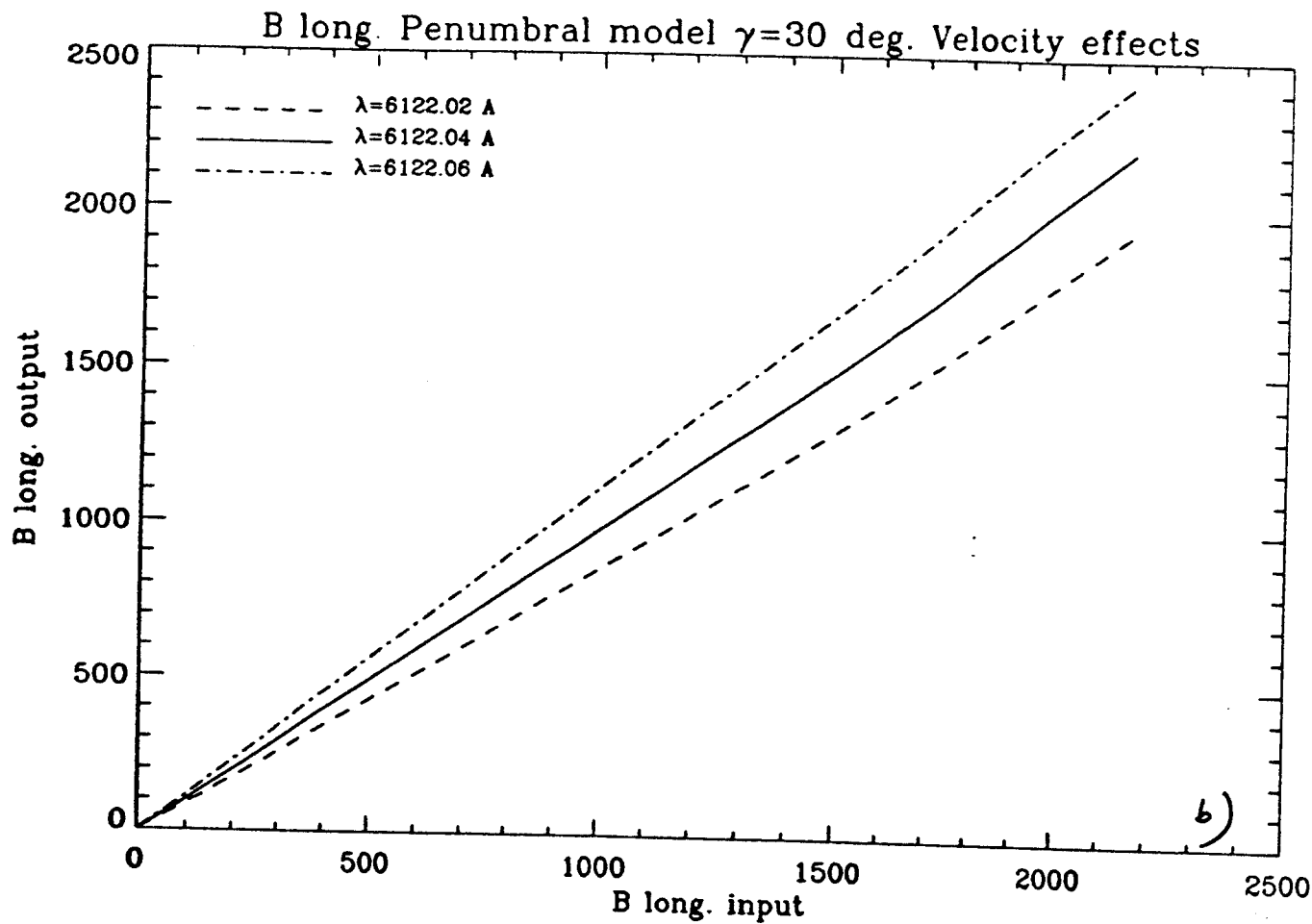
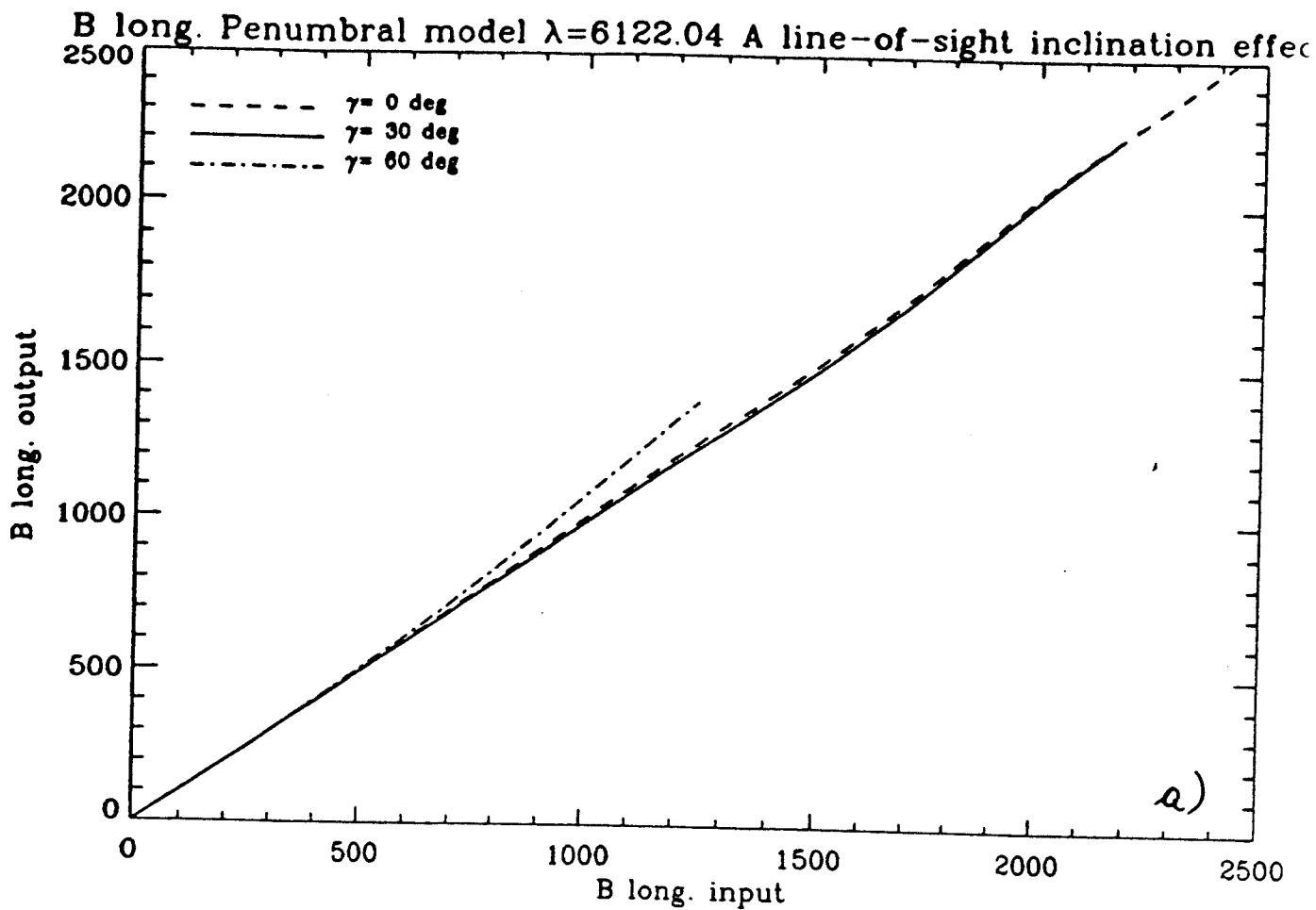
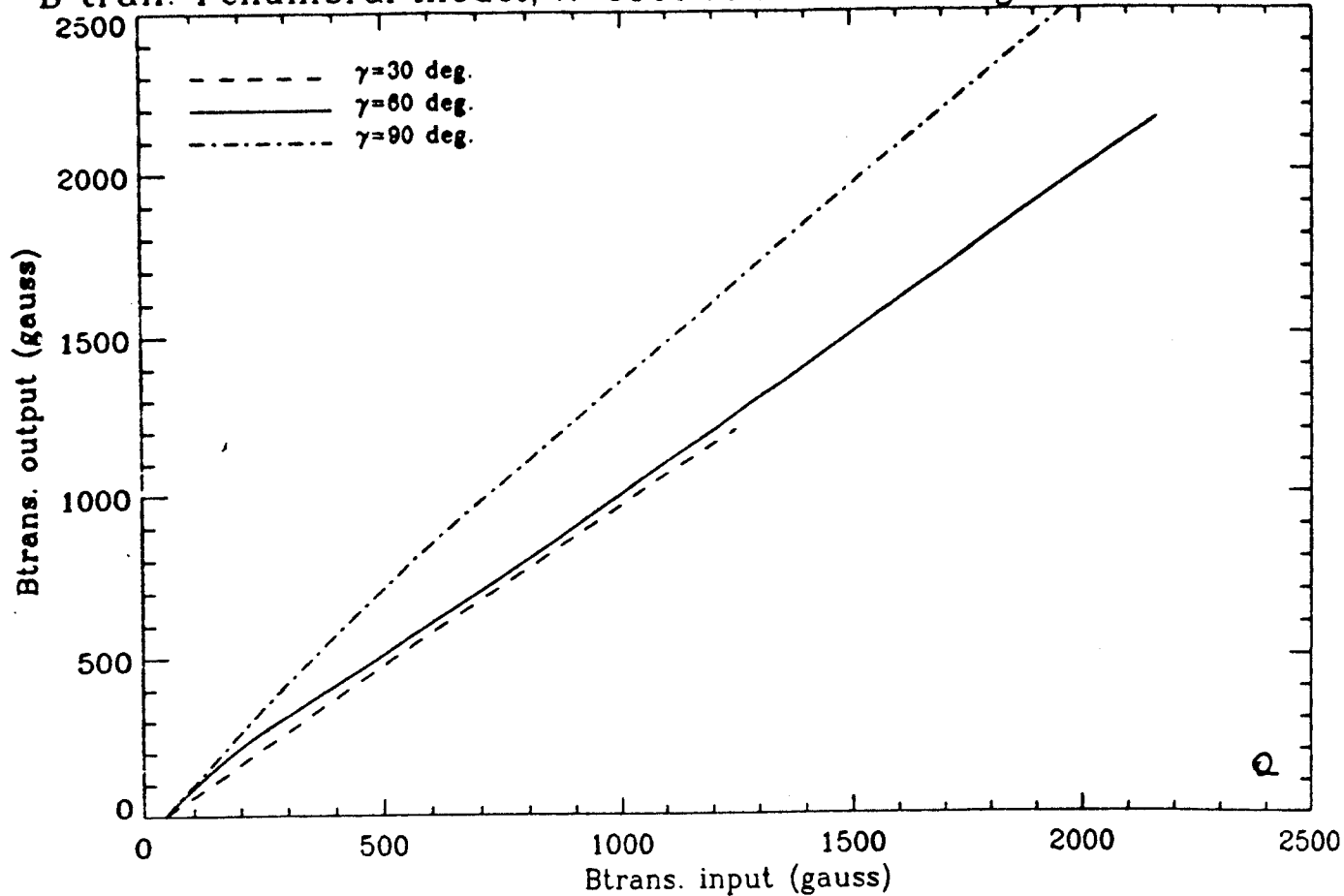


Fig. 20

B tran. Penumbral model,  $\lambda=6122.04$  A. Line-of-sight inclination effects



B tran. Penumbral model,  $\gamma=60$  deg. Velocity effects

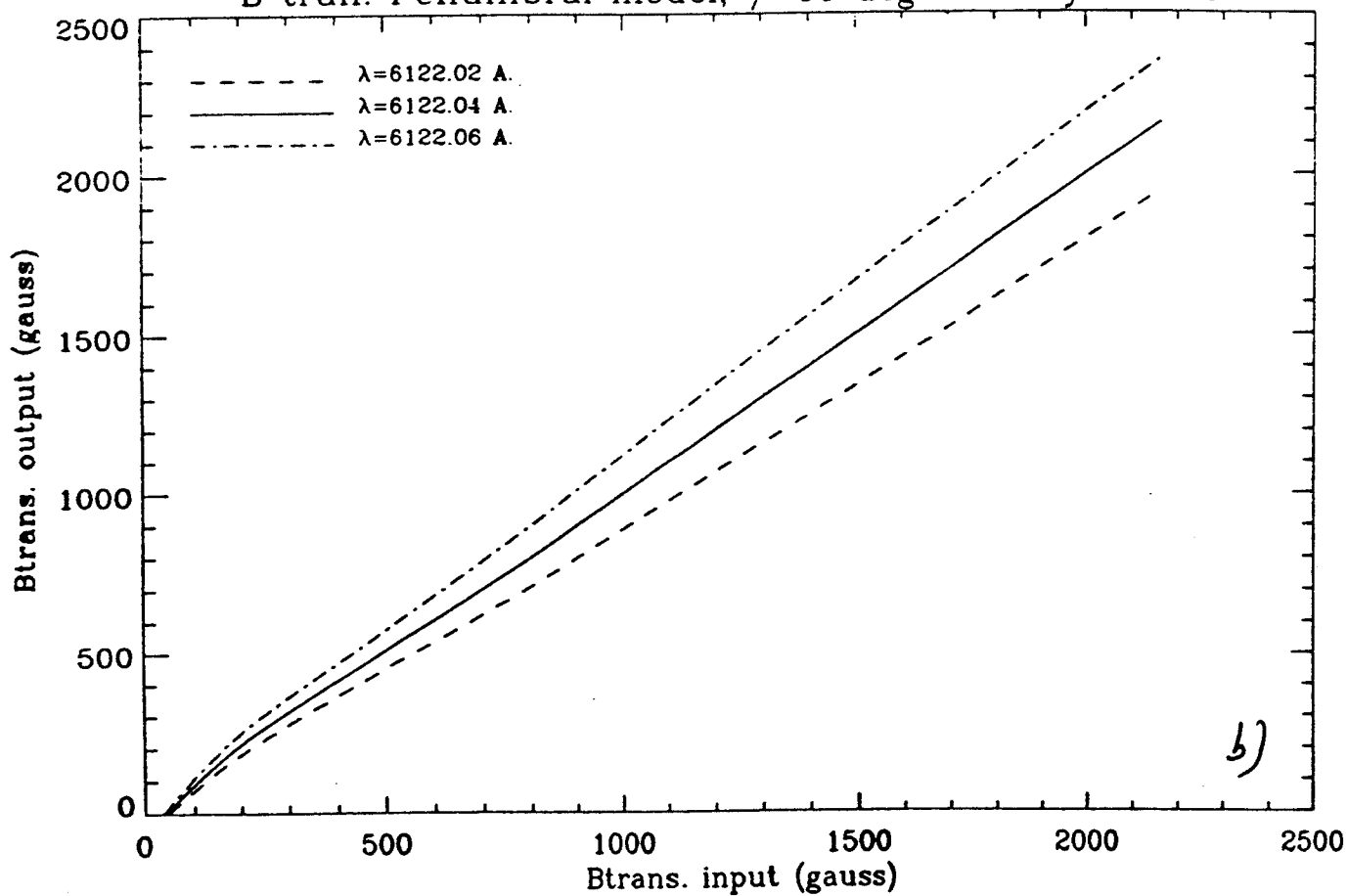


Fig 21

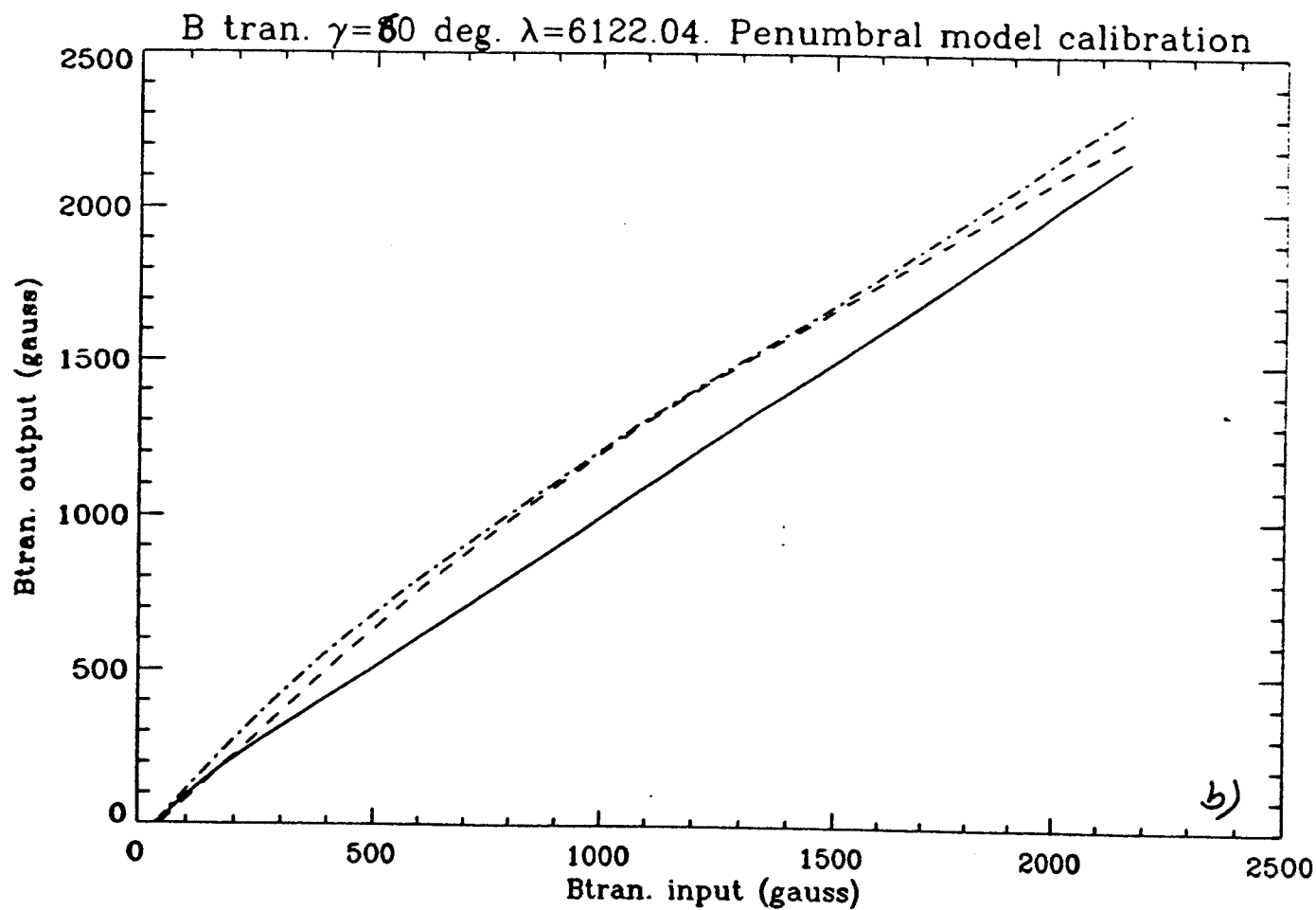
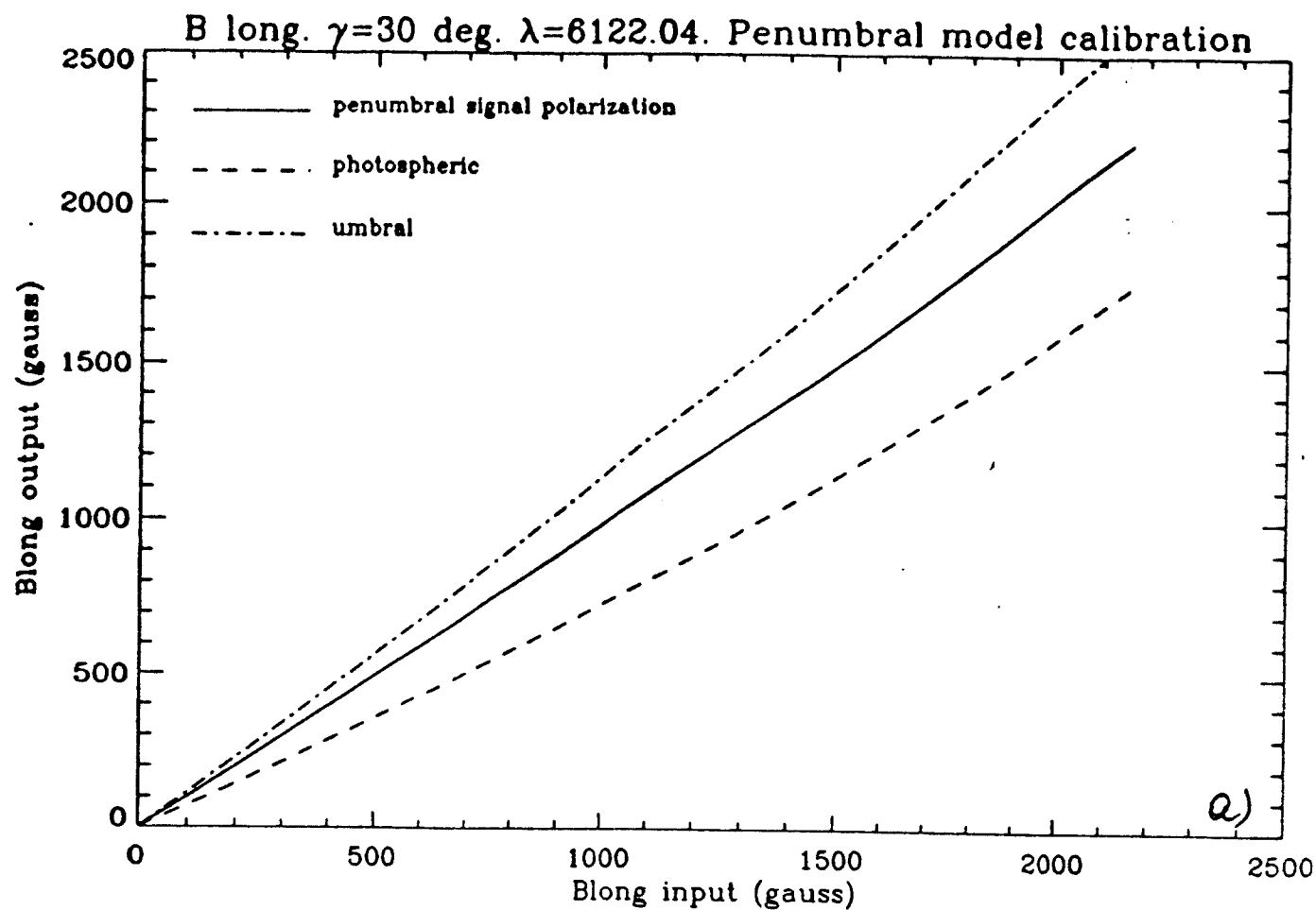
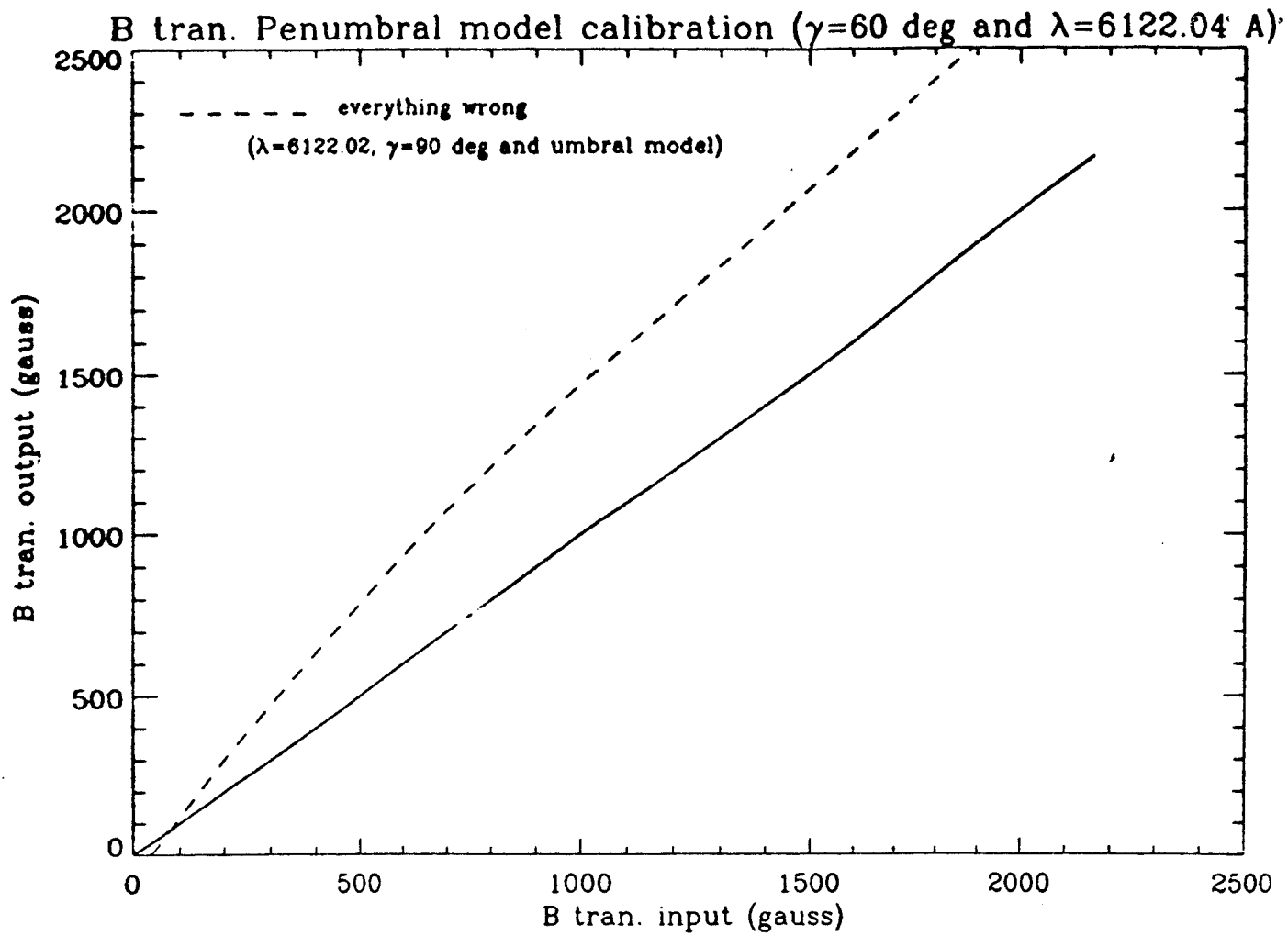
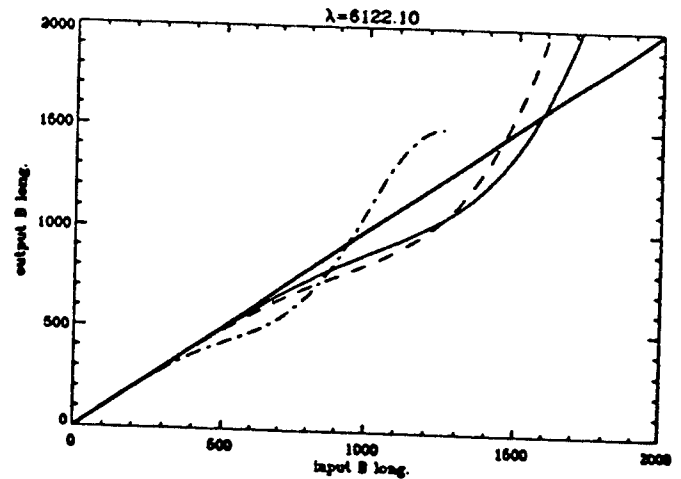
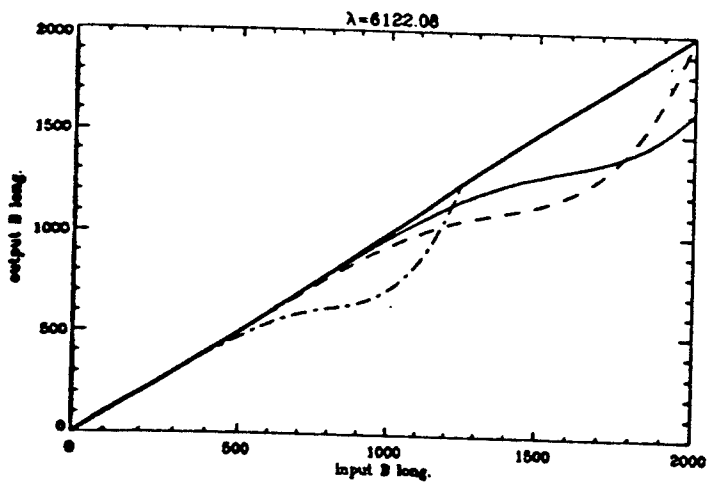
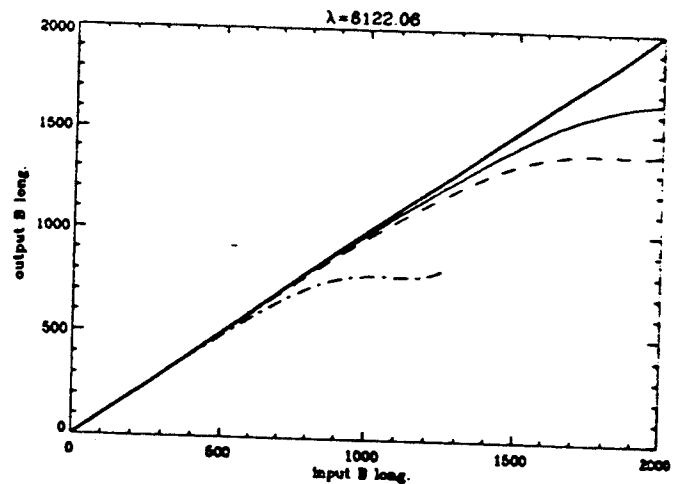
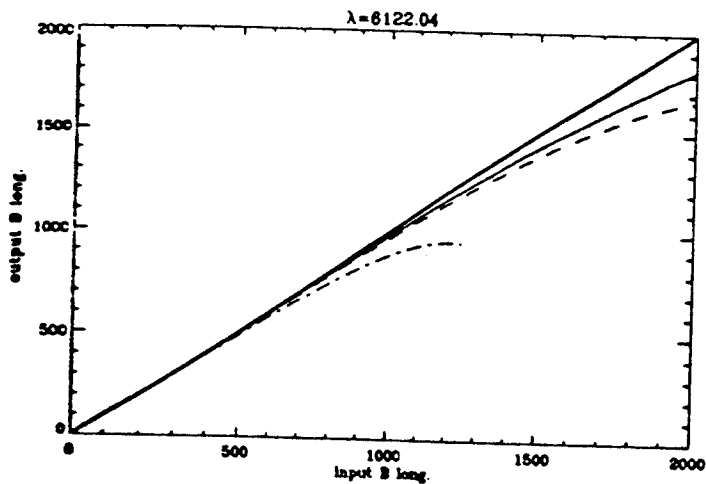
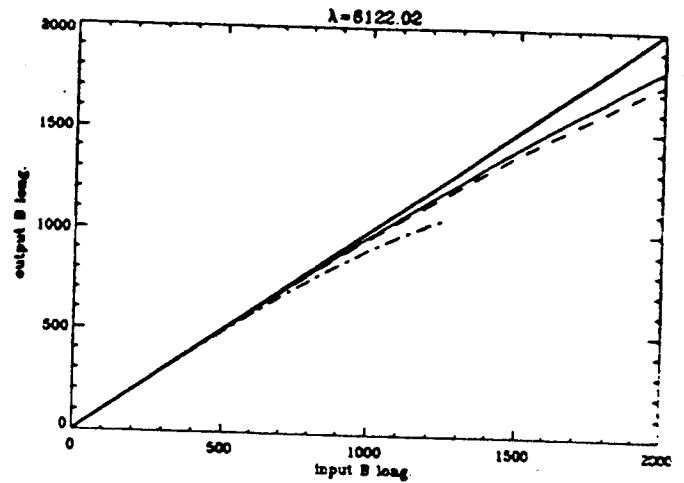
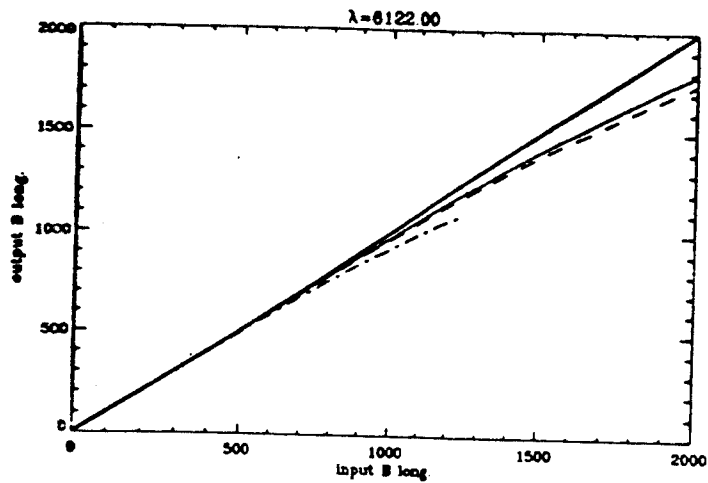
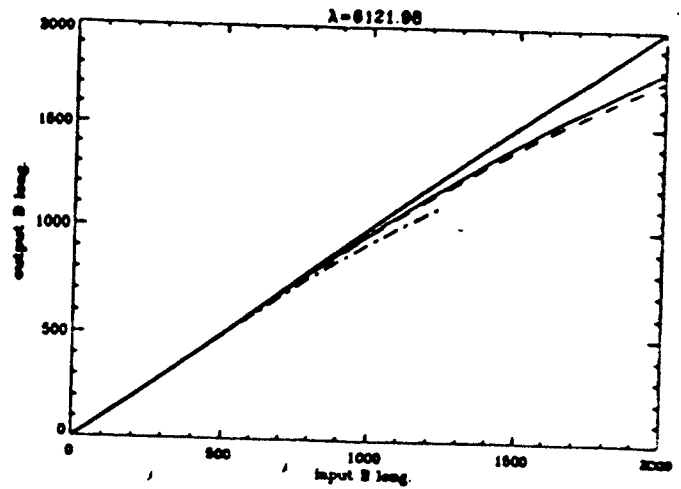
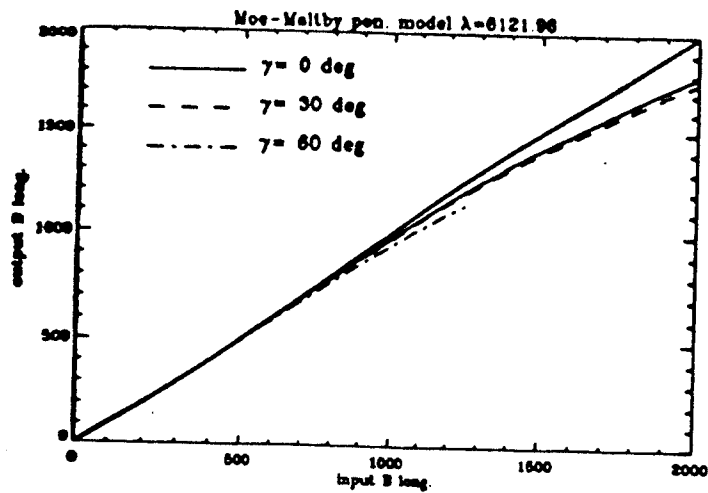


Fig 22





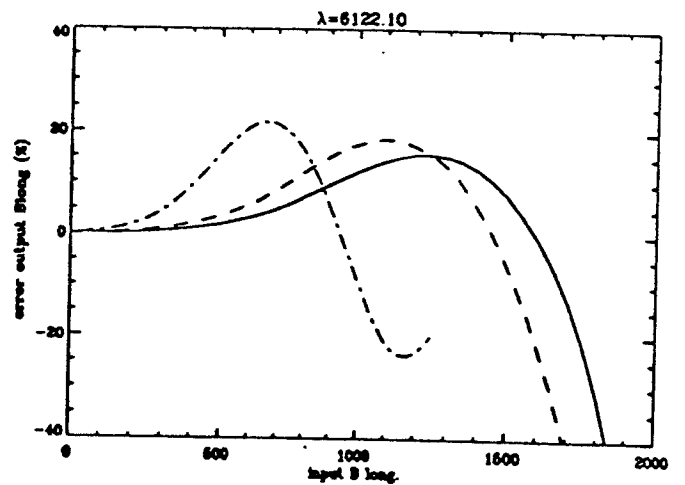
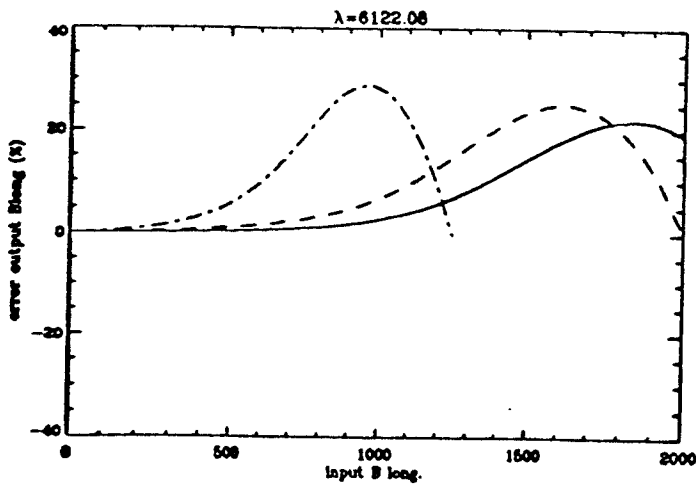
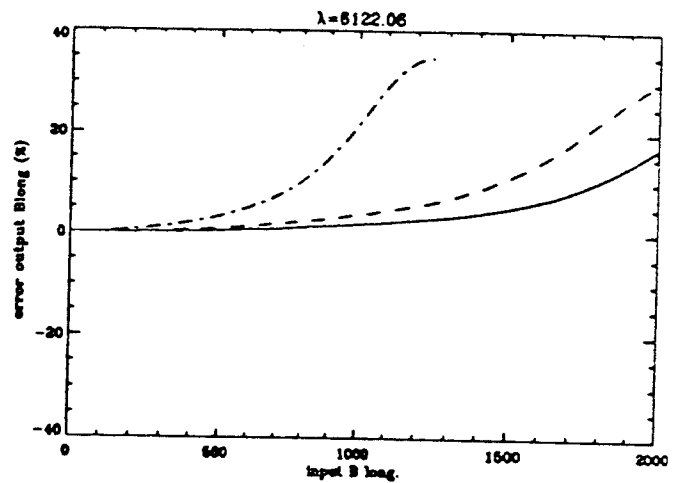
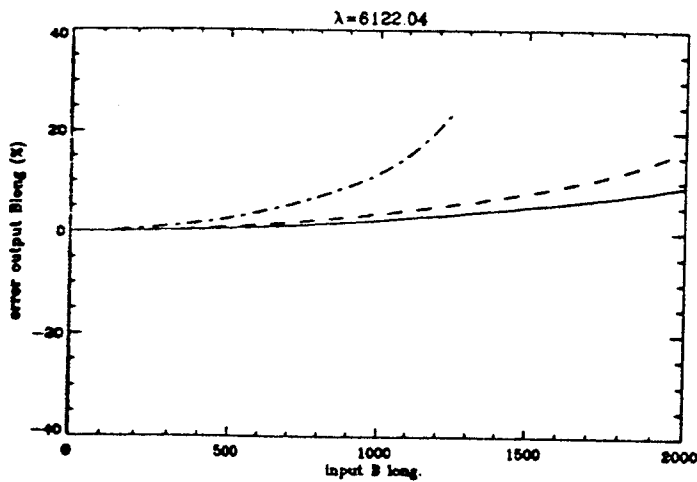
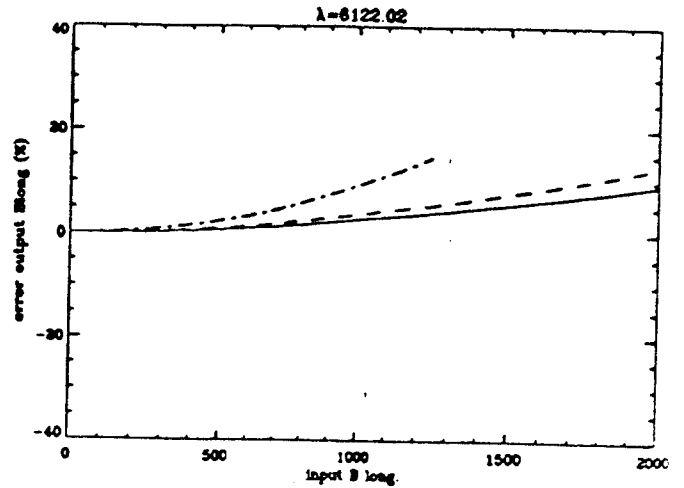
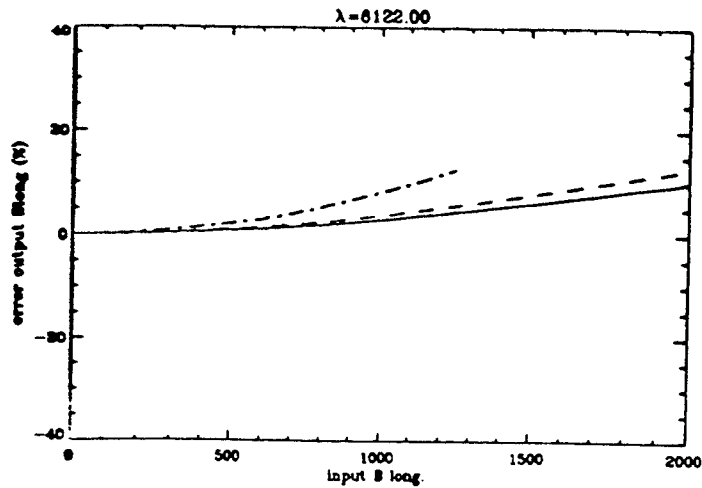
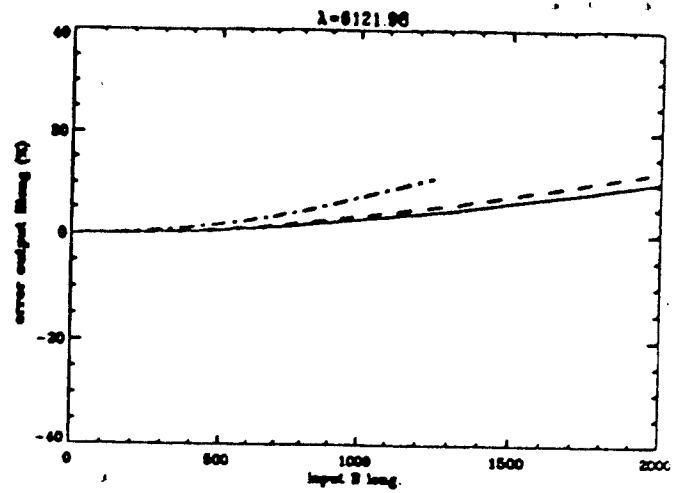
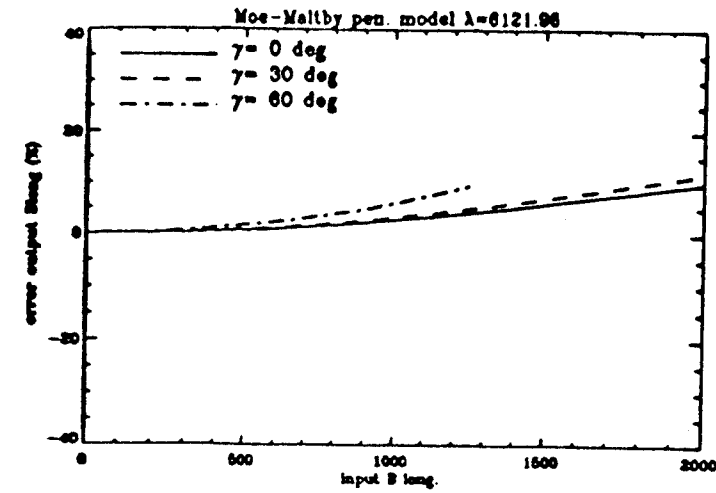
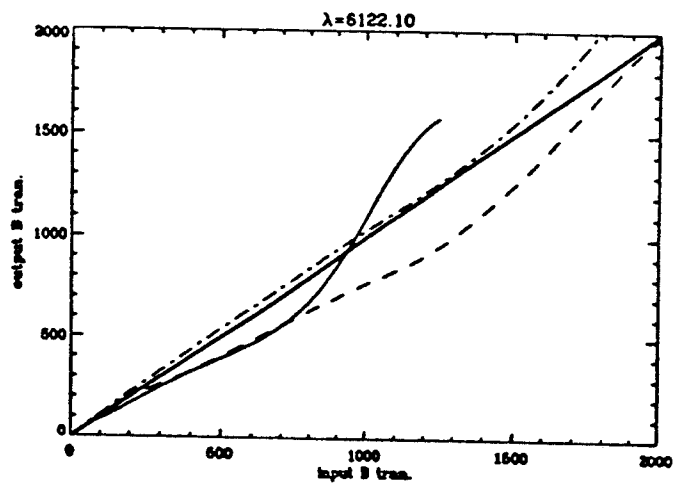
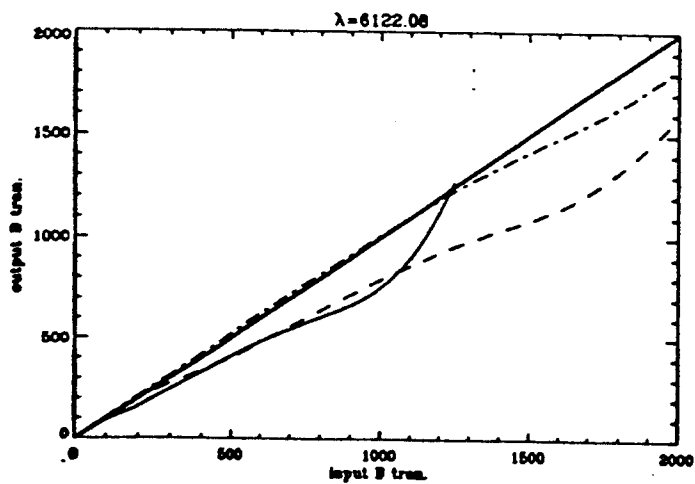
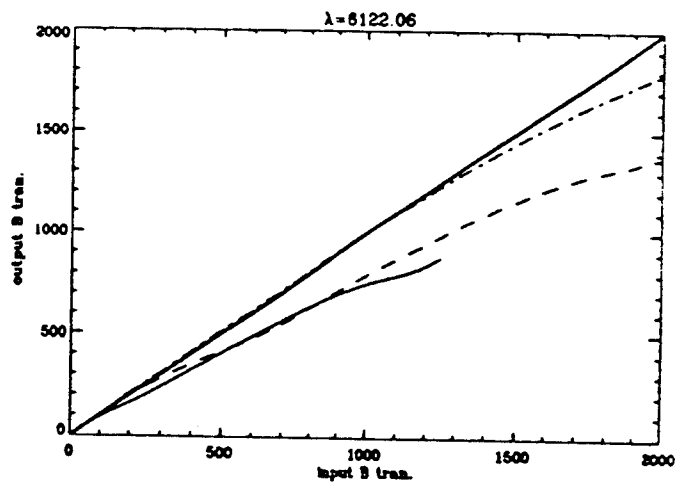
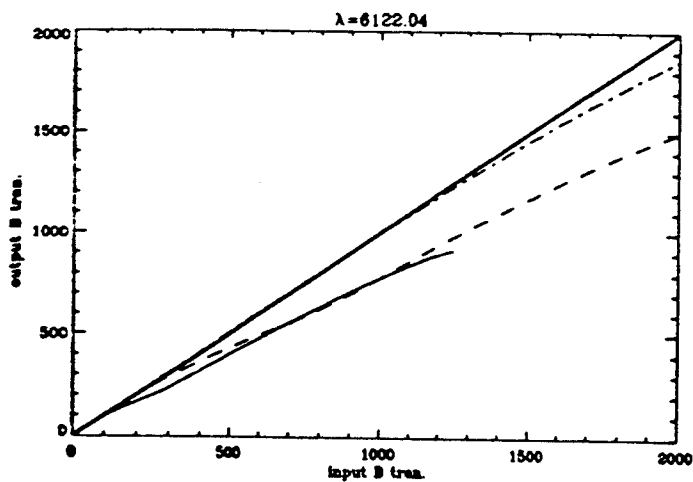
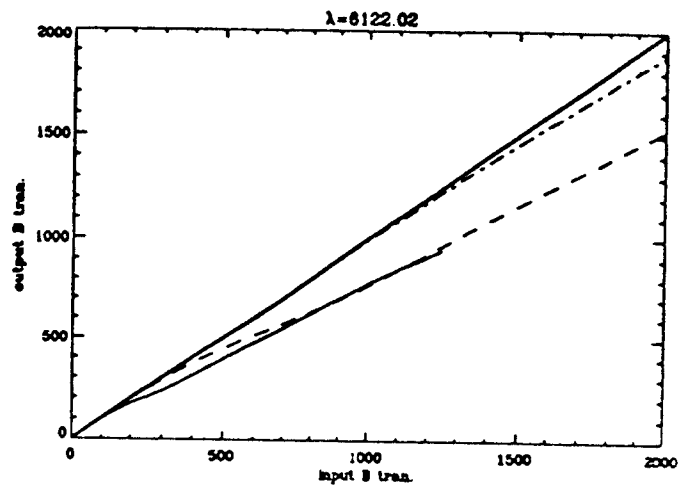
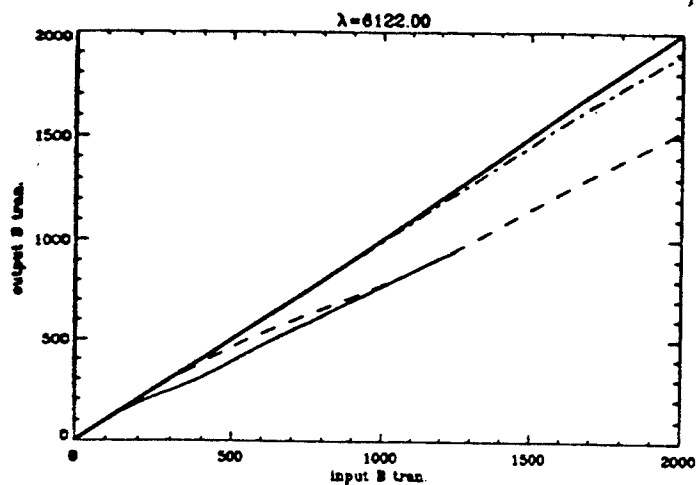
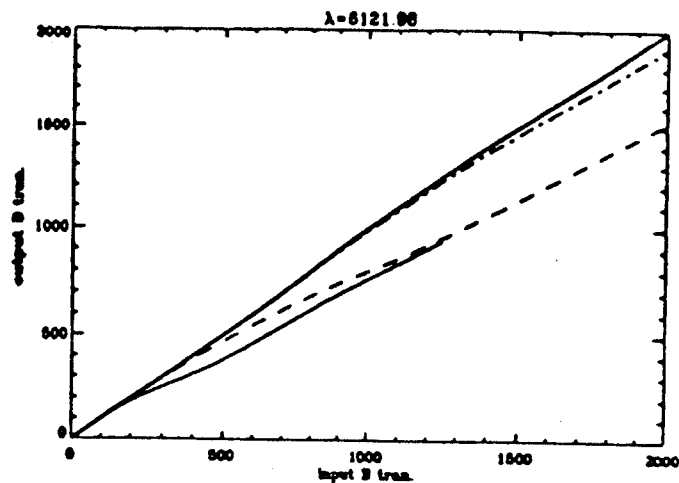
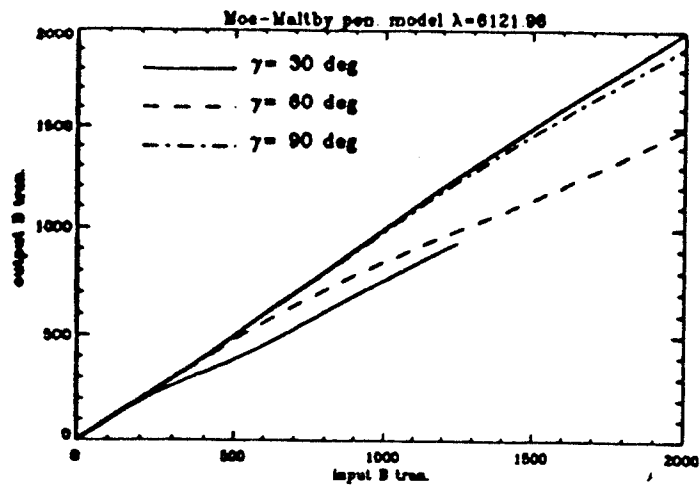


Fig 25



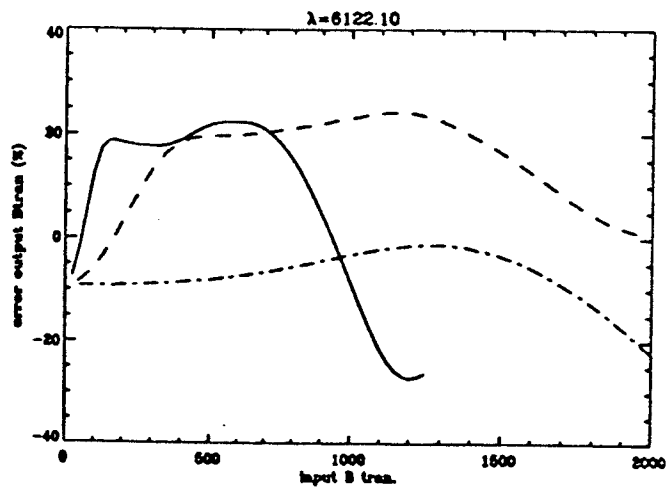
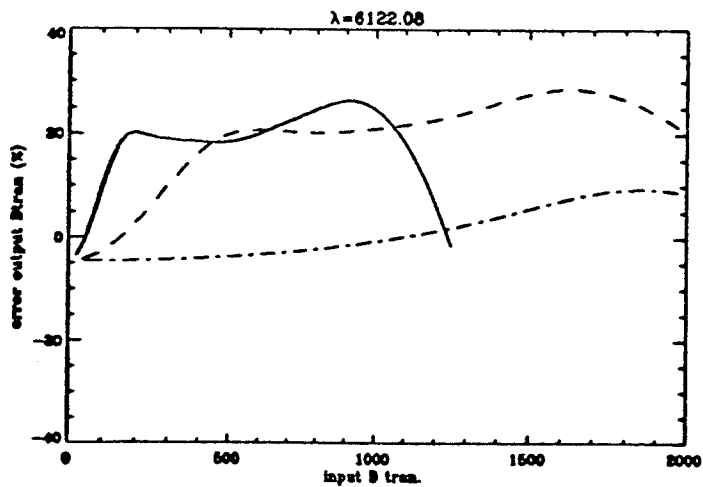
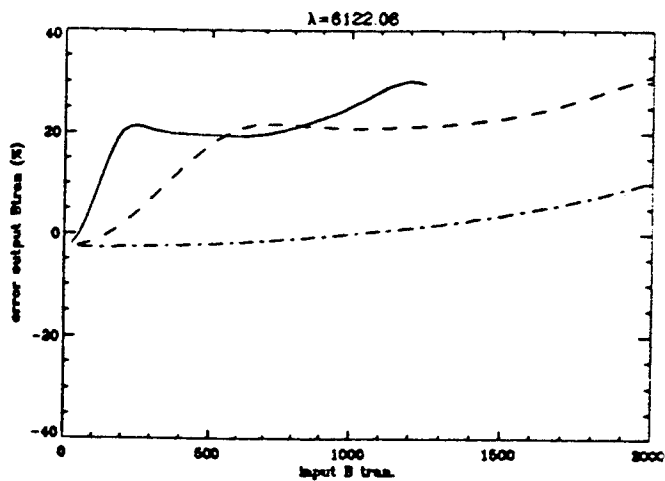
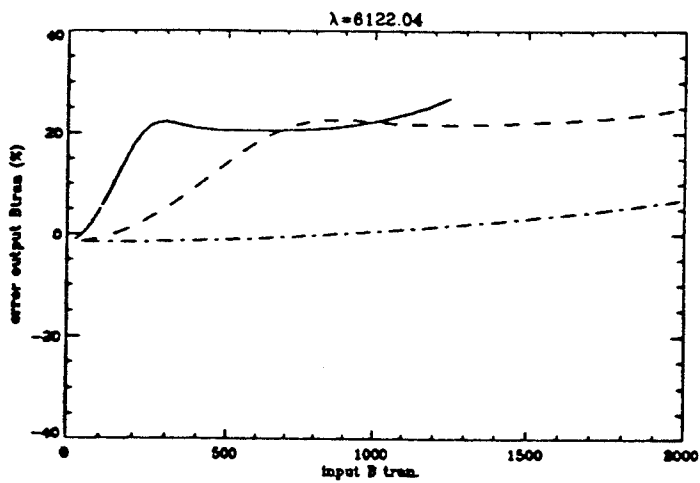
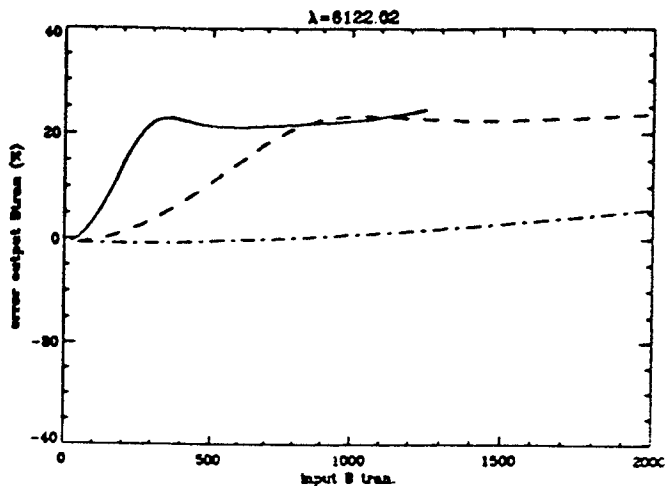
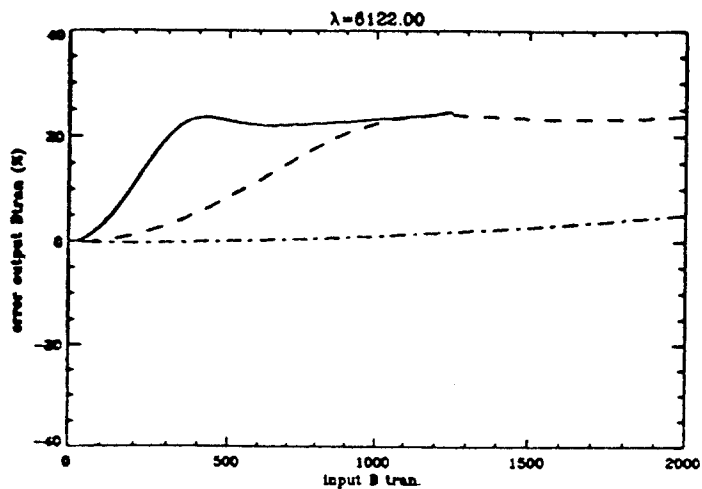
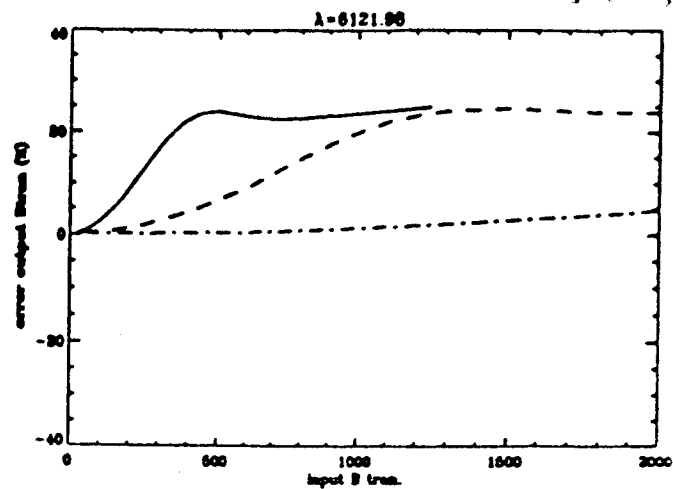
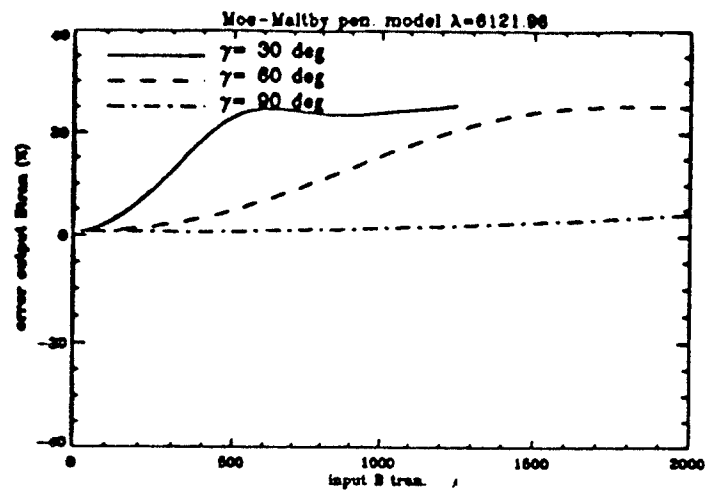


Fig 27

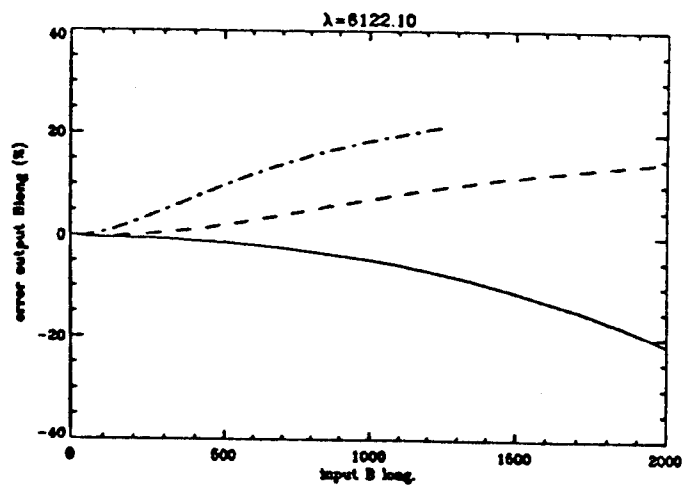
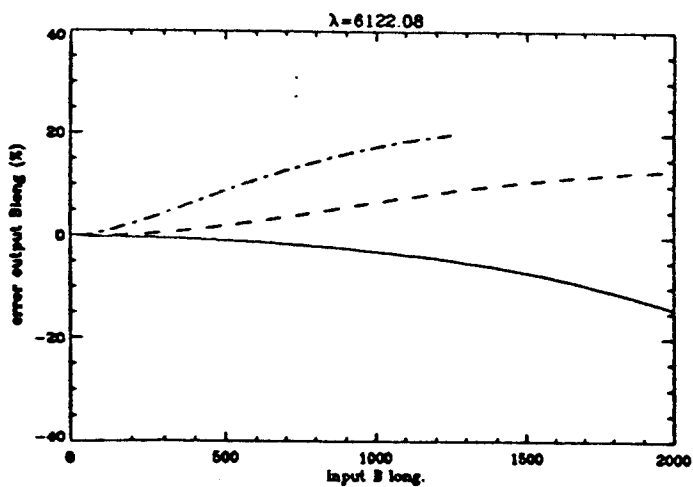
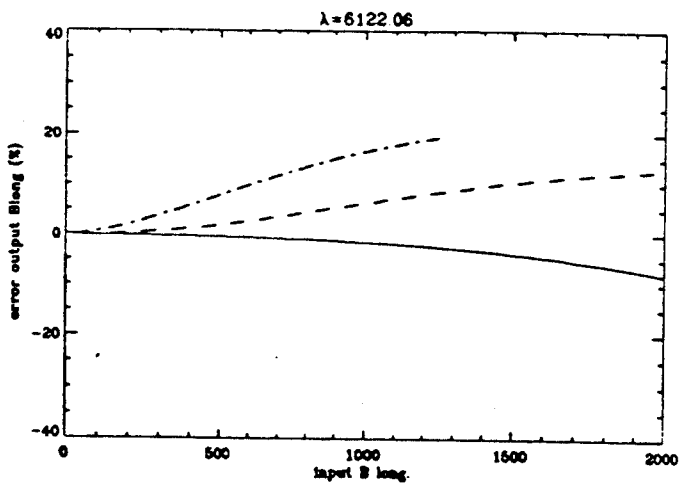
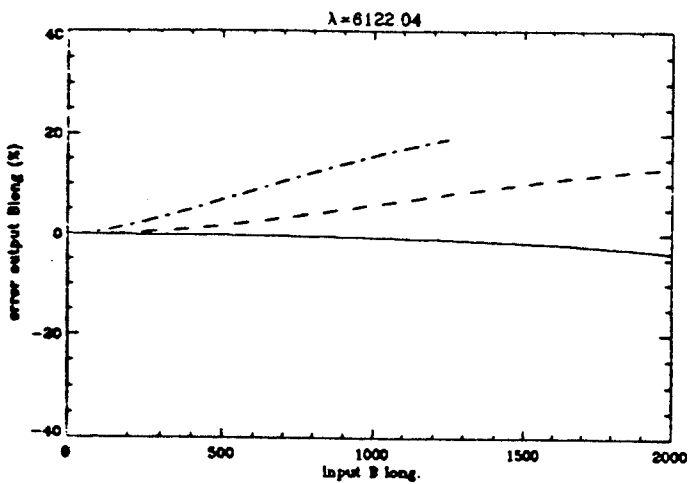
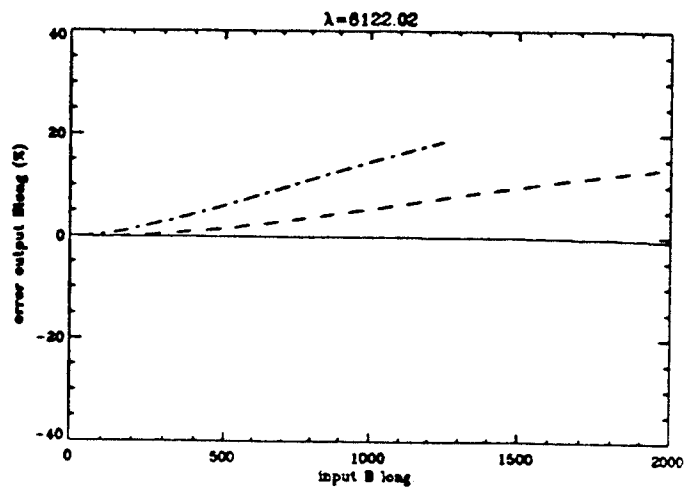
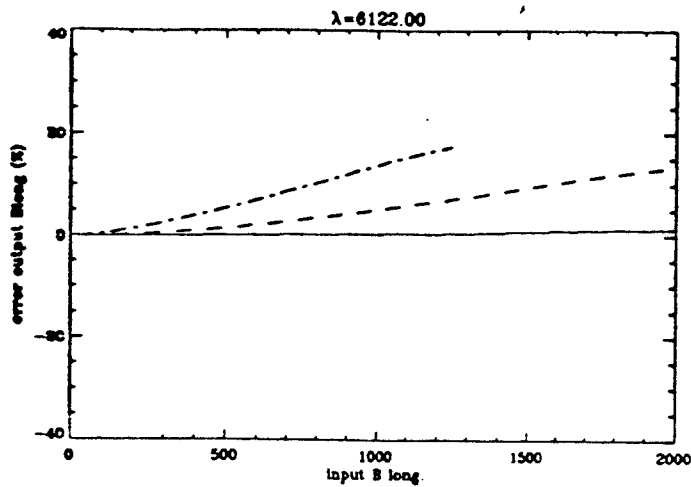
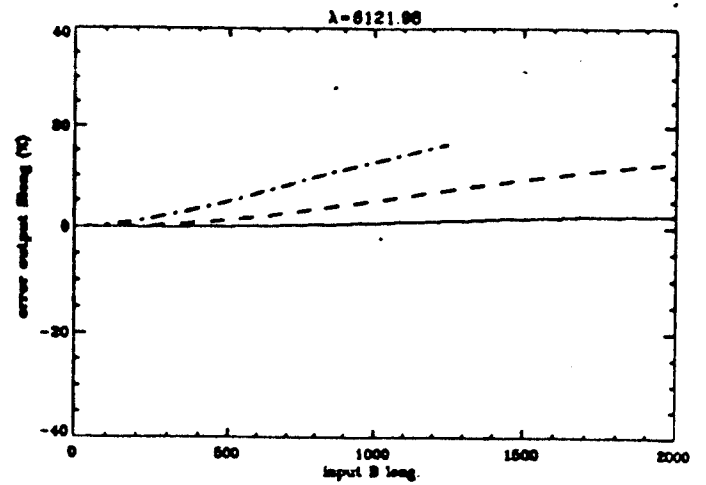
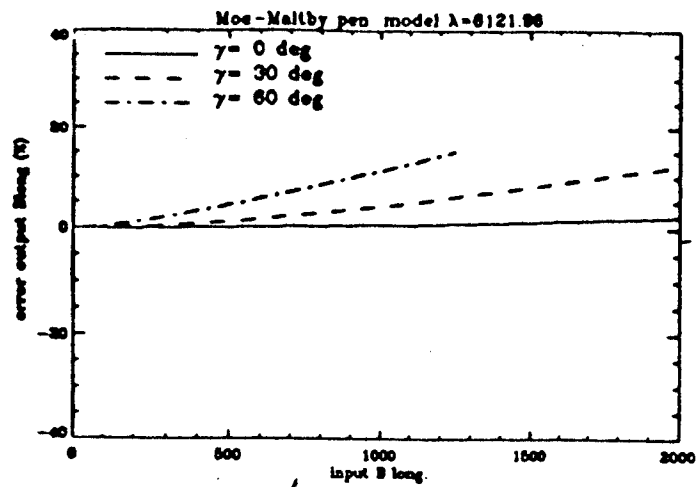


Fig 28

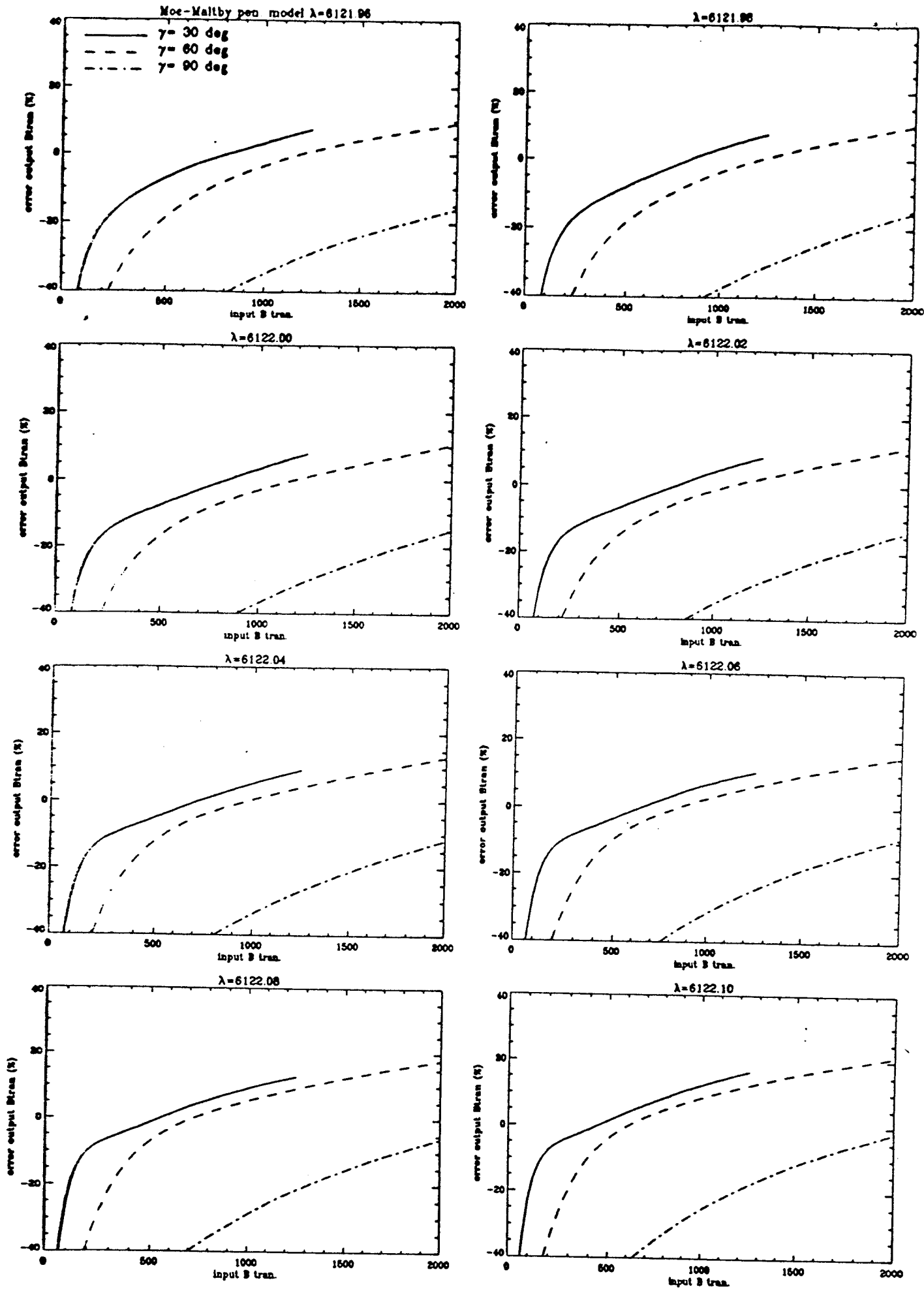


Fig 29

61221.8 61222.0 61222.2 61222.4 61222.6

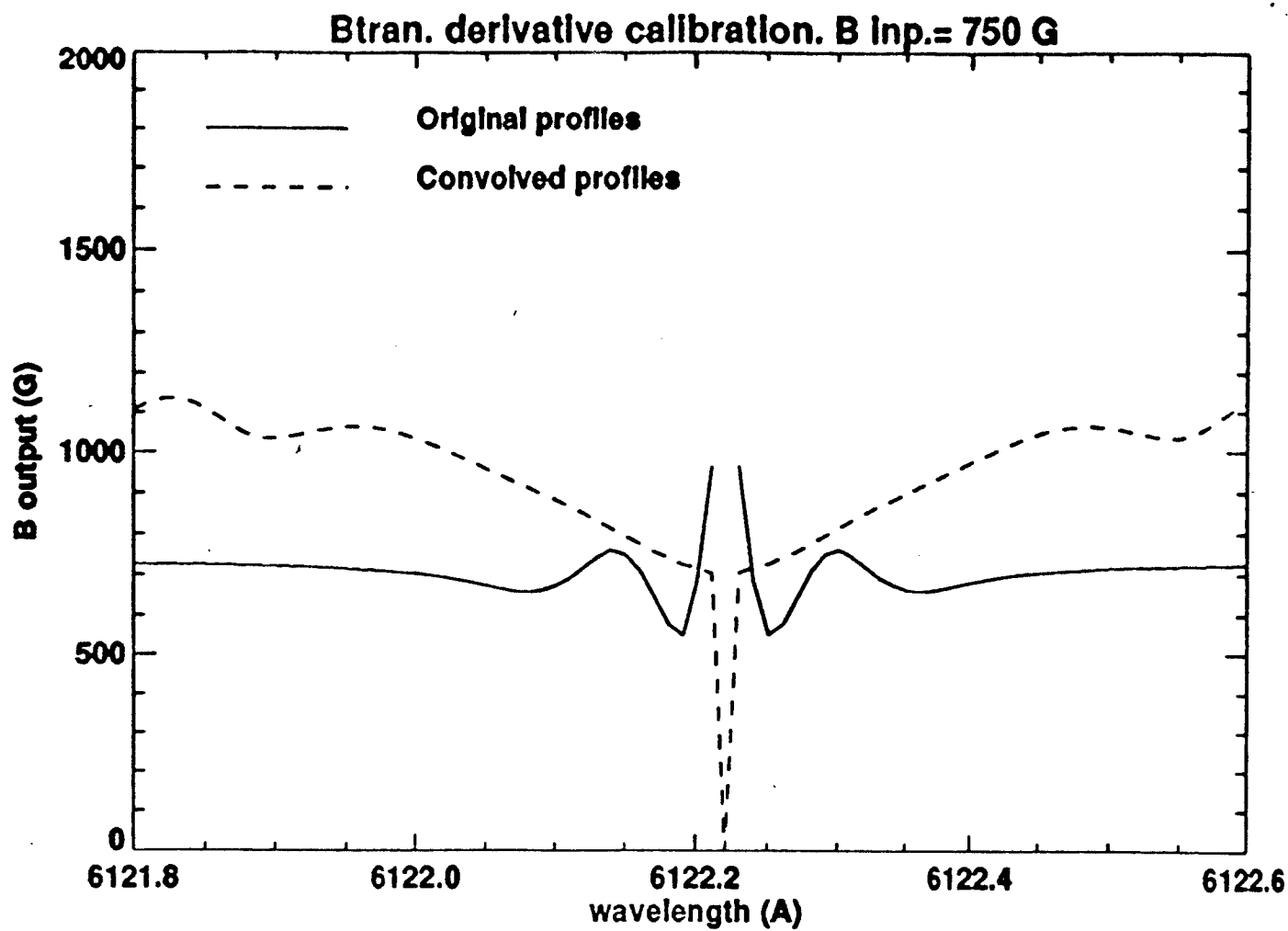


Fig 30

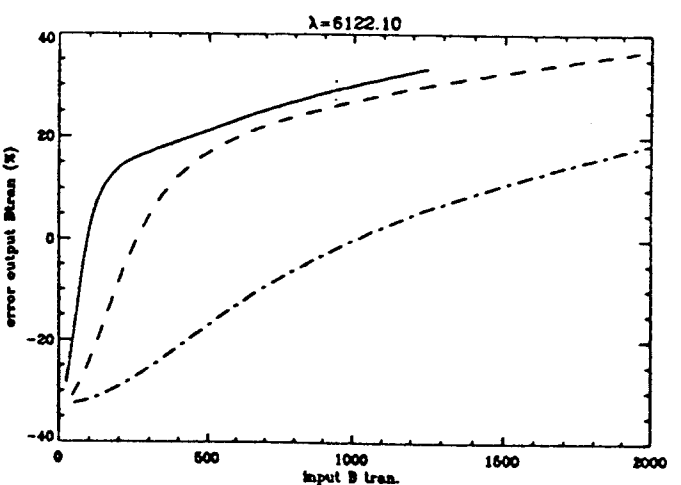
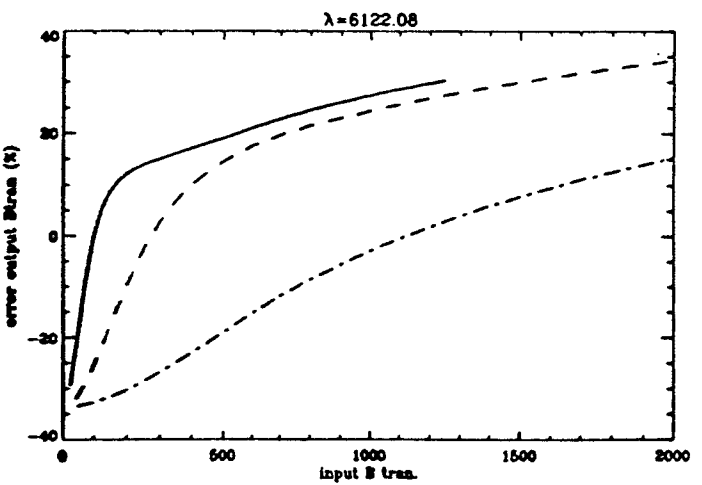
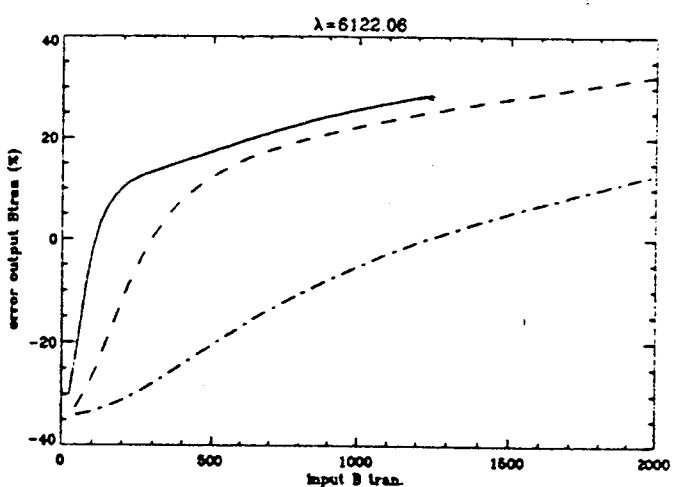
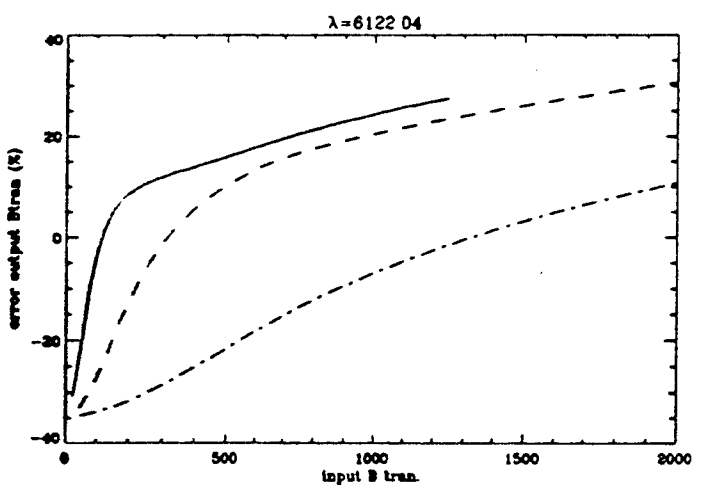
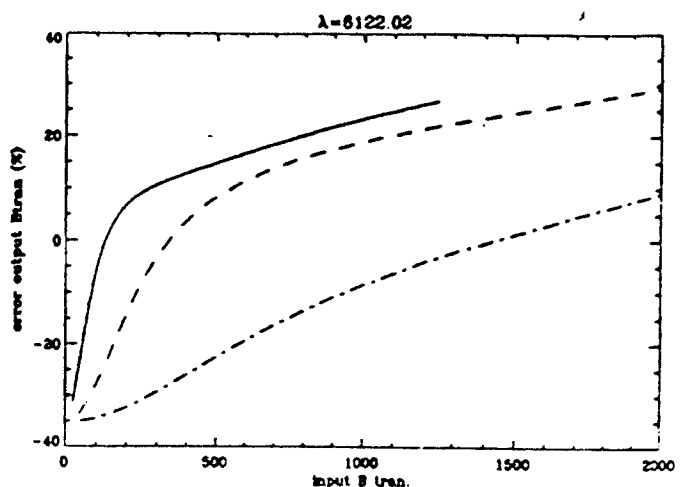
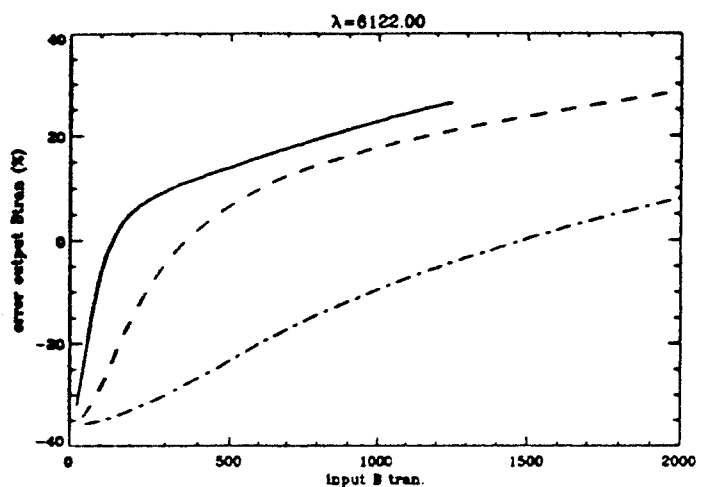
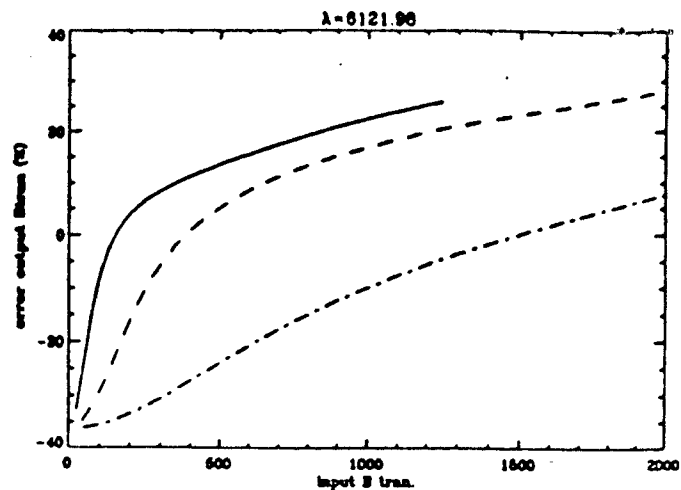
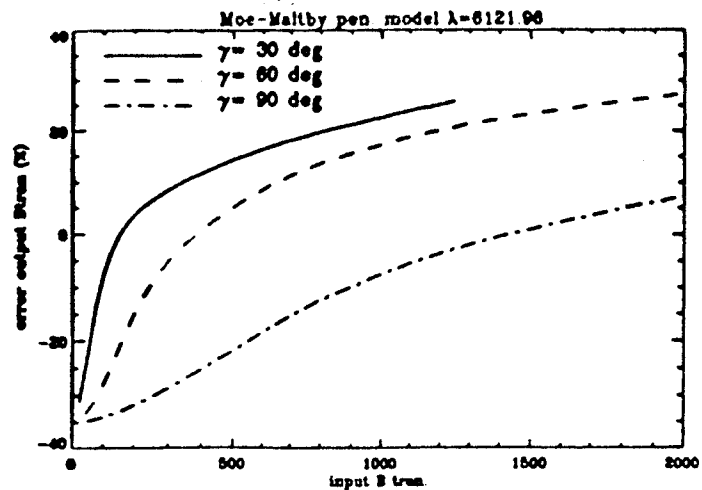
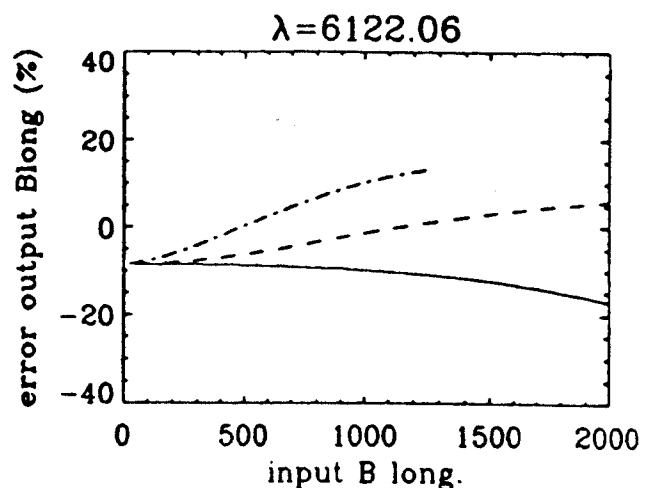
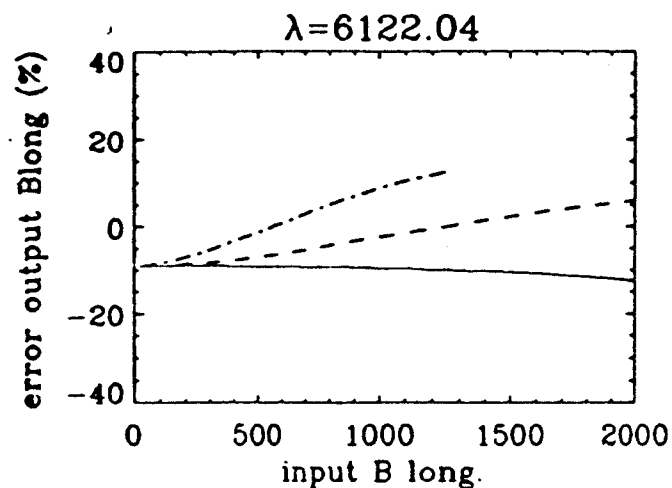
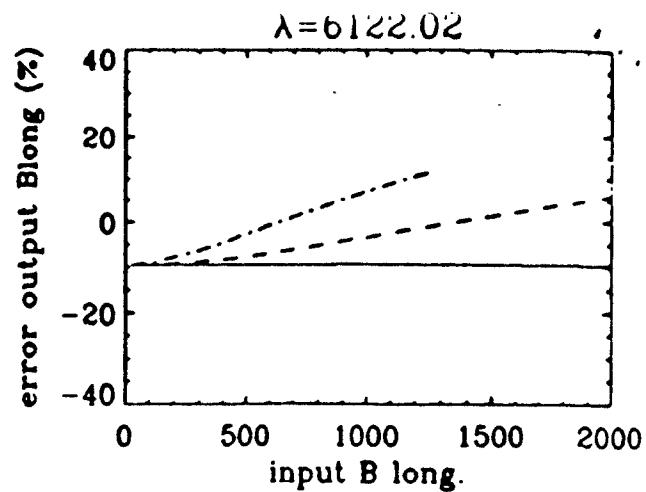
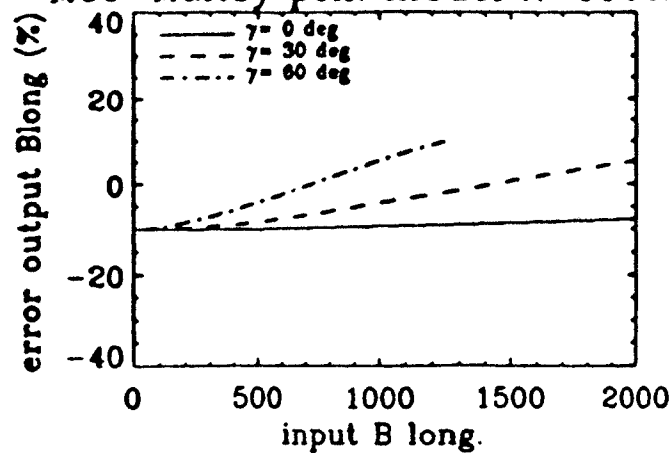
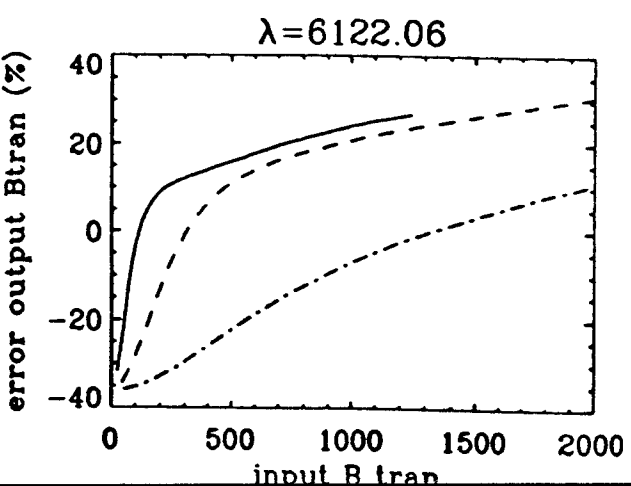
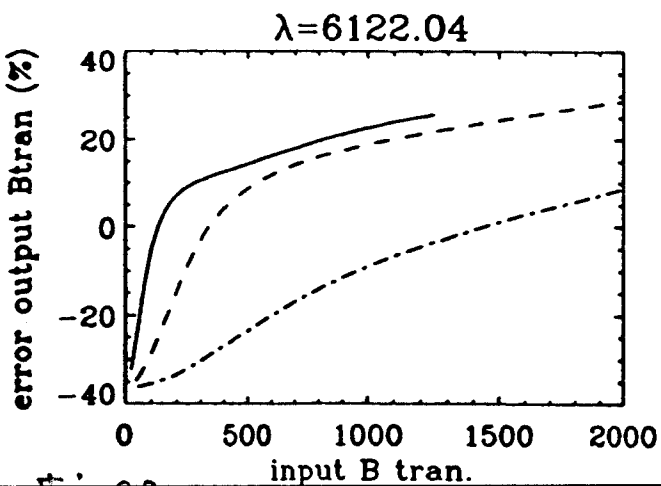
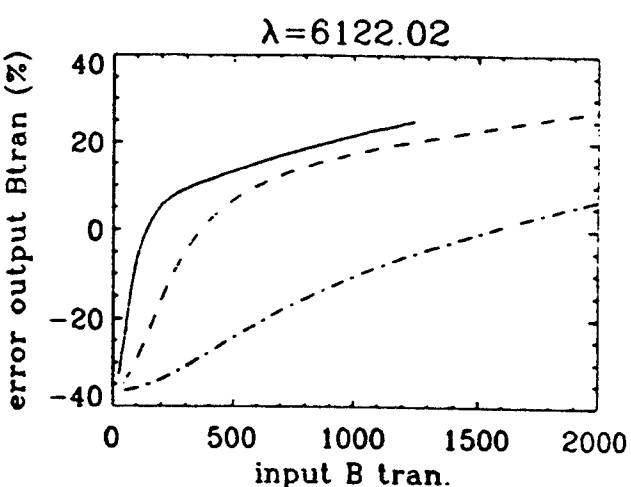
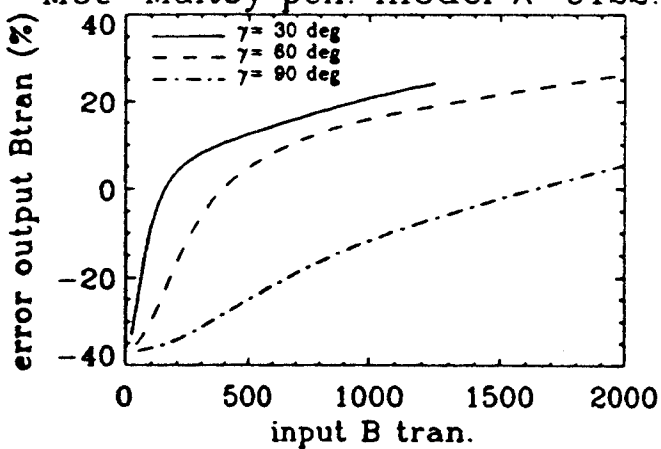


Fig 31

Moe-Maltby pen. model  $\lambda=6122.00$



Moe-Maltby pen. model  $\lambda=6122.00$



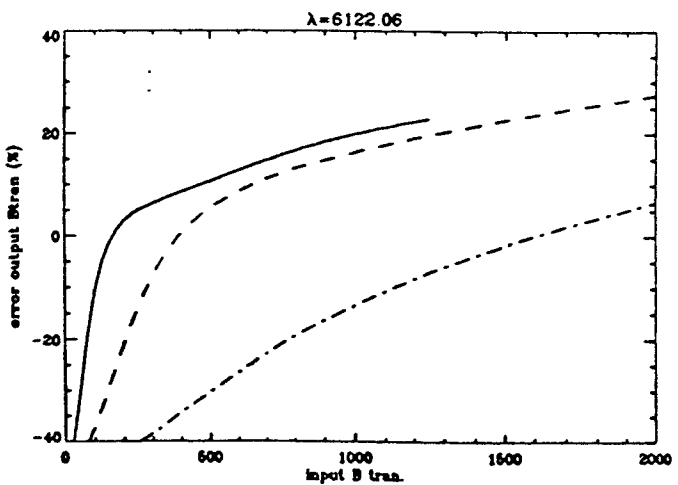
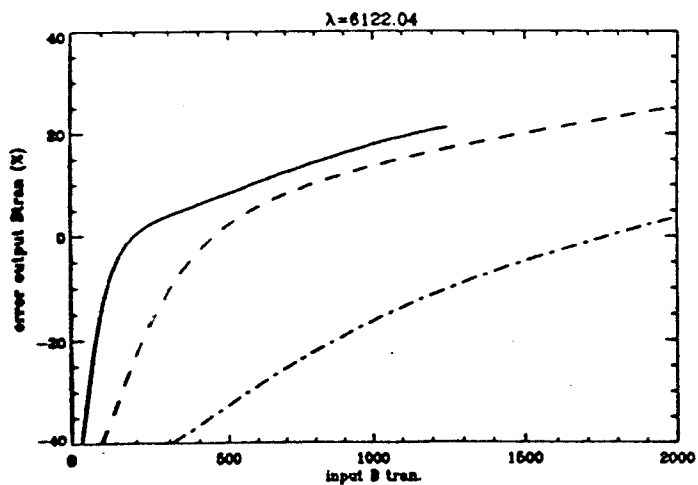
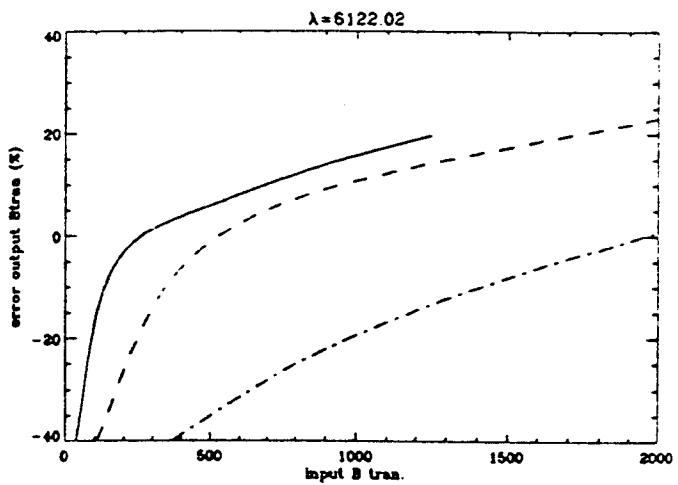
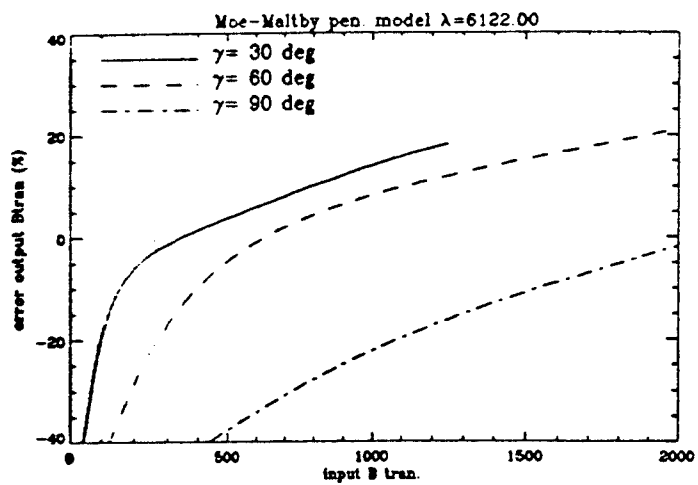
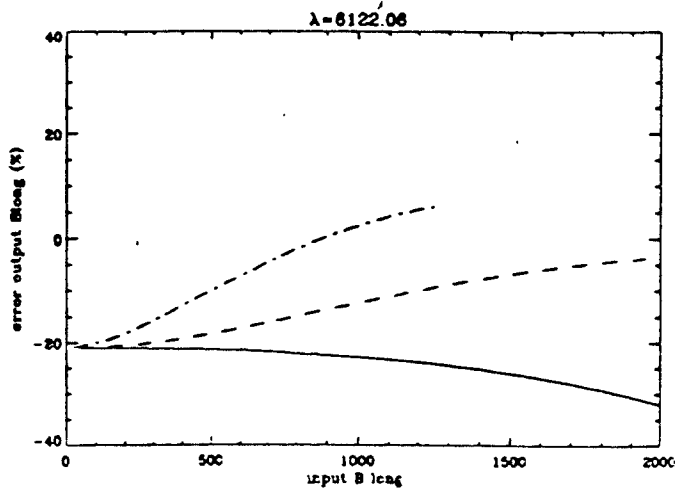
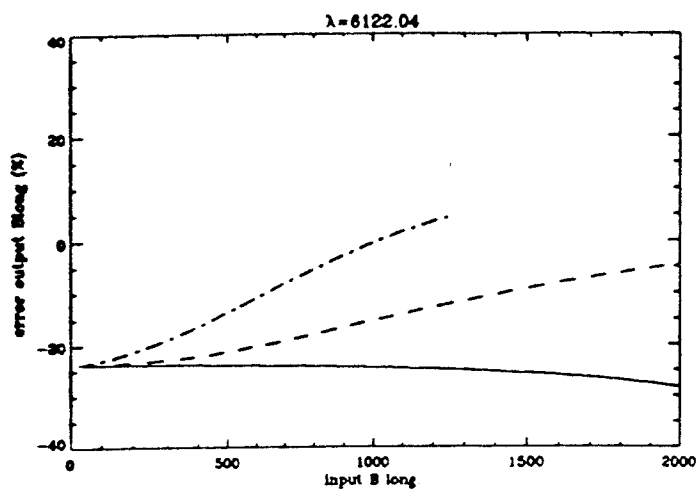
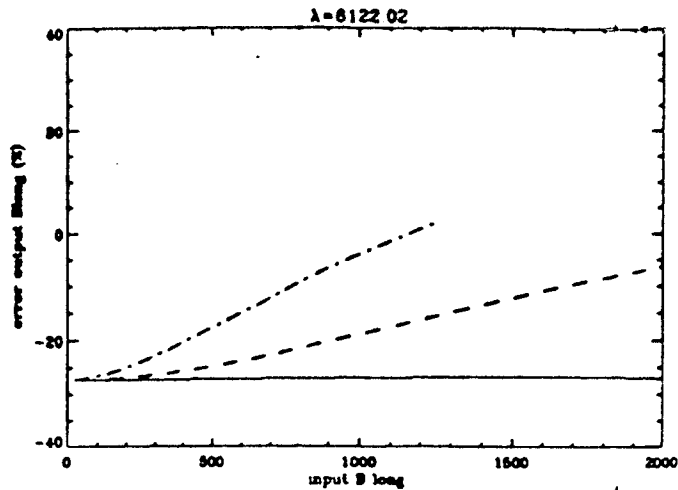
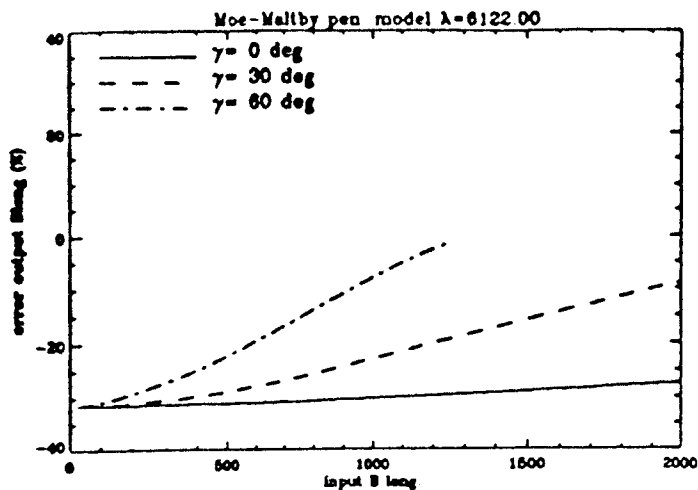


Fig 33

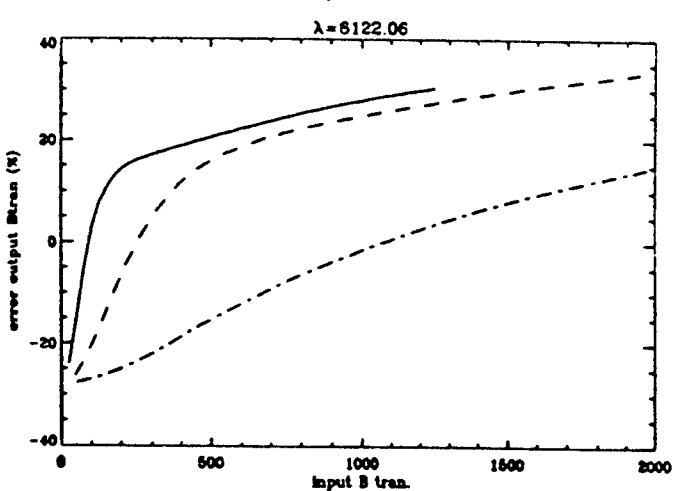
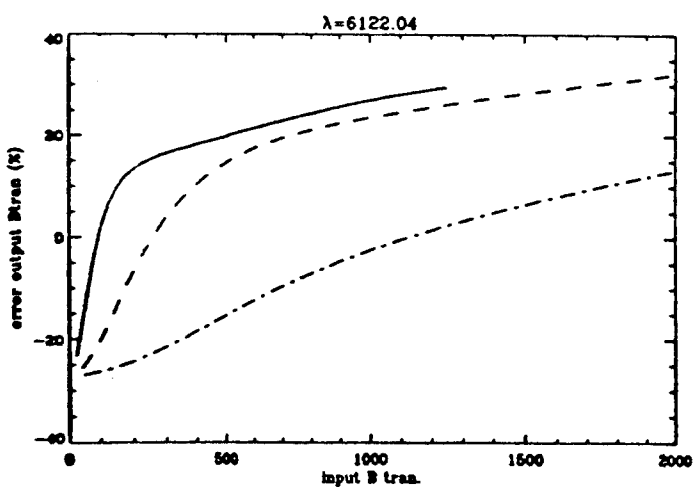
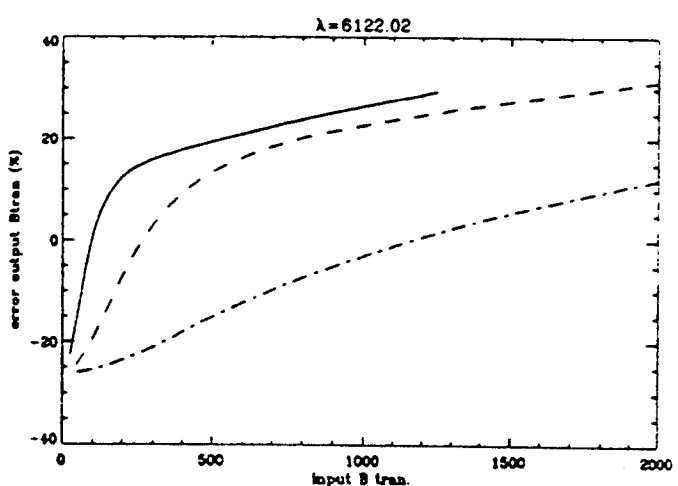
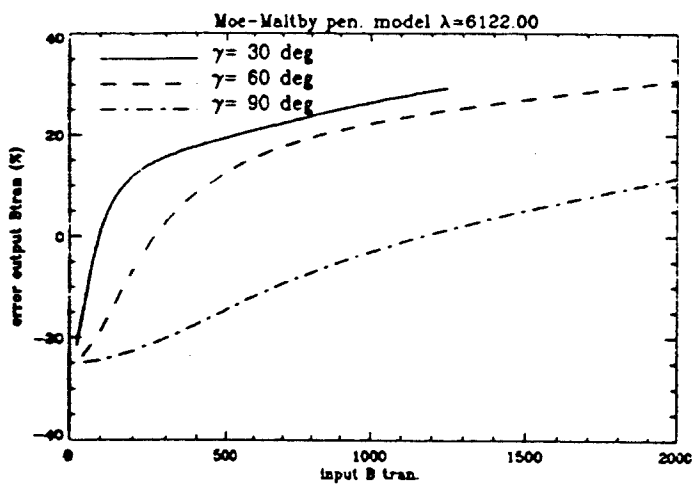
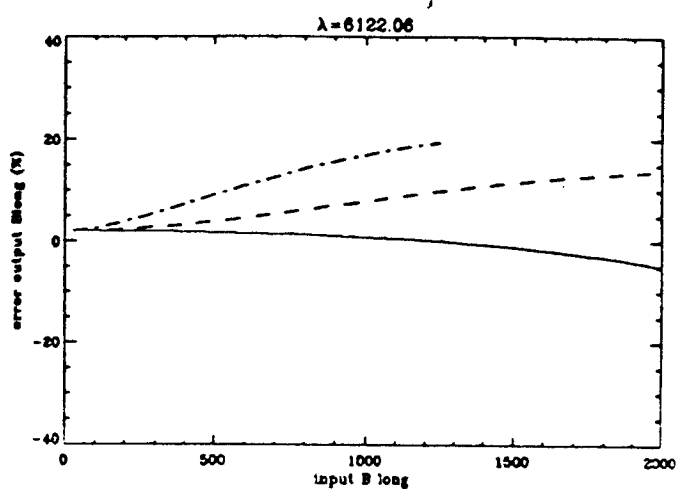
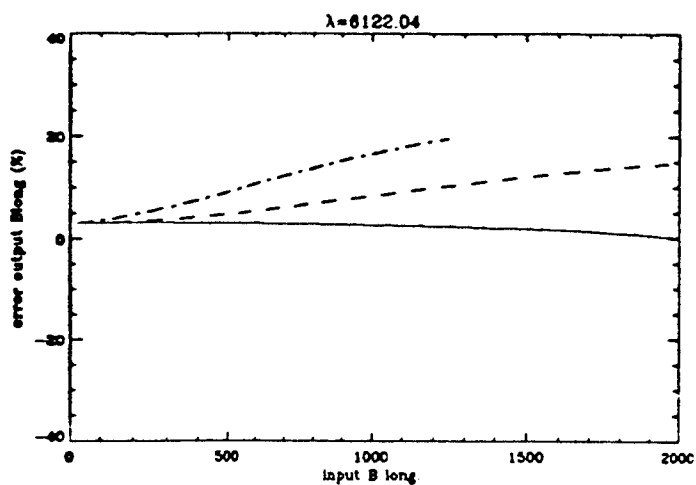
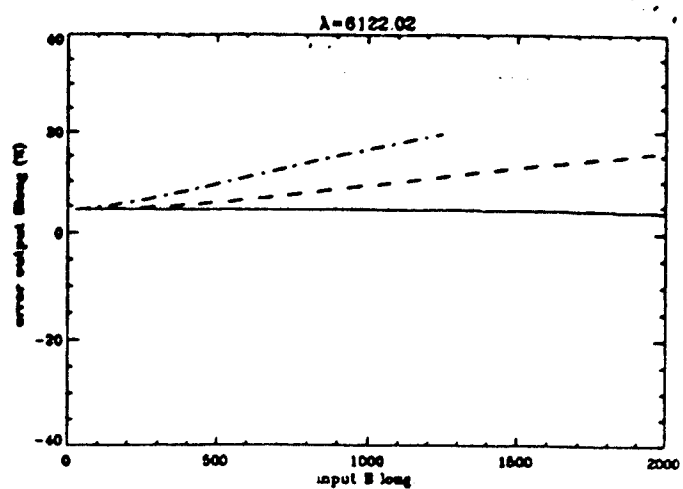
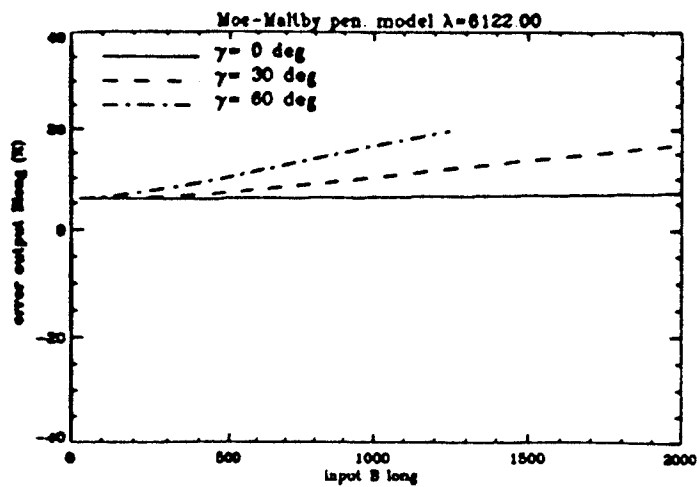


Fig 3/

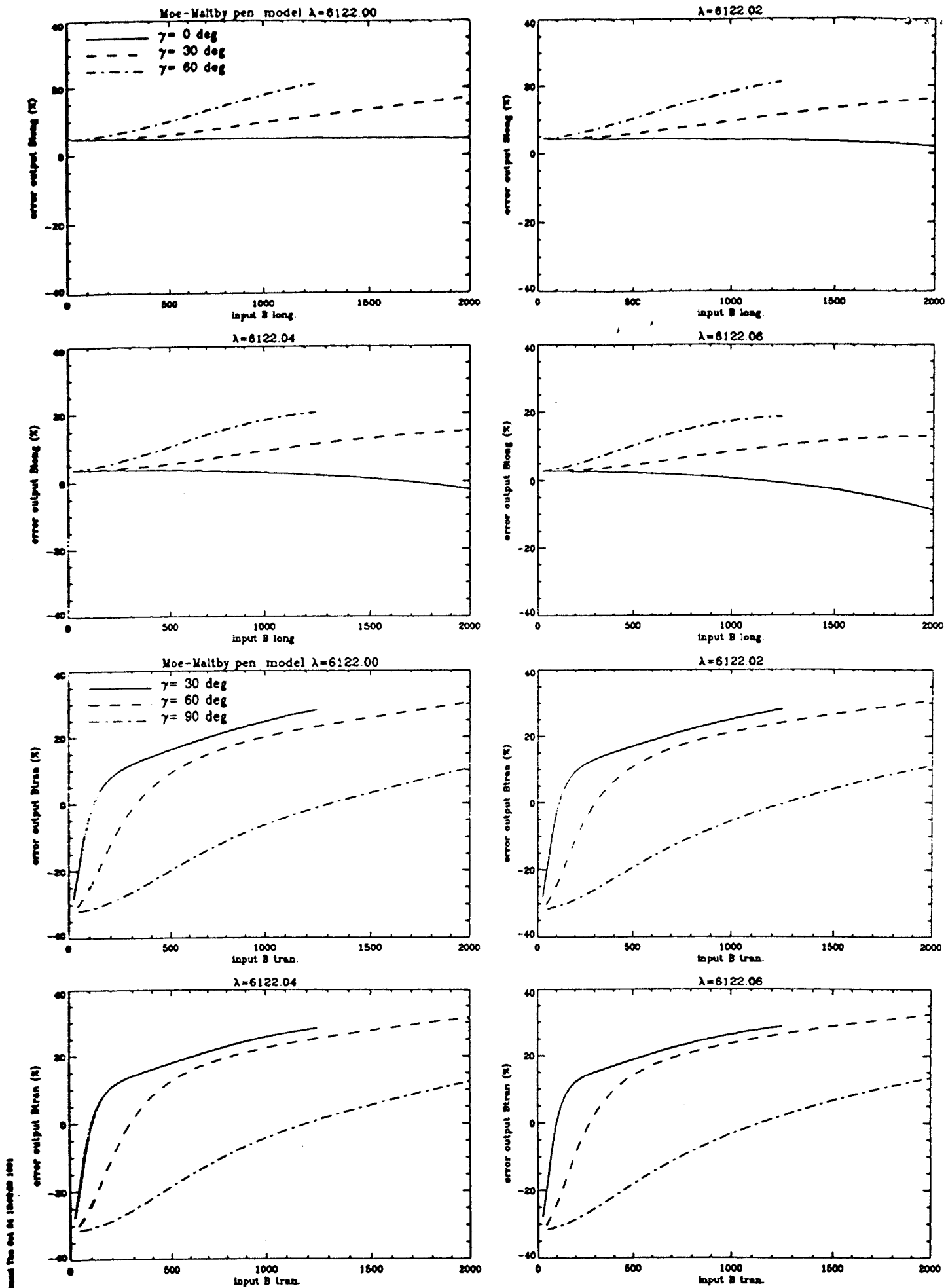
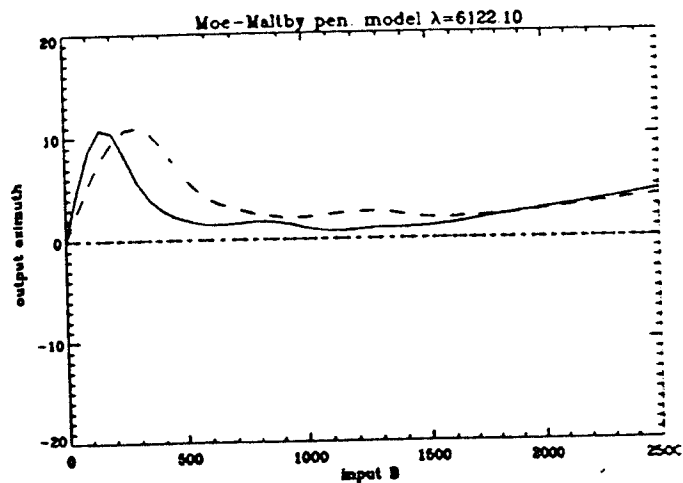
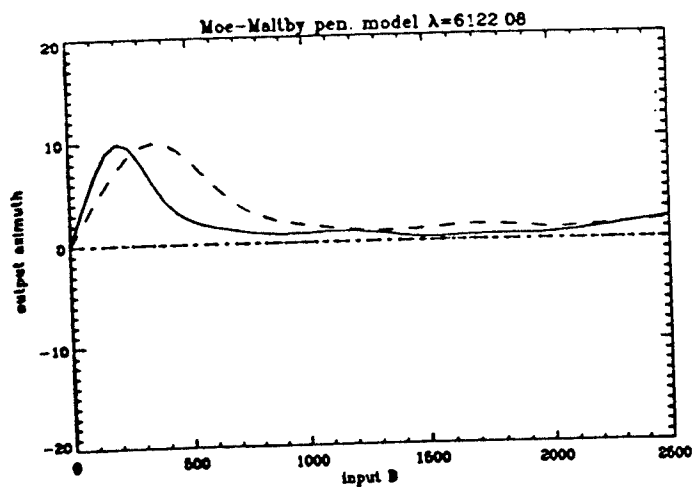
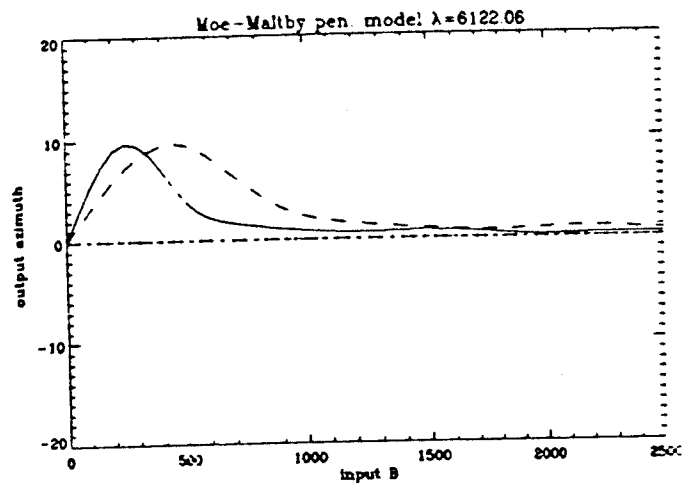
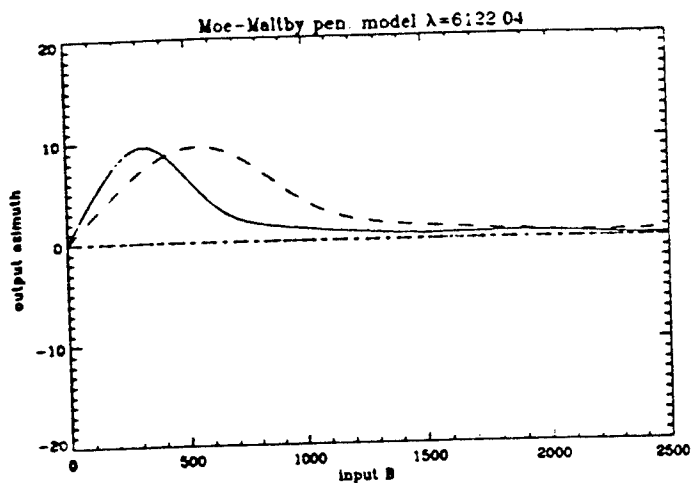
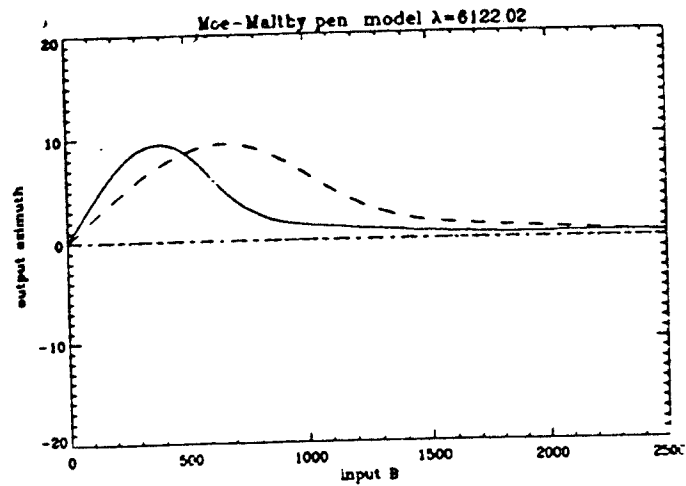
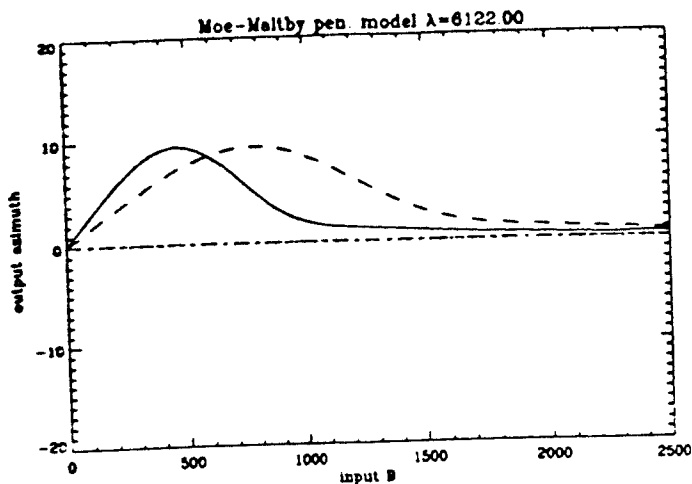
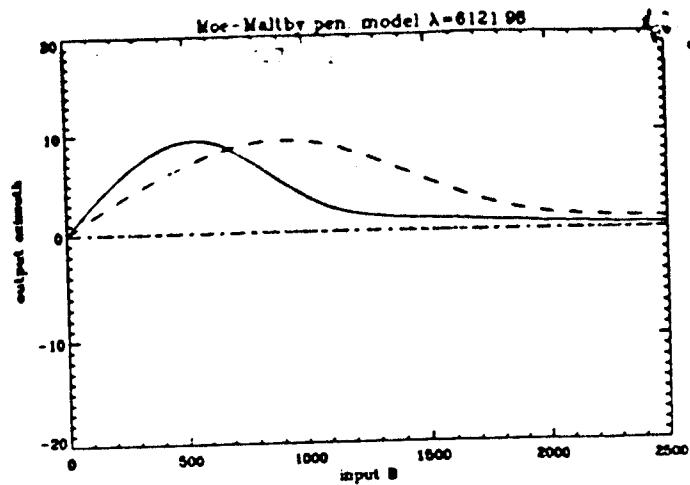
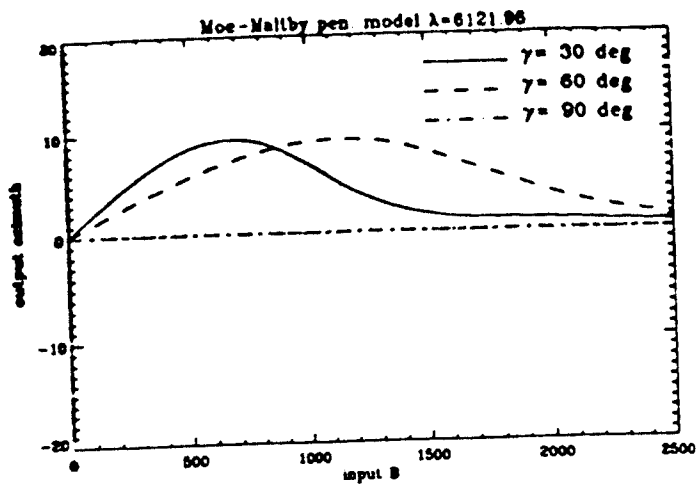


Fig 35



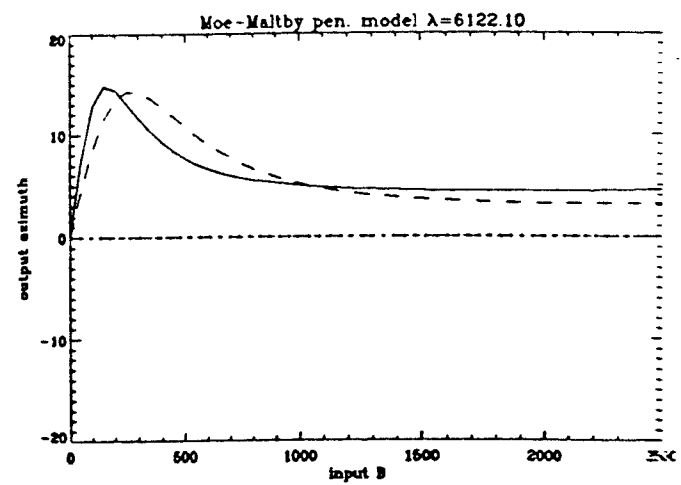
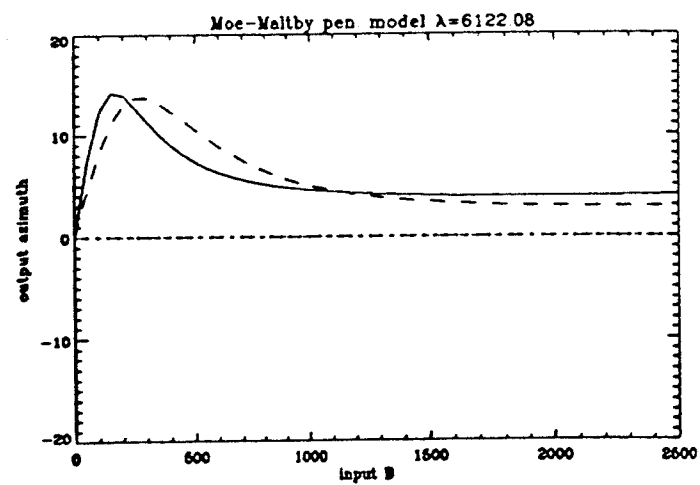
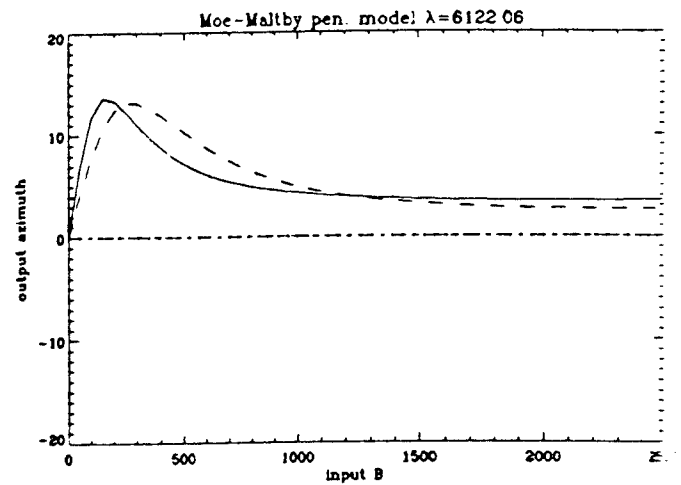
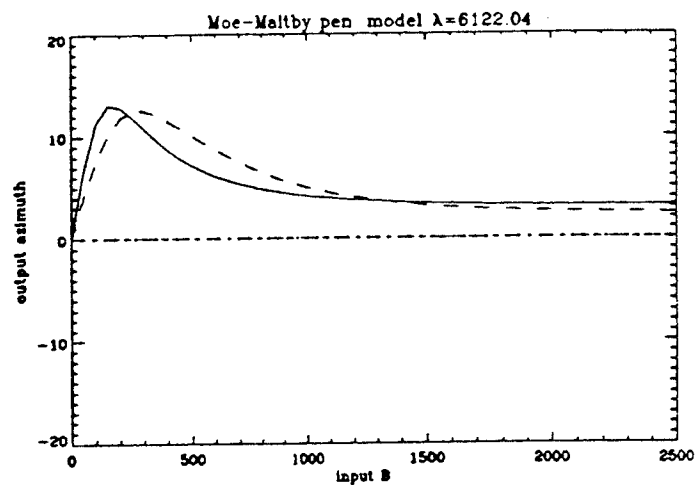
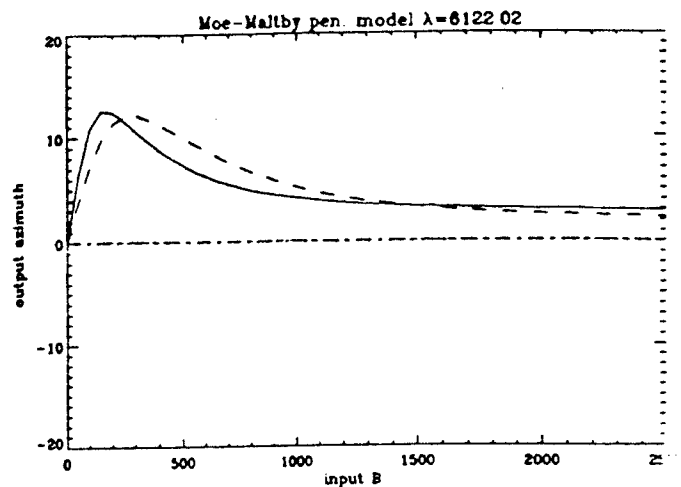
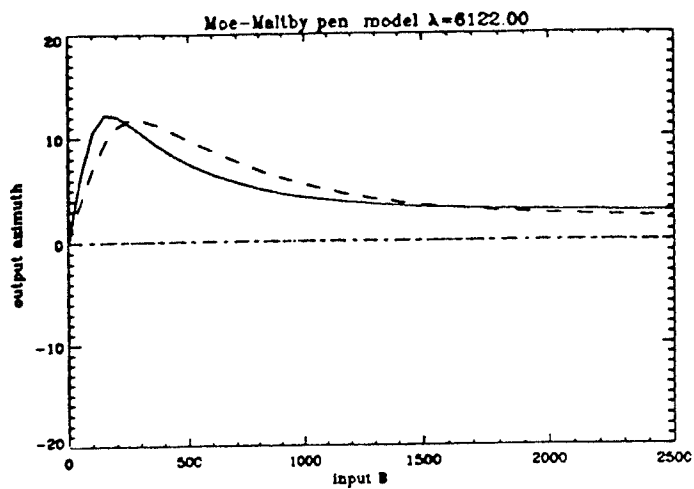
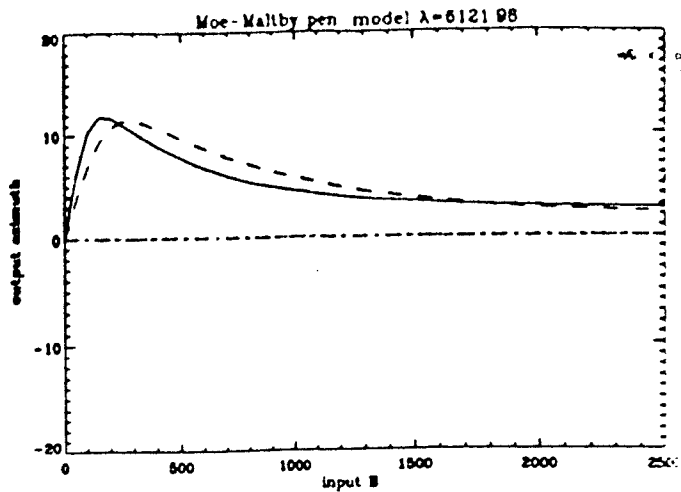
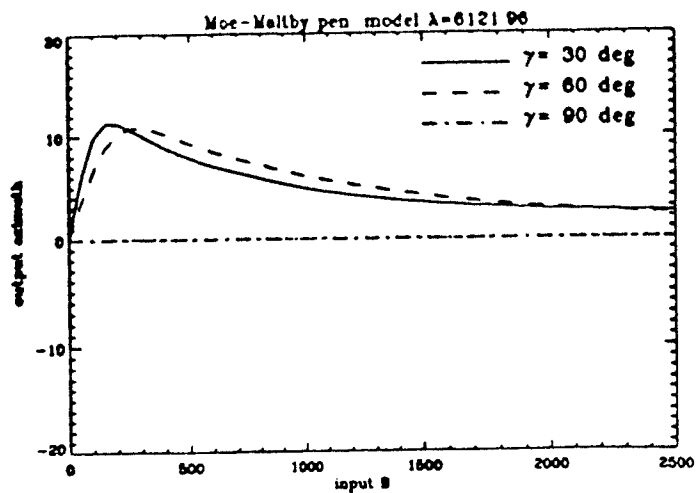
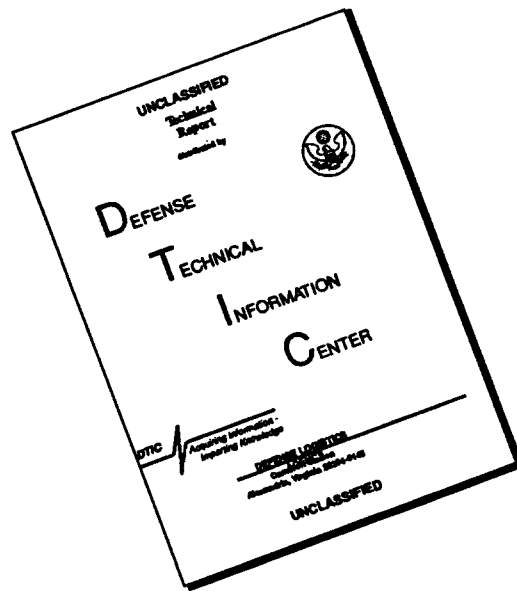


Fig 37

# DISCLAIMER NOTICE



THIS DOCUMENT IS BEST QUALITY AVAILABLE. THE COPY FURNISHED TO DTIC CONTAINED A SIGNIFICANT NUMBER OF PAGES WHICH DO NOT REPRODUCE LEGIBLY.